Louisiana State University
LSU Digital Commons

LSU Historical Dissertations and Theses | Graduate School

2001

De Haas-Van Alphen Effect Measurements on Cerium-Lanthanum-M-Indium (M = Cobalt, Rhodium, Iridium) Alloys.

Umit Alver
Louisiana State University and Agricultural & Mechanical College

Follow this and additional works at: https://digitalcommons.lsu.edu/gradschool_disstheses

Recommended Citation

Alver, Umit, "De Haas-Van Alphen Effect Measurements on Cerium-Lanthanum-M-Indium (M = Cobalt, Rhodium, Iridium) Alloys." (2001). *LSU Historical Dissertations and Theses*. 391.
https://digitalcommons.lsu.edu/gradschool_disstheses/391

This Dissertation is brought to you for free and open access by the Graduate School at LSU Digital Commons. It has been accepted for inclusion in LSU Historical Dissertations and Theses by an authorized administrator of LSU Digital Commons. For more information, please contact gradetd@lsu.edu.

INFORMATION TO USERS

This manuscript has been reproduced from the microfilm master. UMI films the text directly from the original or copy submitted. Thus, some thesis and dissertation copies are in typewriter face, while others may be from any type of computer printer.

The quality of this reproduction is dependent upon the quality of the copy submitted. Broken or indistinct print, colored or poor quality illustrations and photographs, print bleedthrough, substandard margins, and improper alignment can adversely affect reproduction.

In the unlikely event that the author did not send UMI a complete manuscript and there are missing pages, these will be noted. Also, if unauthorized copyright material had to be removed, a note will indicate the deletion.

Oversize materials (e.g., maps, drawings, charts) are reproduced by sectioning the original, beginning at the upper left-hand corner and continuing from left to right in equal sections with small overlaps.

Photographs included in the original manuscript have been reproduced xerographically in this copy. Higher quality 6" x 9" black and white photographic prints are available for any photographs or illustrations appearing in this copy for an additional charge. Contact UMI directly to order.

ProQuest Information and Learning
300 North Zeeb Road, Ann Arbor, MI 48106-1346 USA
800-521-0600

UMI®

Reproduced with permission of the copyright owner. Further reproduction prohibited without permission.

Reproduced with permission of the copyright owner. Further reproduction prohibited without permission.

DE HAAS VAN ALPHEN EFFECT MEASUREMENTS ON $Ce_xLa_{1-x}MIn_5$ (M = Co, Rh, Ir) ALLOYS

A Dissertation

Submitted to the Graduate Faculty of the
Louisiana State University and
Agricultural and Mechanical College
in partial fulfillment of the
requirements for the degree of
Doctor of Philosophy

in

The Department of Physics and Astronomy

by
Umit Alver
B.Sc., Karadeniz Technical University, 1989
M.Sc., Old Dominion University, 1997
December 2001

Reproduced with permission of the copyright owner. Further reproduction prohibited without permission.

UMI Number: 3042607

UMI®

UMI Microform 3042607
Copyright 2002 by ProQuest Information and Learning Company.
All rights reserved. This microform edition is protected against
unauthorized copying under Title 17, United States Code.

ProQuest Information and Learning Company
300 North Zeeb Road
P.O. Box 1346
Ann Arbor, MI 48106-1346

Reproduced with permission of the copyright owner. Further reproduction prohibited without permission.

ACKNOWLEDGMENTS

This dissertation is the result of work that came from many people in many different forms between 1997 and 2001. Although I can not thank everybody personally, there are several people whom I would like to thank here in particular.

First of all, I must thank my advisor Dr. Roy Gordon Goodrich for his excellent guidance, wisdom and especially his patience throughout this project. He has taught me how to be patient and persistent in experimental physics. In addition, during our trip with him to Tallahassee and Los Alamos, I have learned many things from him about the environment, culture and history of this country.

An experimental part of this work was performed at National High Magnetic Laboratory (NHMFL) in Tallahassee, Florida and in Los Alamos, New Mexico. I wish to thank Dr. Donavan Hall, one of the former students of Dr. Goodrich. I had several valuable discussions with Donavan during this work. Without his hospitality and continuing encouragement, in Tallahassee, this work would not have been possible. I also would like to thank Dr. Eric Palm, Dr. Tim Murphy, Dr. Stan Tozer for technical assistance during my experiments in Tallahassee.

A special thanks to Dr. Neil Harrison for helping me to take data at NHMFL in Los Alamos, New Mexico. Working in a laboratory like NHMFL at Los Alamos was a great chance and experience for me. I want to thank Dr. John Sarrao and his postdoc., Dr. P. G. Pagliuso, for providing us the samples used in this work.

Reproduced with permission of the copyright owner. Further reproduction prohibited without permission.

I am indebted to my colleagues and friends Dr. Cabir Terzioglu, Dr. Alem Teklu, Orhan Kizilkaya, Gurcan Aral and Jabari Lee for helping me in many different ways.

I would like to express my deepest love and appreciation to my wife, Nebahat, for her, patience, sacrifice and continuous support during my work in this country. Her encouragement during my difficult times helped me to continue my long trip.

Finally, I am thankful for my parents, brother and sister for their support. I especially want to thank my father for his continuos support and encouragement when I needed it most.

Reproduced with permission of the copyright owner. Further reproduction prohibited without permission.

TABLE OF CONTENTS

ACKNOWLEDGEMENTS ii

LIST OF TABLES vi

LIST OF FIGURES viii

ABSTRACT xi

CHAPTER

1 **GENERAL INTRODUCTION** 1
- 1.1 Free Electron Model 1
- 1.2 Band Theory of Metals 4
- 1.3 Fermi Surface of Metals 8
- 1.4 Effective Mass 9
- 1.5 The Fermi Liquid 11
- 1.6 Magnetic Properties of Solids 11
- 1.7 Organization of the Dissertation 16

2 **HEAVY FERMION MATERIALS** 19
- 2.1 Overview 19
- 2.2 Physical Properties of Heavy Fermions 23
- 2.3 Heavy Fermion Superconductivity 29
- 2.4 $CeMIn_5$ Family 31
  - 2.4.1 CeIrIn5 33
  - 2.4.2 $CeCoIn_5$ 35
  - 2.4.3 $CeRhIn_5$ 37
  - 2.4.4 $LaMIn_5$ 37

3 **THE DE HAAS VAN ALPHEN EFFECT** 40
- 3.1 Historical Background 40
- 3.2 Quantization of Electron Orbits in a Magnetic Field 42
- 3.3 Lifshitz-Kosevich (LK) Equation 48
- 3.4 Reduction Factors in LK Equation 50
- 3.5 dHvA Effect in Heavy Fermion Systems 51
- 3.6 Experimental Techniques 53
  - 3.6.1 Introduction 53
  - 3.6.2 The Torque Method 54
  - 3.6.3 The Pulsed Field Method 57
  - 3.6.4 The Field Modulation Method 61

4 **DHVA MEASUREMENTS ON $Ce_xLa_{1-x}RhIn_5$** 62
- 4.1 dHvA Measurements on $LaRhIn_5$ 62
- 4.2 dHvA Measurements on $CeRhIn_5$ 65
- 4.3 dHvA Measurements on $Ce_xLa_{1-x}RhIn_5$ 71

Reproduced with permission of the copyright owner. Further reproduction prohibited without permission.

4.3.1 Measurements of dHvA Frequencies of the $Ce_xLa_{1-x}RhIn_5$ Compounds....71
4.3.2 Concentration Dependence of Frequencies 76
4.3.3 Measurement of Cyclotron Masses of the $Ce_xLa_{1-x}RhIn_5$ Compounds....78
4.3.4 Concentration Dependence of Effective Masses.... 81
4.3.5 Field Dependence of Effective Masses....87
4.3.6 Measurement of the Dingle Temperatures 87
4.3.7 Spin Dependence of Carriers 91

5 DHVA MEASUREMENTS ON $Ce_xLa_{1-x}CoIn_5$ 94
5.1 dHvA Measurements on $LaCoIn_5$ 94
5.2 dHvA Measurements on $CeCoIn_5$ 96
5.3 dHvA Measurements on $Ce_xLa_{1-x}CoIn_5$ 100
5.3.1 Concentration Dependence of Frequencies 101
5.3.2 Concentration Dependence of Effective Masses 101
5.3.3 The Dingle Temperature 105
5.3.4 Spin Dependence of Carriers 108

6 DHVA MEASUREMENTS ON $Ce_xLa_{1-x}IrIn_5$ 110
6.1 dHvA Measurements on $Ce_xLa_{1-x}IrIn_5$ 110
6.2 Concentration Dependence of the Frequencies 113
6.3 Concentration Dependence of Effective Masses 113
6.4 The Dingle Temperature 115
6.5 Spin Dependence of Carriers 121

7 SUMMARY AND CONCLUSIONS 122

REFERENCES 126

APPENDIX LETTER OF PERMISSION.... 133

VITA 135

Reproduced with permission of the copyright owner. Further reproduction prohibited without permission.

LIST OF TABLES

2.1 Observed transition of some of the most interesting heavy fermion system. γ is the specific heat coefficient.....21

2.2 Atomic positions and lattice parameters of $CeMIn_5$ family. Data was taken from Ref. [82, 55, 78].....34

2.3 dHvA frequencies and corresponding cyclotron effective masses of $CeIrIn_5$ [79].....35

2.4 Measured dHvA effect frequencies and effective masses for B || [100] and B || [001] in $CeRhIn_5$. Frequencies in parenthesis are corrected by 4.5% [68] 38

2.5 Atomic positions and lattice parameters of $LaMIn_5$ family. Data was taken from Robin Macaluso, a graduate student in Department of Chemistry, Louisiana State University.....38

4.1 Techniques used for dHvA measurement on $Ce_xLa_{1-x}RhIn_5$ compounds.....63

4.2 Measured frequencies and cyclotron masses of $LaRhIn_5$.....63

4.3 Measured and calculated dHvA frequencies and measured effective masses for $CeRhIn_5$ with B along the [100]. Frequencies listed by Cornelius have been corrected by 4.5% (Ref. [68]).....68

4.4 Measured and calculated dHvA frequencies and measured effective masses for $CeRhIn_5$ with B along the [001]. Frequencies listed by Cornelius have been corrected by 4.5% (Ref. [68]).....68

4.5 Measured dHvA frequencies and effective masses for $Ce_xLa_{1-x}RhIn_5$ with the field along [100] direction 82

4.6 Measured dHvA frequencies and effective masses for $Ce_xLa_{1-x}RhIn_5$ with the field along [001] direction 83

4.7 Dingle temperatures and free path for f7 orbits in $Ce_xLa_{1-x}RhIn_5$ 91

5.1 Measured dHvA frequencies and effective masses for $LaCoIn_5$ with the field along [001].....96

Reproduced with permission of the copyright owner. Further reproduction prohibited without permission.

5.2 Measured dHvA frequencies for $CeCoIn_5$ with the field along [001].....99

5.3 dHvA frequencies and measured effective masses for $CeCoIn_5$ with the field along [111] 99

5.4 Measured dHvA frequencies and effective masses for $Ce_xLa_{1-x}CoIn_5$ for B || [001].....103

5.5 Dingle temperatures and free path for f8 orbits in $Ce_xLa_{1-x}CoIn_5$ 108

6.1 Measured dHvA frequencies and effective masses for $Ce_xLa_{1-x}IrIn_5$ with the field along the [001] direction 117

6.2 Measured dHvA frequencies and effective masses for $Ce_xLa_{1-x}IrIn_5$ with the field along the [100] direction 118

6.3 Dingle temperatures and free path *l* for f4 orbits in $Ce_xLa_{1-x}IrIn_5$ 120

Reproduced with permission of the copyright owner. Further reproduction prohibited without permission.

LIST OF FIGURES

2.1 A schematic view of the Kondo effect observed in dilute systems at low temperatures [57]. The logarithmic contribution to the resistivity arises from spin-flip scattering 22

2.2 C/T as a function of T^2 for a) UPt_3 b) UCd_{11} (The inset shows the field dependence of γ) c) $CeRhIn_5$. These figures were reproduced from Ref. [30, 66, 67].....25

2.3 Inverse magnetic susceptibility vs temperature for $CeRhIn_5$ and $CeAl_3$. The inset shows saturation indicating itinerant *f* electron behavior below 1.5 K for $CeAl_3$. These plots were reproduced from Ref. [30] and [69].....26

2.4 Temperature dependence of resistivity a) for several heavy fermion compounds (from Fisk et al, [30]) and b) for $CeRhIn_5$. (from Hegger et al, [40]) 28

2.5 Crystal structure of $CeMIn_5$ (M=Rh, Ir, Co) family.....32

2.6 FFT of dHvA frequencies with the applied field along the [001] direction. This plot was reproduced from Ref.[79] 36

2.7 Angular dependence of dHvA frequencies for $CeIrIn_5$ (This figure was reproduced from Ref [79]) 36

3.1 (a) Allowed electron orbits in two dimensional k-space in the absence of a magnetic field in (b) quantization of electron orbits in two dimensional k-space in the presence of a strong magnetic field. (c) quantization of electron orbits in three dimensional k-space in a strong magnetic field. Allowed energy states lie on the concentric cylinder called Landau levels and the occupied portion of these levels is cut by Fermi surface. With increasing magnetic field Landau cylinders expands and they become empty when they pass out of the Fermi surface. (d) A schematic diagram of energy states, filled up to the Fermi energy E_F, split into Landau levels in the presence of magnetic field **B**. Here, the spin of electron is neglected for clarity. These figures are reproduced from Ref. [10] and [27] 44

3.2 The schematic of a capacitive cantilever magnetometer. The sample is attached to the flexible plate. By applying a magnetic field **B**, the torque $\boldsymbol{\tau} = \mathbf{m} \times \mathbf{B}$ deflects the lever. Measurement of deflection gives information about sample magnetization.....56

3.3 The schematic of the experimental set up for pulsed field measurement 58

3.4 Field profile of 50 Tesla pulse field magnet at LANL.....59

Reproduced with permission of the copyright owner. Further reproduction prohibited without permission.

4.1 dHvA oscillation (inset) and its Fourier transform for $LaRhIn_5$ a) for the field along the [100] direction at T=2.44K b) for the field along the [001] direction at T=1.75K 64

4.2 a) dHvA frequencies of $CeRhIn_5$ with the field along the[100] direction. The inset shows some of the high frequencies that are the combinations of the fundamentals. b) dHvA frequencies of $CeRhIn_5$ with the field along the [001] direction 66

4.3 Angular dependence of dHvA frequencies for $CeRhIn_5$. Calculated frequencies for [001] and [100] directions are indicated with bowties 67

4.4 a) The first, b) the second and c) the third sheet of parametric $CeRhIn_5$ Fermi surface. The electron surfaces are illuminated.....70

4.5 a) The torque oscillation of the $Ce_{0.05}La_{0.95}RhIn_5$ sample at 1.3K for B || [100] and b) its corresponding Fourier transform.....73

4.6 Pulse field data for $Ce_{0.5}La_{0.5}RhIn_5$ for the field along the [001] direction at 1.43K. The dark lines represent the rising field and the light lines represent the falling field.....74

4.7 a) dHvA oscillation of a pulsed field measurement for $Ce_{0.5}La_{0.5}RhIn_5$ at 1.43K for B || [001] and b) its corresponding Fourier transform.....75

4.8 a) Concentration dependence of dHvA frequencies for B || [100] and b) for B || [001]. The dotted lines are a guide for the eye.....77

4.9 Mass plot of $Ce_{0.97}La_{0.03}RhIn_5$ for the F3 orbit with the filed along the [100] direction. The solid line represents the fit corresponding the reduction factor R_T in LK equation.....80

4.10 Concentration dependence of effective masses for B || [100] for two frequencies a) F2 and b) F3. The dotted lines are a guide for eye.....85

4.11 Concentration dependence of the effective masses for B || [001] a) for f2 b) for f4 c) for f7 orbits. The dotted lines are a guide for eye. The value of effective masses for x=1 for f4 orbit was taken Ref. [68].....86

4.12 The field dependence of effective masses for f2 and f7 orbits at the selected concentration for B || [001] 88

4.13 Dingle plot of some of $Ce_xLa_{1-x}RhIn_5$ compounds for f7 frequency. The Dingle temperatures T_D are determined from the slope of the straight lines ...90

Reproduced with permission of the copyright owner. Further reproduction prohibited without permission.

4.14 A plot of $\ln[A_p/p^{1/2})]$ versus harmonic index p for the F3 frequency, for which several harmonics could be observed. The dHvA signal is dominated by a single spin for $x \geq 0.5$, evidenced by the straight line.....93

5.1 a) dHvA oscillation measured in pulsed field of $LaCoIn_5$ at 0.43 K b) Frourier transform of the signal shown in a).....95

5.2 The Fourier transform of dHvA oscillations shown in the inset for the field along the c-axis. Both F_1 and F_6 are difficult to see in this Fourier transform. The amplitude of F_1 and F_6 grow with the increasing angle. (F_6 is observable at high fields.) 98

5.3 Angular dependence of the dHvA frequencies for $CeCoIn_5$.....98

5.4 a) dHvA oscillation of pulsed field measurement for $Ce_{0.1}La_{0.9}CoIn_5$ at 1.47 K for B || [001] and its corresponding Fourier transform.....102

5.5 Concentration dependence of dHvA frequencies for $Ce_xLa_{1-x}CoIn_5$ with the field along [001] direction. The dotted lines are a guide for the eye.....104

5.6 Concentration dependence of effective masses for $Ce_xLa_{1-x}CoIn_5$ with the field along the [001] direction. The solid lines represent the quadratic fit....106

5.7 Dingle plot of some $Ce_xLa_{1-x}CoIn_5$ compounds for f8 frequency. The Dingle temperatures are determined from the slope of straight lines.....107

5.8 A plot of $\ln(A_p/p^{1/2})$ versus the harmonic number p for the f8 frequency.....109

6.1 a) The pulsed field dHvA oscillation of the $Ce_{0.03}La_{0.97}IrIn_5$ sample at 1.43 K for B || [100] and b) its corresponding Fourier transform 111

6.2 a) dHvA oscillations of pulsed field measurements for $Ce_{0.1}La_{0.9}IrIn_5$ at 0.49 K for B || [001] and b) its corresponding Fourier transform.....112

6.3 a) Concentration dependence of dHvA frequencies for B || [100] and b) for B || [001]. The dotted lines are a guide for the eye.....114

6.4 Concentration dependence of effective masses for $Ce_xLa_{1-x}IrIn_5$ for B || [001]. The solid lines are a quadratic fit to the data.....116

6.5 Dingle plot of $Ce_xLa_{1-x}IrIn_5$ compounds for f4 orbits for different concentrations.....119

6.6 Plot of concentration dependence of Dingle temperature, T_D and m^*T_D for the f4 orbit 120

6.7 A plot of $\ln(A_p/p^{1/2})$ against the harmonic number p for the f4 orbit in $Ce_xLa_{1-x}IrIn_5$.....121

Reproduced with permission of the copyright owner. Further reproduction prohibited without permission.

ABSTRACT

The de Haas van Alphen (dHvA) effect, which measures the oscillatory component of the magnetization, in several $Ce_xLa_{1-x}MIn_5$ (M = Rh, Co, Ir) alloys for $0 \leq x \leq 1$ has been studied in detail using torque, pulse field and field modulation techniques. The frequencies, associated extremal cross sectional areas of the Fermi surface and effective masses of each sample throughout each of the series are reported.

The energy band calculations of $CeRhIn_5$, $CeCoIn_5$ and $CeIrIn_5$ assume that the 4*f* electrons in Ce are completely delocalized and these electrons make a significant contribution to the topology of the Fermi surface. It is observed that the band calculations are in agreement with the dHvA measurements for $Ce_xLa_{1-x}CoIn_5$ and $Ce_xLa_{1-x}IrIn_5$. However, the dHvA measurements on $Ce_xLa_{1-x}RhIn_5$ show that the 4*f* electrons are entirely localized in $CeRhIn_5$. The measurements show that the effective masses of carriers for each series vary slowly at low concentration and a dramatic increase is observed at high concentrations for B || [001]. In addition, for Co and Ir series at low concentrations ($x \leq 0.25$), the mass enhancement agrees with the existing theory. The Dingle temperature measurements suggest that the replacement of La by Ce increases the scattering rate of the electrons for M = Co, Ir, not for M = Rh. For x = 0.5 and higher concentrations dHvA measurements on $Ce_xLa_{1-x}RhIn_5$ show that dHvA oscillations originate from only one spin direction. However, dHvA measurements on Co and Ir series for $x \leq 0.10$ show that there is no single spin dependence contributing to the oscillations.

Reproduced with permission of the copyright owner. Further reproduction prohibited without permission.

CHAPTER 1

GENERAL INTRODUCTION

Historically, the development and advancement of societies have depended directly on the people to produce and manipulate materials to fill their needs. One of the keys to understanding materials is the understanding of the behavior of electrons in solids. The electron theory of solids is capable of explaining optical, magnetic, thermal as well as electrical properties of materials. For an understanding of the electronic properties of materials, many models have been developed during the past hundred years. Although both classical and quantum mechanics have remarkable success in describing the behavior of single particle problems, it is still a problem to directly apply the rules of quantum mechanics to an assemble of about 10^{23+x} interacting electrons and nuclei in order to calculate the properties of solids. In the following sections, we will briefly review some important models used to explain electron's behavior in metals.

1.1 Free Electron Model

One of the most important and simplest models, known as the free electron model, was developed by P. Drude at the turn of last century [1]. The basic assumption in Drude's theory is that within a metal the valance electrons (conduction electrons) of the atoms are free and all forces between conduction electrons and ionic cores are neglected. That is, each atom gives up its valance electrons, which are then free to move like an ideal gas and the energy of these electrons is entirely kinetic. This theory is based on the kinetic theory of an electron gas in a solid. In the original Drude theory a single

Reproduced with permission of the copyright owner. Further reproduction prohibited without permission.

average energy, average velocity and so on, were used rather than any statistical distribution. Later, H. Lorenz [2] developed Drude's idea and applied the Maxwell-Boltzman distribution law to the gas of electrons. According to Drude-Lorentz theory, a metal was considered a potential box filled with a gas of free electrons obeying Maxwell-Boltzman statistics. Although this model is not absolutely correct, it helped in explaining the phenomena of electric and thermal conduction and their interaction, expressed by the Widemann-Franz Law. The successes of classical theory are still used today as a quick practical way to form simple pictures and rough estimates of properties of metals. However, the theory failed to explain why the free electrons did not make a large contribution to specific heat and later, when electron spin had been discovered, it was not clear why the free electrons did not contribute to the paramagnetic susceptibility by varying as 1/T. Shortly after the discovery of the Pauli exclusion principle [3], in 1926, E. Fermi and P. Dirac postulated that at T = 0 K in a system of N free electrons, the energy states are occupied with electrons up to the Fermi energy E_F and only two electrons (spin up and spin down) can occupy each energy level [4,5]. That is, at absolute zero, the states above the Fermi level are empty. Hence, there is a an energy boundary between occupied and unoccupied states in k-space at T= 0 K. This boundary defines a surface called the Fermi surface which is a surface of constant energy. For free electrons, the Fermi surface is a sphere called the Fermi sphere. By using the Schröndinger equation, the energy level of electrons at the Fermi level is given by [6]

$$E_F = \frac{\hbar^2 k_F^2}{2m_e} \quad , \tag{1.1}$$

where m_e is the mass of the free electron.

Reproduced with permission of the copyright owner. Further reproduction prohibited without permission.

So far, we talked about the ground sates (i.e., T = 0 K) of the electron gas. What happens as the temperature is increased? The answer to this question is given by the Fermi-Dirac distribution function. The kinetic energy of an electron gas increases as the temperature increases, so that, some energy levels are occupied which were empty at absolute zero and the probability of occupancy of a level of energy ε at temperature T is given by the Fermi-Dirac function [6] as

$$f(\varepsilon) = \frac{1}{e^{(\varepsilon-\mu)/k_B T} + 1}, \tag{1.2}$$

where μ is the chemical potential which is equal to the Fermi energy at T = 0 K and k_B is the Boltzmann constant.

In 1927, Pauli [7] removed the difficulty about spin susceptibility by using Fermi-Dirac statistics. The calculated paramagnetic susceptibility then becomes independent of the temperature and roughly comparable to experimental value. In 1928, Sommerfeld [8] applied quantum mechanics to the free electron gas of metals and he showed that the application of the Fermi-Dirac distribution rather than Maxwell-Boltzman distribution removed the specific heat difficulty and other unsatisfactory features of Drude's theory. In this model, a metal crystal is described by a three dimensional potential box with an infinite barrier at the surface; in other words, the electrons are unable to leave the crystal. The time independent Schröndinger equation for the electron in the one electron approximation (ignoring any interaction between valance electrons due to their Coulomb repulsion, i.e., each electron is treated as an independent particle.) in the infinitive square well

$$-\frac{\hbar^2}{2m}\nabla^2\Psi(\mathbf{r}) + V(\mathbf{r})\Psi(\mathbf{r}) = E'\Psi(\mathbf{r}). \tag{1.3}$$

Reproduced with permission of the copyright owner. Further reproduction prohibited without permission.

where the potential V(**r**) is regarded as a constant potential, V_0. This equation can be solved using a plane wave $\Psi(r) = e^{i\mathbf{k}\mathbf{r}}$. Then possible energy states are found as

$$E = \frac{\hbar^2 k^2}{2m} \quad . \tag{1.4}$$

That is, a representation of allowed values in three-dimensional k-space yields constant energy surfaces, i.e., $E = \frac{\hbar^2 k^2}{2m}$ = constant, and they are spherical. It is obvious that Sommerfeld theory is an oversimplification by neglecting the periodic atomic potential.

Its is worthwhile here to talk about density of states g(E), i.e., the number of energy states per unit energy interval. In three dimensions, the number of states between E and E + dE is given by

$$g(E) = \frac{V}{2\pi^2}\left(\frac{2m}{\hbar^2}\right)^{\frac{3}{2}} E^{1/2} \quad , \tag{1.5}$$

where V is the volume of the sample.

1.2 Band Theory of Metals

Sommerfeld's model gives us a good insight into heat capacity, thermal conductivity, electrical conductivity, magnetic susceptibility, field emission, thermodynamic emission and electrodynamics of metals. But the model fails to help us with other large questions such as; distinction between metals, semimetals, semiconductors, insulators, superconductors and heavy fermions; the occurrence of positive values of the Hall coefficient; magnetoresistance effect and many other transport properties. Real crystals differ from Sommerfeld's model in that the potential of an electron in the metal is periodic rather than constant. That is, electrons in the metal move in a periodic potential V(**r**). But the construction of V(**r**) is a very complicated

Reproduced with permission of the copyright owner. Further reproduction prohibited without permission.

many body problem involving all nuclei and all electrons of all atoms in a metal. For practical purposes, it is convenient to separate electrons into ion-core electrons, which are regarded as being localized on the individual ions, and conduction electrons, which are regarded as being free to move throughout the metal in delocalized states. Although this division between localized ion-core electrons and delocalized or itinerant conduction electrons is quite sharp for many metals (alkali metals, for example) it shouldn't be considered that it is always true for all metals. By accepting this division of electrons, the main contribution to the potential $V(\mathbf{r})$ includes: electrostatic potential due to the ion cores, electrostatic potential due to the other conduction electrons, exchange and correlation among the ion core electrons, exchange between ion core electrons and conduction electrons, correlation between ion core electrons and conduction electrons, exchange and correlation among the conduction electrons, and spin orbit coupling [9]. The electrostatic potential due to the ion cores, and electrostatic potential due to the other conduction electrons, give the largest contribution to $V(\mathbf{r})$, while the exchange and the correlation effects give significant extra contribution to $V(\mathbf{r})$. The magnitude of the spin-orbit coupling contribution depends very much on the metal in consideration. Generally, it is very small for metals of low atomic number, but it becomes significant for metals for high atomic number [9]. As we discussed in section 1.1, it is quite straight forward to solve the one electron Schröndinger equation in the case when $V(\mathbf{r})$ is equal to zero or constant, but, it is very difficult to solve the Schröndinger equation when the realistic non zero potential $V(\mathbf{r})$ is considered. It is also difficult to construct the realistic potential $V(\mathbf{r})$ due to the many body problem as we discussed before. A number of a attempts have been done over the years to construct the realistic non-zero potential $V(\mathbf{r})$ and solve the

Reproduced with permission of the copyright owner. Further reproduction prohibited without permission.

Schrondinger equation with V(**r**). Some of them are the nearly free electron model, tight-binding model, Kronig-Penney model, cellular model, pseudopotential model, Wigner-Seitz model, Green's function model, muffin-tin potentials, etc. We will not give any treatments of these models but the readers who are interested in them can review the books given in references [6, 9-13]. However, we will talk about general formation of band structure in crystals qualitatively by using the one electron model.

The simplest quantum mechanical view of an electron in a crystal is that of a single electron in a perfectly periodic potential which has the periodicity of a lattice. In this one electron model of a solid, the periodic potential may be thought of as arising from the periodic charge distribution associated with the ion cores situated on the lattice sites, and the average potential contribution due to all other free electrons, so that the interaction of the single electron with all the others is accounted for in an average sense [14]. So we can therefore, describe each electron by the same Schröndinger equation

$$[-\frac{\hbar^2}{2m}\nabla^2 + V(\mathbf{r})]\Psi(\mathbf{r}) = E\Psi(\mathbf{r}) \qquad (1.6)$$

where $V(\mathbf{r}) = V(\mathbf{r}+\mathbf{T})$ and $\mathbf{r}$ is the position vector, $\mathbf{T}$ is any translation of Bravais Lattice given by $\mathbf{T} = n_1\mathbf{a}+n_2\mathbf{b}+n_3\mathbf{c}$, where **a**, **b**, **c** are the lattice parameters of the primitive cell. The solutions of the one electron wave equation for an infinite periodic potential are known as Bloch waves and in 3-dimensions they are given as

$$\psi(\mathbf{r}) = u(\mathbf{r})e^{i\mathbf{k}\mathbf{r}} \qquad (1.7)$$

where $u(\mathbf{r})=u(\mathbf{r}+\mathbf{T})$ is a function which has the periodicity of the lattice. Thus the solutions (the Bloch functions) are traveling plane waves modulated by the function $u(\mathbf{r})$ with the periodicity of the potential, which varies with the period of lattice. Such waves are called Bloch waves. The solution of the above equation in one dimension is given by

Reproduced with permission of the copyright owner. Further reproduction prohibited without permission.

Floquet's theorem [15]. (Analytic solutions can be found to the one-dimensional periodic potential problem in a number of cases. Some of these are (a) an array of narrow deep potential wells [16], (b) an array of potential wells of a finite width and depth the Kronig-Penney model [17], (c) a sinusoidal potential of the form $V(x)=A \sin(2\pi x/a)$ where the solutions are in terms of Mathieu functions [18] and (d) the cusped potential formed by an array of inverted parabolas for which the solutions are in terms of confocal hyper-geometric functions [19].)

Because of the lattice periodicity, the eigenvalues of equation (1.6) break up into allowed and forbidden energy bands. Thus allowed energy levels of electrons are grouped into bands and these bands are separated by regions called forbidden bands. The existence of these forbidden bands help us to understand the nature of insulators and semiconductors as well as metals. Simply, in one-dimension, the energy versus k curve, between the boundaries $-\pi/a$ and $+\pi/a$, corresponds to the first electron band. This region in k-space between $-\pi/a$ and $+\pi/a$ is called the first Brillouin zone. Accordingly, the area between π/a and $2\pi/a$ and also between $-\pi/a$ and $-2\pi/a$ which corresponds to the second band, is called the second Brillouin zone, and so on. In three dimensions, the range of $\mathbf{k}$ values included in the Brillouin zone depends on the crystal symmetry. For instance, for a simple cubic lattice, the first Brillouin zone is a cube with equal extensions in k_x, k_y and k_z between $-\pi/a$ and $+\pi/a$. For other crystal structures, the geometry of the Brillouin zone can be determined from the crystal symmetry. The first Brillouin zone corresponds to the unit cell of the reciprocal lattice. One simple result is that the face centered cubic crystal has a Brillouin zone with a body centered cubic symmetry. Since the energy bands are not alike in different directions in $\mathbf{k}$-space, the energy band structure

Reproduced with permission of the copyright owner. Further reproduction prohibited without permission.

of the solids is usually obtained for **k** pointing in various principal directions (directions of high symmetry); these directions are generally labeled with Greek letters and their intersections with the zone are labeled with the Latin letters. Because of discrete values in **k**, the Fermi surface is not spherical any longer like in the free electron gas approximation, but it is distorted. If the Fermi surface is larger than the Brillouin zone, then the Fermi surface is intersected by the zone boundary and occupies more than one zone. In order to understand the electronic properties of metals, we need to talk about the Fermi surface of metals as well as band structure.

1.3 Fermi Surface of Metals

The Fermi surface of a metal holds the key to understanding and calculating the various properties of the material because many of the electronic properties of materials such as optical, electrical, or magnetic properties are related to the location of the Fermi surface within the band. The Fermi surface can be defined as a constant energy surface in **k**-space which separates occupied and unoccupied states at T = 0 K [9]. We should emphasize that the Fermi surface is not a surface in real space but an abstract surface in reciprocal space. As we have already mentioned in section 1.1, for the free electron case, the Fermi surface is a sphere centered at **k** = 0, but in real metals the Fermi surfaces are different from the ideal spherical surface of free electron model. In alkali metals, the Fermi surface is nearly a sphere and this sphere is smaller than the first Brillouin zone. (If the Fermi surface is larger than the first Brillouin zone, then the Fermi surface is often represented by the reduced zone scheme, where each branch of the Fermi surface is reflected into the first Brillouin zone.) In noble metals (Cu, Ag, Au), the Fermi surface is distorted away from the free electron sphere in the [111] direction with the

Reproduced with permission of the copyright owner. Further reproduction prohibited without permission.

eight necks touching the hexagonal faces of the first Brillouin zone. For transition and rare earth metals, the Fermi surface is much more complex than an ideal sphere because no simple free electron model can be used. This surface is very significant because all the conduction electrons lie on the Fermi surface and only those electrons on the Fermi surface can participate in the transport process and thermal excitations of metals. Because they obey the Fermi-Dirac statistics, electrons well below the Fermi level can not be excited easily into unoccupied higher energy levels. Effectively, in low lying quantum states, electrons do not contribute significantly to the measurable properties of a metal in any direct way other than to support the higher energy electrons at the Fermi level. All the conduction electron in a metal reside near the Fermi level. Therefore, any experimental technique used to measure the Fermi surface provides important details about the conduction phenomena in any given metallic system. Many experimental methods have been developed for studies of Fermi surfaces of metals. Important methods include: anomalos skin effect [20, 21], cyclotron resonance [22] , magnetoresistance [23], ultrasonic propagation in magnetic fields, optical reflectivity [24, 6], and de Haas-van Alphen effect [25]. Among these techniques, the de Haas-van Alphen (dHvA) effect is the most powerful and sensitive method for probing the electrons at the Fermi surface. In this work, measurements and analysis of the dHvA effect on $Ce_xLa_{1-x}MIn5$, (M = Rh, Co, Ir, $0 \leq x \leq 1$) will be presented.

1.4 Effective Mass

The mass of the electron given in Eqs. (1.1) and (1.4) is the free electron mass measured in free space. However, experimental facts indicate that for some solids the mass is larger while for others it is slightly smaller than the free electron mass. There are

Reproduced with permission of the copyright owner. Further reproduction prohibited without permission.

also some crystals in which the effective mass may be anisotropic and it may even be negative. The experimentally determined electron mass is usually called the effective mass, m*. The reason of deviation of the effective mass from the free electron mass is usually attributed to interactions between the drifting (conduction) electrons and the atoms in the crystal. For instance, an electron accelerated in an electric field might be slowed down slightly due to collisions with some atoms. In that case, the ratio of effective mass of the electron to the free electron mass m*/m is larger than one [26]. The expression for effective mass m* is given as [27]

$$\frac{1}{m^*} = \frac{1}{\hbar^2}\left(\frac{d^2E}{dk^2}\right) , \tag{1.8}$$

or

$$\left(\frac{1}{m^*}\right)_{ij} = \frac{1}{\hbar^2}\left(\frac{d^2E}{dk_i dk_j}\right) , \tag{1.9}$$

where E is the energy of electron. The equation (1.9) is the effective mass tensor which is generalized to three-dimensional anisotropic energy surfaces. As can be seen in the above equations, the effective mass is inversely proportional to the curvature of an electron band. Thus, effective mass depends on the electron's **k** value. In addition to this, m* also depends on band width. If the band width is narrow, and the gap between the bands is large, then d^2E/dk^2 is relatively small, and m* is large. Materials such as the transition metals and rare earth metals tend to have this property. Some experimental methods to measure effective mass directly include: cyclotron resonance, anomalous skin effect, magnetoresistance, and de Haas-van Alphen effect [10]. In this study, the effective masses of $Ce_xLa_{1-x}MIn_5$ alloys were measured by using the de Hass-van Alphen effect.

Reproduced with permission of the copyright owner. Further reproduction prohibited without permission.

1.5 The Fermi Liquid

In the free electron model, we have considered a system of noninteracting bare electrons, which is called a Fermi gas. In fact, the conduction electrons in a metal interact with each other and this interacting system is called a Fermi liquid. The effect of interacting electron systems were discussed by Landau in 1957 [28]. Landau considered the free electron gas and the electron-electron interaction and showed that the Coulomb interaction between one electron and all the others is strongly reduced due to screening by the free electrons. In addition, Landau showed that the electron-electron interaction is still small, as long as electrons within k_BT of E_F are considered. Thus, the free electron gas idea is valid with a few changes. In place of bare electrons, the quasi-particles (that may come from screening) whose mass can be different from that of free electron should be considered in a system of many electrons. Even though Fermi liquid theory is the most successful approach for describing the interacting electron system, some experiments done in recent years in strongly correlated electron systems (this term is used to describe conditions when the Coulomb repulsion between the electrons strongly inhibits their motion) showed that there is a limit and to the validity of Fermi liquid theory. Some of these materials include: high temperature superconductors, heavy fermion compounds, Luttinger liquids and the materials exhibiting the fractional quantum Hall effect. Many of them are still far from understood and alternative models need to be explored in order to describe their many-body ground state.

1.6 Magnetic Properties of Solids

In this section, we will briefly review some basic concepts in magnetism that we will use frequently in the following chapters of this dissertation. The magnetic response

Reproduced with permission of the copyright owner. Further reproduction prohibited without permission.

of most magnetic solids involves the orientation of the magnetic dipoles contained in the solid. These magnetic dipoles or magnetic moments, *m*, consist of the electron spin dipole moments, electron orbital dipole moments, and the change in the orbital dipole moment induced by an applied magnetic field. If an external magnetic field **H** is applied to a piece of material, it usually responds in some way, so that the total field **B** inside the material does not remain equal to **H.** Inside a magnetic material, the total field, **B,** consists of the external magnetic field, **H**, plus a contribution to the magnetic field which is due to presence of matter,

$$\mathbf{B} = \mathbf{H} + 4\pi\mathbf{M}\,, \tag{1.10}$$

where **M** is called the magnetization of the material and it is defined as the magnetic dipole moment per unit volume or per unit mass. Magnetic properties of the materials are often discussed in terms of the susceptibility. In other words, the response of the material to the applied magnetic field can be described by its susceptibility, χ, which is a characteristic constant of material and it is expressed as [6]

$$\chi = \frac{\partial M}{\partial H}. \tag{1.11}$$

In general, five main types of magnetic behavior are observed in bulk materials. We will briefly describe each of these behaviors in the following paragraphs.

Diamagnetism: Diamagnetism is produced by the effect of an applied magnetic field on the orbital motion of the electrons. The diamagnetic effect can be deduced from Lenz's Law of electromagnetic induction. According to Lenz's law, the change of flux through an electrical circuit induces an e.m.f which produces a current in such a direction as to oppose the flux change. In a resistanceless circuit, such as in a superconductor or in an electron orbit within an atom, the induced current persists until

Reproduced with permission of the copyright owner. Further reproduction prohibited without permission.

the field is removed. Thus the effect of applying a magnetic field is to induce a dipole moment in a direction opposite to that of the field. In other words, for perfect diamagnetic materials χ = -1. The diamagnetic susceptibility per unit volume is given by classical Langevin equations [10]

$$\chi = -\frac{\mu_0 NZe^2}{6m_e} < r^2 > , \qquad (1.12)$$

where μ_0 is the permeability of free space, N is the number of atoms per unit volume, e is the charge of the electron, m_e is the mass of the electron, and r is the orbital radius. The inert gases, polyatomic gases such as H_2 and N_2, and ionic solids like NaCl are the best examples for diamagnetism. Superconductors are known as perfect diamagnets. In dielectric solids, the magnetic contribution of the ion cores is roughly given by the Langevin result. The contribution of conduction electrons to diamagnetism is more complicated and the study of diamagnetism has been very restricted except for the special case of the de Haas van Alphen effect.

Paramagnetism: In contrast to diamagnetism, paramagnetism usually only occurs when the atoms (or ions) have a net magnetic dipole moment due to orbiting electrons. These magnetic moments are randomly oriented and thus they mutually cancel one another. As a result, the net magnetization is zero. However when an external field is applied, the individual magnetic moments tend to turn into the field direction. The external magnetic field also tries to turn the unfavorably oriented spin (spin up and spin down in each electron state) moments in the direction of the external field. The alignment of electron spins within an atom and neighboring atoms is governed by a special type of interaction, known as the exchange interaction. But this spin paramagnetism is generally very weak and slightly temperature independent. Although magnetic dipole moments

Reproduced with permission of the copyright owner. Further reproduction prohibited without permission.

align with the external field, thermal agitation counteracts this alignment. The temperature dependence of many paramagnetic materials is governed by the Curie-Weiss law [10]

$$\chi = \frac{C}{T - \theta}, \tag{1.13}$$

where C is called the Curie constant and θ is another constant which has the same units as temperature. Some of the metals, the rare earth elements and salts of transition metals like carbonates, sulfates and chlorides obey the Curie-Weiss law quite well. A paramagnetic material has a positive contribution to the susceptibility, that is, the magnetic moment increases with increasing magnetic field.

Ferromagnetism: A ferromagnetic substance is one that possesses a spontaneous magnetization, i.e. it is magnetized even in the absence of a magnetic field. The most common ferromagnets are the metals iron, cobalt, nickel with incomplete d shells, some of their alloys and rare earth elements with an incomplete f shell, mostly at lower temperatures. In these materials, strong interaction (exchange interactions) between atomic magnetic moments cause them to line up parallel to each other in regions called magnetic domains. When there is no external applied field the orientations of domain magnetizations are random, but when a field is present, they tend to orient themselves parallel to field. Ferromagnetic materials behave as ordinary paramagnets at high temperatures, but acquire a permanent magnetic dipole moment below a critical temperature which is known as the Curie Temperature T_c. That is, at temperatures greater than T_c, the substance has a temperature dependent paramagnetic susceptibility. But, below T_c, the exchange interaction (interaction between spins on neighboring atoms) is able to overcome the disorder due to the thermal energy of the ions, so that neighboring

Reproduced with permission of the copyright owner. Further reproduction prohibited without permission.

spins line up parallel with one another even in the absence of an external magnetic field. This classical treatment of the exchange interaction was proposed by Pierre Weiss [6], who suggested that a high internal magnetic field $\mathbf{B}_{ex}$ exist in any ferromagnetic material and be directly proportional to the magnetization in the material. This is also known as mean field theory, but it is inadequate at low and high temperatures. The physical origin of ferromagnetism can be understood by using quantum mechanics.

Antiferromagnetism: Just as ferromagnets, antiferromagnetic materials display a spontaneous alignment of magnetic moments below a critical temperature, known as the Néel temperature T_N. However, neighboring dipole moments align in an antiparallel fashion. Above the Néel temperature T_N, antiferromagnetic materials are paramagnetic, thus, antiferromagnetic materials obeys a Curie-Weiss law above the Néel temperature but with the opposite sign of θ, i.e

$$\chi = \frac{C}{T + \theta} . \tag{1.14}$$

The negative sign is used for θ because the exchange interaction tends to destroy the alignment parallel to the external field. Below T_N, the exchange interaction dominates over the thermal effects but, as the temperatures rises, thermal effects become more significant and the cancellation of magnetization due to antiferromagnetic arrangement is decreased. At the Néel temperature, the antiferromagnetic coupling is totally overcome by thermal agitation, and materials become essentially paramagnetic at higher temperatures. The Néel temperature commonly lies far below room temperature, so that it is often necessary to carry susceptibility measurements down to quite low temperatures to discover if a given substance, paramagnetic at room temperature, is actually

Reproduced with permission of the copyright owner. Further reproduction prohibited without permission.

antiferromagnetic at some lower temperatures. Antiferromagnetic substances have a small positive susceptibility at all temperatures. Most antiferromagnetics are ionic compounds, namely, oxides sulphides, chlorides and the like. All the rare earths are paramagnetic at room temperatures and above, but most of them are antiferromagnetic at low temperature. Even though antiferromagnets are of considerable scientific interest they have limited practical applications.

Ferrimagnetism: In some crystals with a more complicated structure, the magnitude of the magnetic moments on each of the two sub lattices is not exactly the same. Thus when spontaneous antiparallel alignment occurs, the material, instead of having zero magnetic moment, has a net permanent magnetization. This phenomenon is known as ferrimagnetism. To explain the spontaneous magnetization in ferrimagnets, Néel proposed that two sublattices should exist in these materials, like in antiferromagnetics, each of which contains ions whose spin are aligned parallel to each other. The crucial point is that each of the sublattices contain unequal magnetic moments. This causes some of the magnetic moments to remain uncancelled. As a consequence, a net magnetic moment results. Their spontaneous magnetization disappear above a certain critical temperature T_c, also called the Curie temperature and they become paramagnetic. The most common material which shows this behavior is magnetite, Fe_2O_4. Ferrites have great technical importance because of their high electrical resistivity.

1.7 Organization of the Dissertation

The first chapter of this dissertation is organized as a review of the electron theory of metals, although this work mainly focuses on de Haas-van Alphen (dHvA) effect of

Reproduced with permission of the copyright owner. Further reproduction prohibited without permission.

$Ce_xLa_{1-x}MIn_5$ alloys (M = Rh, Co, Ir). In this chapter, free electron theory, band theory, Fermi surface, effective mass, Fermi liquid theory, and magnetism in solids were reviewed qualitatively in order to understand the physical properties of metals.

Chapter 2 focuses on the heavy fermion materials. The substitution of one element for another in a compound and subsequent observations of the changes in properties is one of the most powerful tools to study materials and in this work, the light metals $LaMIn_5$ was used as host metals for $Ce_xLa_{1-x}MIn_5$ compounds. In this chapter, we will discuss some of the most important heavy fermion compounds and their physical properties. Some of the models that attempt to explain the interaction of f-electrons with the conduction electrons will be briefly discussed in order to provide the theoretical background for the measurements described in Chapter 4, 5 and 6.

In Chapter 3, the de Haas-van Alphen (dHvA) effect, the most powerful technique to study Fermi surface of the materials, will be presented in a qualitative fashion, with some important mathematical relationships. The semi classical Lifshitz-Kosevich equation will be presented for the theory of dHvA oscillations. This Chapter will also illustrate the experimental techniques used to study dHvA effect during this research. Torque measurement, pulse field measurement and field modulation measurement are the backbone of this study.

Chapter 4, 5 and 6 will describe the main experimental results obtained during this work. As the result of dHvA measurements, the frequencies and effective masses of $Ce_xLa_{1-x}MIn_5$ ($0 \leq x \leq 1$) compounds are obtained. The concentration dependence of

Reproduced with permission of the copyright owner. Further reproduction prohibited without permission.

dHvA frequencies and effective masses, Dingle temperature measurements, and spin dependence of carriers of $Ce_xLa_{1-x}MIn_5$ compounds are reported in these Chapters.

Finally, the most important new results and conclusions of this work will be summarized again shortly in Chapter 7.

Reproduced with permission of the copyright owner. Further reproduction prohibited without permission.

CHAPTER 2

HEAVY FERMION MATERIALS

2.1 Overview

The history of heavy fermion physics in *f* electron systems began about 25 years ago with the study of $CeAl_3$ compound [29] and ever since, an increasing number of studies have been done on the heavy fermion compounds. The term heavy fermion system is used to describe metallic compounds and alloys which contain $4f$ and $5f$ ions (i.e., rare-earth or actinide ions, in particular Ce, U, Yb). In these systems, very large effective conduction electron masses are observed at low temperatures. These materials are electrically conducting materials which have a large specific heat coefficient, γ, (electronic specific heat coefficient) greater than 400 $mJ/molK^2$ [30], which is typically about 100 times larger than in most metals. This large specific heat coefficient is associated with large effective masses of the conduction electrons.

At room temperature and above, these systems behave as a weakly interacting collection of the *f*-electron moments and conduction electrons with quite ordinary masses. But at low temperatures the *f*-electron moments become strongly coupled to the conduction electrons and to one another, and the conduction-electron effective mass is typically 10 to 100 times the bare electron mass [30]. At low temperatures, they show diverse form; while some remain normal, some become superconducting or antiferromagnetic [31-37]. In addition, in these materials with lowering temperatures, an antiferromagnetic transition follows the superconducting transition [31] and

Reproduced with permission of the copyright owner. Further reproduction prohibited without permission.

some of these materials show superconductivity only under high pressure [38-40]. Some of the most interesting heavy fermion systems with large values of γ at zero magnetic field are given in Table 2.1. The Ruderman-Kittel-Kasuya-Yosida (RKKY) interaction [41-43] and Kondo effects [44] are two terms used frequently for the heavy fermion systems. It is worth mentioning the meaning of these terms qualitatively here.

The RKKY interaction is the indirect exchange interaction between localized moments themselves, and it can be either antiferromagnetic or ferromagnetic. This effect can be explained as follows. In many systems conduction electrons and localized electrons interact with each other. This is generally referred as an *s-d* or *s-f* exchange. For example, in rare metals, the conduction electrons (for rare earth metals, the 6*s* electrons have the weakest binding and therefore make up the conduction electrons) experience an exchange interaction with the partially filled 4*f*-shell and as a result, the conduction electrons become magnetically polarized. Because these conduction electrons occupy band states and extend throughout the crystal, they serve through their own polarization to align the localized 4*f* moments on the atoms. In other word, the spin information from the localized 4*f* electrons of one atom is transmitted to another. This is known as the RKKY interaction. The localized picture of the 4*f* electrons in the rare earth compounds can be understood on the basis of this RKKY interaction. Although there is a direct dipole-dipole interaction between 4*f* electrons, it is very weak. The interesting aspect of the RKKY interaction is that it has a longer range than just the nearest neighbor distances.

The Kondo effect is also a consequence of the interaction of localized magnetic moments with conduction electrons. If a magnetic impurity (partially filled *d*- or *f*-shell, such as Mn, Fe, or Ce, U) is put in a non magnetic host material (Cu, Au or Al,

Reproduced with permission of the copyright owner. Further reproduction prohibited without permission.

Table 2.1 Observed transition of some of the most interesting heavy fermion system. γ is the specific heat coefficient.

Material	γ (mJ/mol K^2)	Superconductive	Tc(K)	Antiferromagnetic	No Ordering down to 0.02K	Ref.
$CeCu_2Si_2$	1000	Yes	0.64	No	No	[45]
$CeAl_3$	1620	No	-	No	Yes	[29]
$CeCu_6$	1600	No	-	No	Yes	[46,30]
UPt3	450	Yes	0.5	No	No	[35]
UBe_{13}	1100	Yes	0.93	No	No	[35,47]
$CeRh_2Si_2$	50	Under Pressure	0.35	Yes	No	[38,48]
YbPtIn	430	No	-	Yes	No	[49]
CeB_6	260	No	-	Yes	No	[50,51]
$CeIn_3$	130	Under Pressure	0.15	Yes	No	[39,52]
$CeRhIn_5$	400	Under Pressure	2.1	Yes	No	[40,53]
$CeCoIn_5$	290	Yes	2.3	No	No	[45,55]
$CeIrIn_5$	720	Yes	0.40	No	No	[54,56]
Ce_2RhIn_8	400	No	-	Yes	No	[53]

Be) the resistivity shows a minimum at low temperatures. This minimum resistivity in magnetic alloys was explained by Kondo [44]. The magnetic impurities act as scattering centers for the conduction electrons and electron scattering from these magnetic impurities makes a contribution to the resistivity. Scattering can be thought as spin flip scattering between the conduction electrons and the localized spin, i.e., the spin of conduction electrons and spin of impurities flip because of the interaction. Kondo showed that the resistivity appears in second order perturbation theory and at low temperatures the resistivity shows a logarithmic divergence (Fig 2.1) that arises from the spin flip scattering of the conduction electrons by the impurities. Although Kondo

Reproduced with permission of the copyright owner. Further reproduction prohibited without permission.

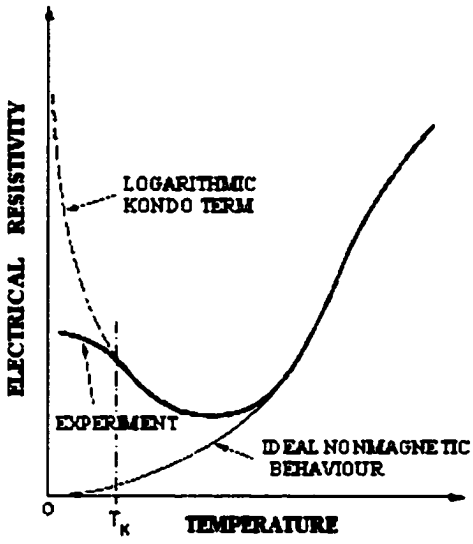

Figure 2.1: A schematic view of the Kondo effect observed in dilute systems at low temperatures [57]. The logarithmic contribution to the resistivity arises from spin-flip scattering.

provided an explanation of the resistance minimum effect, he did not provide a complete understanding of the term containing a factor log(T) in resistivity. As seen in Figure 2.1, the logarithmic Kondo term is divergent and leads to a singularity at T = 0. This is physically unacceptable because when the temperature approaches the absolute zero the resistivity reaches infinity. There are no metals or alloys which show such behavior. This divergence of the logarithmic term in the limit $T \rightarrow 0$ is known as the Kondo problem. Furthermore, experiments show that this logarithmic behavior in resistivity is followed only above a certain characteristic temperature T_K (the Kondo temperature); below this temperature, the resistivity is relatively independent of temperature. The perturbation theory provides a good description of the magnetic impurity system for $T \geq T_K$ but it could not be extended to the region $T \leq T_K$. T_K varies enormously from compound to compound. Heavy fermions can be considered as a lattice of magnetic atoms interacting

Reproduced with permission of the copyright owner. Further reproduction prohibited without permission.

with a sea of conduction electrons. For that reason the Kondo lattice is often used to describe heavy fermions.

In heavy fermion systems, it is thought that both the RKKY interaction and Kondo effect compete with each other. The competition between the RKKY interaction and the Kondo effect was studied by S. Doniach [58] as a function of the magnetic exchange interaction (J_{cf}) and the electronic density of states ($D(E_F)$) at the Fermi energy. At low temperatures, the RKKY interaction overcomes the Kondo effect and as a result of this, most of the Ce compounds order magnetically. However, some cerium compounds such as $CeCu_6$ [59] and $CeRu_2Si_2$ [60] do not exhibit any long range magnetic order.

The different behavior of the heavy fermion systems at room temperature and low temperature can explain the nature of *f* electrons as we discussed above. As can be seen in the following paragraph, although these systems have been put together in a single class, heavy fermions, the physical properties of these systems such as specific heat, resistivity and magnetic properties, show great diversity from sample to sample. For that reason, making a general conclusion on these systems is still a big challenge for scientists.

2.2 Physical Properties of Heavy Fermions

At temperatures much below the Debye Temperatures in a usual metal at constant volume, the specific heat, C, may be written as the sum of the electronic and lattice contributions:

$$C = \gamma T + \beta T^3 , \qquad (2.1)$$

where γ and β are the constants which are characteristic of the material. Therefore a C/T vs T^2 plot of a normal metal at sufficiently low temperatures has a straight line with an

Reproduced with permission of the copyright owner. Further reproduction prohibited without permission.

intercept γ and positive slope β. For an ordinary metal such as metallic Na, γ is on the order of 1 mJ/mol K^2 at T = 0 K. But the temperature dependence of the specific heat at low temperatures is not the same for all the heavy ferminon compounds. A plot of specific heat for the heavy fermion compounds UPt_3, UCd_{11} and $CeRhIn_5$ is shown in Figure 2.2. As shown in the plots, none of them fit equation (2.1). However, in UCd_{11} and $CeRhIn_5$ the peaks in C_T/T at low temperatures are due to magnetic ordering, i.e. they occur at the Neel Temperature, T_N, and above the region of the ordering temperature they fit $\gamma T+\beta T^3$ very well so that the value of γ can be obtained by extrapolation. In addition to the $\gamma T+\beta T^3$ term, a $T^3 \ln T$ term was detected in the specific heat in UPt_3 [30] as shown in Fig. 2a. But this term was not observed for other heavy fermions like UBe_{13} and $CeCu_2Si_2$. For heavy fermion materials in general, γ rises considerably with decreasing temperature, i.e. γ is not constant, but it is temperature dependent and as temperatures approach zero Kelvin, it reaches very large values. These large values imply very large effective masses of conduction electrons. But temperature dependence is not a characteristic unique to heavy fermion systems. Application of magnetic fields to heavy fermion systems can also affect the specific heat. In general, the value of $\gamma(B)$ tends to decrease with applied field [61-65]. But, there are again some exceptions for systems exhibiting a metamagnetic transaction such as UCd_{11}. As shown in the inset of Fig.2.1b, γ can increase with increasing magnetic field [66].

The magnetic susceptibilty, χ, of all the heavy fermions obeys the Curie-Weiss law, $\chi \propto (T + \theta)^{-1}$ (where θ is the Weiss constant also known as the Curie or Neel temperature), at high temperaures, but at low temperatures, χ displays considerable

Reproduced with permission of the copyright owner. Further reproduction prohibited without permission.

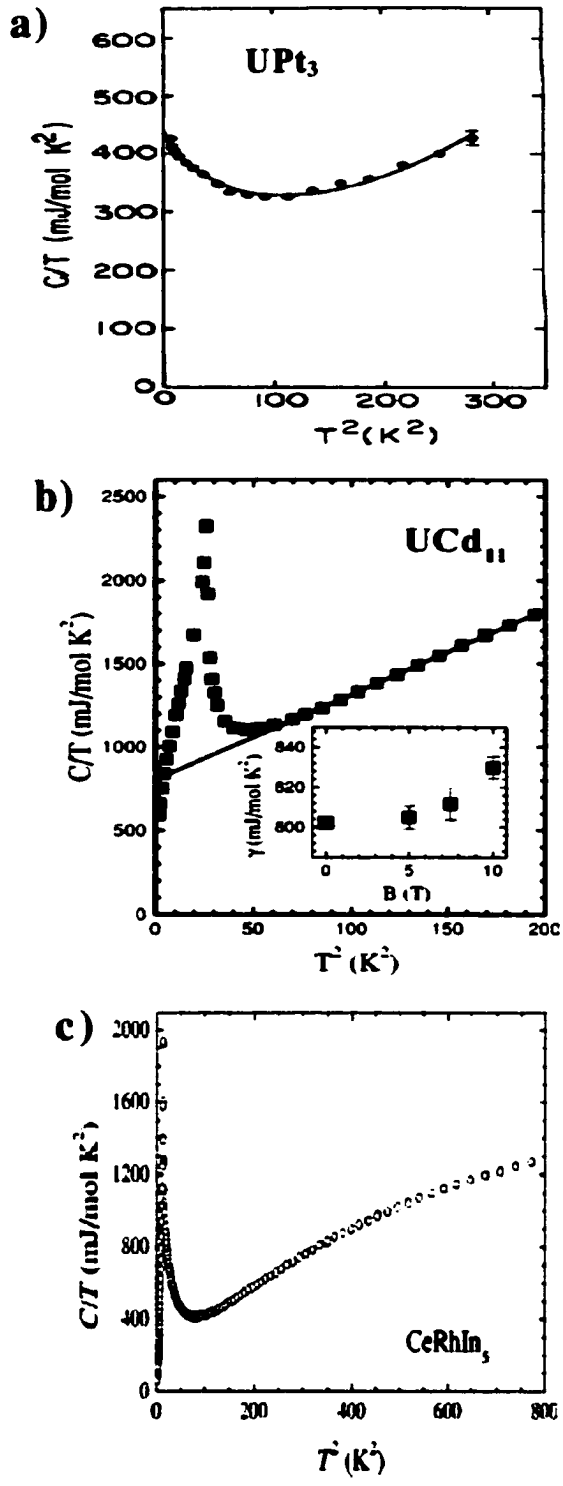

Figure 2.2. C/T as a function of T^2 for a) UPt_3 b) UCd_{11} (The inset shows the field dependence of γ) c) $CeRhIn_5$. These figures were reproduced from Ref. [30, 66, 67].

Reproduced with permission of the copyright owner. Further reproduction prohibited without permission.

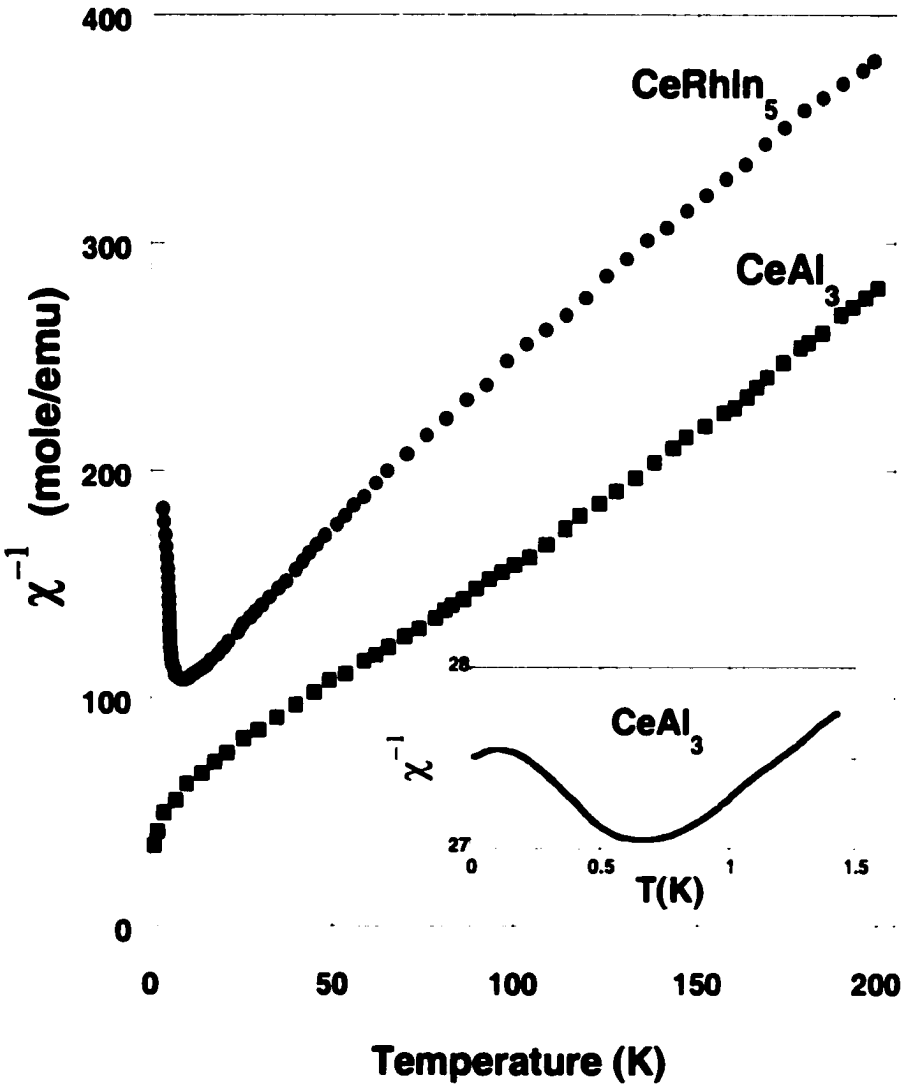

Figure 2.3. Inverse magnetic susceptibility vs temperature for $CeRhIn_5$ and $CeAl_3$. The inset shows saturation indicating itinerant *f* electron behavior below 1.5 K for $CeAl_3$. These plots were reproduced from Ref. [30] and [69].

Reproduced with permission of the copyright owner. Further reproduction prohibited without permission.

variation as shown in Figure 2.3 for $CeAl_3$ and $CeRhIn_5$. In this figure, for $CeAl_3$ the Curie-Weiss law form above 100K corresponds to the local moment behavior of *f* electrons. The inset shows saturation, indicating itinerant *f* electron behavior at very low T. In general, the measured values of low temperature magnetic susceptibility are very large when compared to *d*-electron elements [30].

The electrical resistivity of several heavy fermion compounds as a function of temperature is shown in Figure 2.4 a and b. The resistivity of the ordinary metals, ρ, decreases rapidly with decreasing temperature below room temperature and reaches a finite value known as the residual resistivity ρ_{res}. This residual resistivity originates from the impurities and imperfections in the crystals. But in heavy fermion materials, ρ often increases with decreasing temperature, goes through a maximum and decreases to low values as T goes to zero (UPt_3 and $CeRhIn_5$ again being the exceptions) as shown in Fig. 2.4. The high values in resistivity indicate very strong scattering of the electrons, but decreasing resistivity at low temperature demonstrates that these are not due to imperfections in crystals. Roughly speaking, they are the same as Kondo lattice compounds, increasing as temperature is lowered from room temperature and reaching a maximum, followed by a rapid decrease at low temperatures. Below 10 K the resistivity of many heavy fermion systems displays a rapid variation. For many heavy fermion materials, the resistivity is proportional to T^2 at very low temperatures [30] and this behavior is explained within Fermi Liquid theory. But again there are some exceptions. The resistivity of UPt_3 and $CeRhIn_5$ decreases monotonically with decreasing temperature from room temperature and look like that of normal metals as shown Figure 2.4 a and b. Resistivity of many heavy fermion materials as a function of

Reproduced with permission of the copyright owner. Further reproduction prohibited without permission.

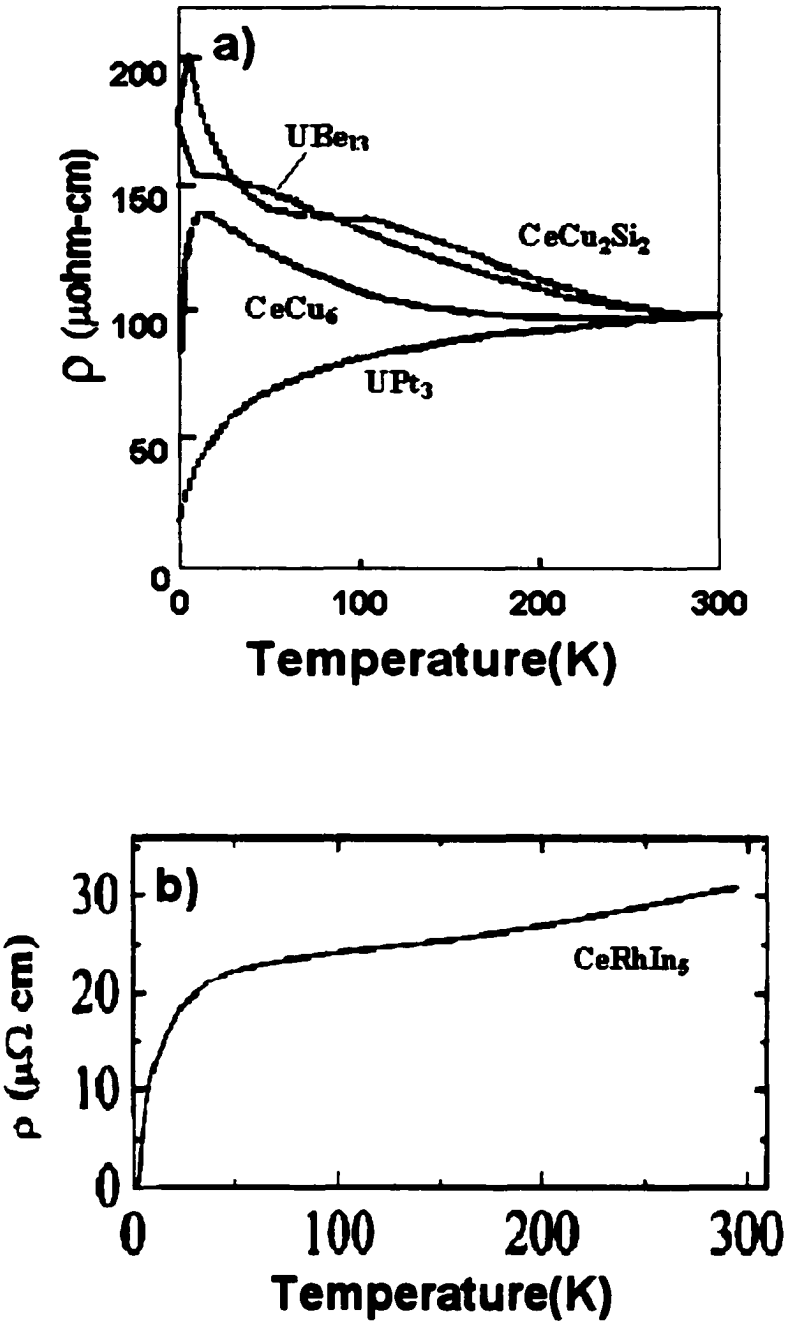

Figure 2.4. Temperature dependence of resistivity a) for several heavy fermion compounds (from Fisk et al, [30]) and b) for $CeRhIn_5$ (from Hegger et al, [40]).

Reproduced with permission of the copyright owner. Further reproduction prohibited without permission.

applied magnetic field has been reported by several workers. Both positive and negative magnetoresistance has been found at different temperatures for many heavy fermion materials [30].

2.3 Heavy Fermion Superconductivity

The first observation of superconductivity in heavy electron metals was made in $CeCu_2Si_2$ by Steglich *et. al.* [45] and then several Ce and U-based heavy fermion superconductors have been found so far. General properties of heavy fermion superconductors include: a large linear coefficient of specific heat of 70 –1000 mJ/mol K, and a superconducting transition temperature in the range of 0.5 to 2 K. [30, 37]. In many cases, the superconductivity develops as unconventional superconductivity. The term unconventional is used to describe the new form of superconductivity which originates in the Coulomb interaction and distinguishes them from the classic form of superconductivity which originates in the interaction with the lattice vibrations well described by the theory of Bardeen, Cooper and Schrieffer (BCS theory) [70]. According to BCS theory, there is an attractive interaction between a pair of electrons (Cooper pair), due to the exchange of virtual photons and this attraction between a pair of electrons creates a lower energy state than two unpaired electrons. Thus, the Fermi energy in a superconducting state is considered to be lower than that for the nonsuperconducting state. This lower state is separated from the normal state by an energy gap. This gap is finite everywhere on the Fermi surface so that many properties, such as the specific heat and transport coefficients, fall exponentially with decreasing temperatures. The orbital part of the wave function associated with the pairs has s-like character, and the gap is essentially constant over the Fermi surface i.e. it is isotropic.

Reproduced with permission of the copyright owner. Further reproduction prohibited without permission.

But after the experimental discovery of the superfluid phases of liquid ^{3}He [71], researches explored the possibility that the pairing might have a more complicated orbital structure (such as *p*-wave or *d*-wave), so that the position of the energy gap at the Fermi energy can vary in both magnitude and phase. In this case, it is considered that many states have nodes of the gap (zeroes of the gap) at points or lines at certain directions on the Fermi surface, and consequently the number of excitations in such states at low temperatures varies as a power of temperature, rather than exponentially. The presence of these nodes of the gap points out the unconventional superconductivity. In other words, the superconductivity in a heavy fermion system is not simply the usual isotropic (or *s*-state) kind, but anisotropic kind (*p*- or *d*-state). But today there are still some unanswered questions about heavy fermion superconductivity such as: "What is the pairing mechanism involving magnetic interactions, and what is the topology of the superconducting gap on the Fermi surface?" While the origin of superconductivity in heavy fermion materials is unknown, there is growing evidence that heavy fermion superconductivity originates from magnetic fluctuations [39] which are thought to arise primarily from Kondo coupling of partially filled 4*f* and 5*f* shells to conduction electrons.

Another interesting feature of heavy fermion superconductivity is that superconductivity appears in some cases under external pressure. Examples include: $CeCu_2Ge_2$ [72], $CePd_2Si_2$ [73, 39], $CeRh_2Si_2$ [38], $CeIn_3$ [39], and CeRhIn5 [40]. Unlike $CeCu_2Si_2$ which is the superconducting at ambient pressure with Tc= 0.65 K [45], for these materials the superconductivity emerges near the quantum citical point (QCP) where the magnetic ordering is suppressed by the large external pressure. In

Reproduced with permission of the copyright owner. Further reproduction prohibited without permission.

other words, when pressure p is applied to these cerium compounds, the magnetic ordering temperature T_N shifts to lower temperature i.e., T_N shifts toward the QCP, corresponding to $T_N \rightarrow 0$, and at $p = p_c$ (where p_c is the critical pressure) superconductivity appears.

In conclusion, heavy fermion compounds display a number of anomalous properties that can not be explained with well known conventional theories. As can be seen from this brief survey in spite of progress, these systems present many challenging problems for theoretical investigation. The complexity and variety of their behavior must be consequences of the strong short range Coulomb interaction between the *f* electrons, including strong local correlations. The survey given here for heavy fermion materials is too brief to convey the diversity of their behavior. For more details, the reader can review Ref. [30, 46, 74-76].

2.4 $CeMIn_5$ Family

$CeMIn_5$ (M = Rh, Co, Ir) are recently discovered heavy fermion materials. These materials are also known as "^{115}In". This nickname comes from the ratio of included materials of $CeMIn_5$, with 5 parts of Indium to one each of various elements. These materials crystallize in the tetragonal $HoCoGa_5$ crystallographic structure. In this structure, as shown in Figure 2.5, $CeMIn_5$ consists of alternating layers of $CeIn_3$ (a heavy fermion antiferromagnet in which superconductivity can be induced with applied pressure [39]) and MIn_2 stacked sequentially along the [001] axis. Therefore, we can treat $CeIn_3$ as a parent compound for the $CeMIn_5$ family. As seen in Fig. 2.5, there are two inequivalent crystallographic sites of In in these compounds, the In (1) site, analogous to the In site in cubic $CeIn_3$, is located on the top and bottom faces of the

Reproduced with permission of the copyright owner. Further reproduction prohibited without permission.

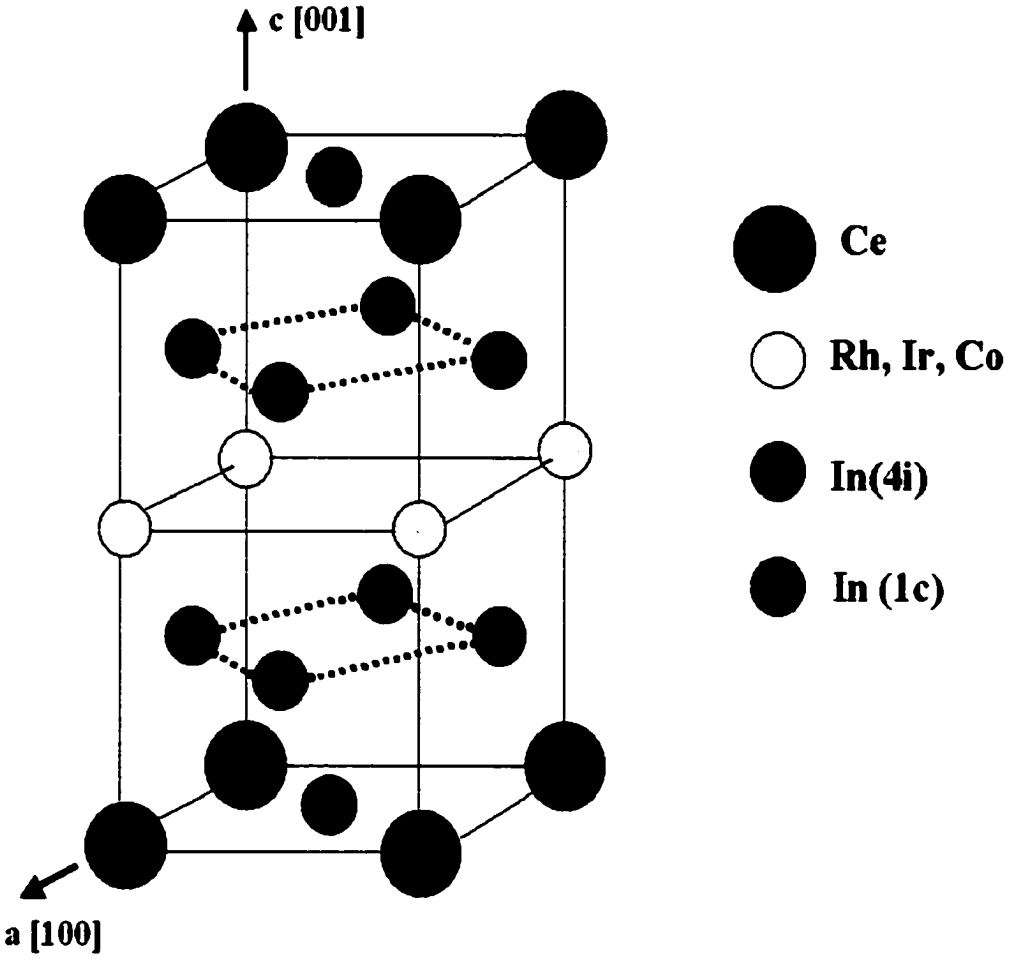

Figure 2.5: Crystal structure of $CeMIn_5$ (M=Rh, Ir, Co) family.

Reproduced with permission of the copyright owner. Further reproduction prohibited without permission.

tetragonal unit cell. And there are four In (2) sites per unit cell, two on each of lateral faces of the unit cell, equidistant above and below the Rh layer. As might be expected from the quasi- two dimensional (2D) structure, the magnetic susceptibility and electric resistivity of these materials are anisotropic. Because these materials exhibit 2D layers of $CeIn_3$, it has been suggested that this family would enable new understanding of relationship between magnetism and superconductivity in heavy fermion materials. In the following paragraphs we will give physical properties measured so far for each member of this family.

2.4.1 $CeIrIn_5$

$CeIrIn_5$ is the heavy fermion compound with γ = 720 mJ/mol-K^2 [56] and shows unconventional superconductivity at 0.4 K [77]. $CeIrIn_5$ is the first ambient pressure heavy fermion superconductor discovered since 1991 when UPd_2Al_2 was discovered. For $CeIrIn_5$, and the other family members the atomic positions and the lattice constants are given in Table 2.2. The temperature dependence of the electrical resistivity of $CeIrIn_5$ is typical of heavy fermion materials, thus, weakly temperature dependent above a characteristic temperature (here ~30K) and followed by rapid decrease at lower temperature. At room temperature, the resistivity was measured as 89 $\mu\Omega$–cm with the current along [100] direction [79]. Susceptibility measurements showed that there is a large anisotropy between [001] and [110] directions. Above 100 K, the susceptibility follows the Curie-Weiss law with the effective moment μ_{eff} = 2.50 μ_B/Ce for the [001] direction and μ_{eff} = 2.36 μ_B/Ce for the [110] direction [80]. R. Movshovic *et al* [54] have shown a power law temperature dependence by using the

Reproduced with permission of the copyright owner. Further reproduction prohibited without permission.

Table 2.2 Atomic positions and lattice parameters of $CeMIn_5$ family. Data was taken from Ref. [82, 55, 78].

lattice constant (Å)	$CeRhIn_5$	$CeCoIn_5$	$CeIrIn_5$
a = b	4.65	4.62	4.674
c	7.54	7.56	7.501

Atomic positions for $CeRhIn_5$

	x	y	z
Ce	0	0	0
Rh	0	0	½
In1	½	½	0
In2	0	½	0.306

Atomic positions for $CeCoIn_5$

	x	y	z
Ce	0	0	0
Rh	0	0	½
In1	½	½	0
In2	0	½	

Atomic positions for $CeIrIn_5$

	x	y	z
Ce	0	0	0
Rh	0	0	½
In1	½	½	0
In2	0	½	0.305

results of measurements of low temperature specific heat and thermal conductivity measurements, and reported that superconductivity in $CeCoIn_5$ and $CeIrIn_5$ compounds display unconventional superconductivity in which there are lines of nodes in the superconducting gap. The first de Haas-van Alphen (dHvA) measurement of $CeIrIn_5$ is made by Haga and *et al.* [79]. They measured dHvA frequencies and cyclotron effective masses by using a field modulation technique at 25 mK, with the field along

Reproduced with permission of the copyright owner. Further reproduction prohibited without permission.

Table 2.3: dHvA frequencies and corresponding cyclotron effective masses of $CeIrIn_5$ [79].

	Experiment		Band Theory	
H || [001]	F (kT)	$m^*(m_0)$	F(kT)	$m^*(m_0)$
β_1	12.00	32	12.40	3.32
β_2	6.59	21	6.18	1.33
	6.11	30	6.18	1.37
α_1	5.56	25	5.00	1.89
	5.15	17		
	5.07	23		
α_2	4.53	29	4.03	1.15
α_3	4.24	10	3.65	1.37
γ	0.27	6.3		
H || 49.5° from [001] to [100]				
δ_1	1.96	45	2.29	2.17
δ_2	1.63	35	2.08	3.14

[001] direction. The measured effective masses are given in Table 2.5 and Fast Fourier Transform (FFT) of dHvA data is shown in Fig.2.6. In addition to that, they also measured the angular dependence of dHvA ferquencies as shown in Fig. 2.7. Furthermore, they reported that some of the branches roughly follow a $1/\cos\theta$ dependence which indicates the existence of cylindrical Fermi surfaces. Based on the band theory, they have also reported that 4*f* electrons in $CeIrIn_5$ are itinerant and they observed that itinerant 4f electron picture is agreement with the experiment.

2.4.2 $CeCoIn_5$

Similar to $CeIrIn_5$, $CeCoIn_5$ shows unconventional superconductivity with T_c= 2.3 K. at atmospheric pressure [77]. The T_c measured in $CeCoIn_5$ is the highest transition temperature observed in the class of the heavy fermion materials so far. The specific heat coefficient for $CeCoIn_5$ was measured to be $\gamma = 290$ mJ/mol-K^2. Below 1.4

Reproduced with permission of the copyright owner. Further reproduction prohibited without permission.

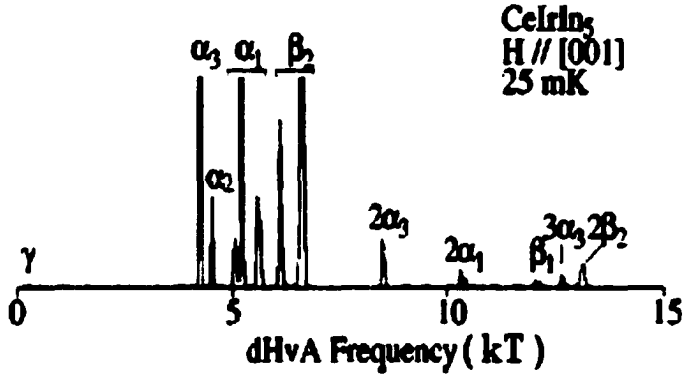

Figure 2.6 FFT of dHvA frequencies with the applied field along the [001] direction This plot was reproduced from Ref.[79].

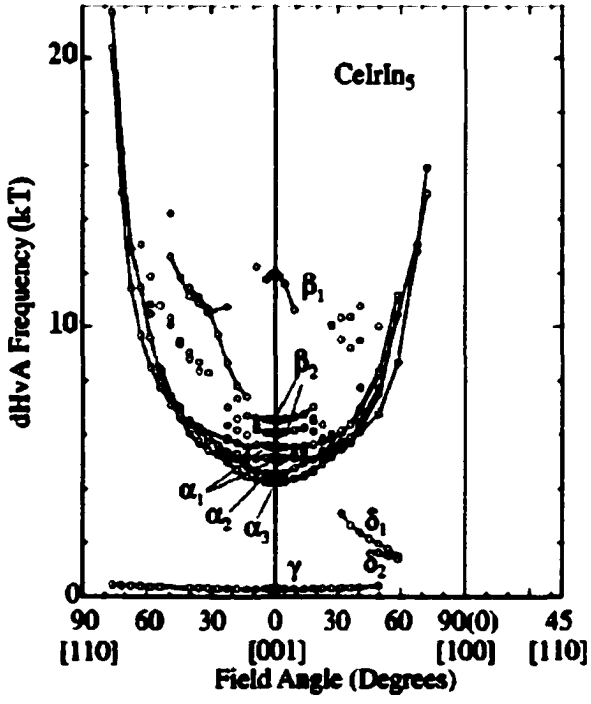

Figure 2.7 Angular dependence of dHvA frequencies for $CeIrIn_5$ (This figure was reproduced from Ref. [79]).

Reproduced with permission of the copyright owner. Further reproduction prohibited without permission.

K the transition from the normal state to the superconducting state as a function of magnetic field in $CeCoIn_5$ has been observed to be first order at ambient pressure [81]. We measured dHvA frequencies of $CeCoIn_5$. The details of the measurements of this material will be given in Chapter 5.

2.4.3 $CeRhIn_5$

$CeRhIn_5$ has the same tetragonal crystal structure as the $CeMIn_5$ family. It is an antiferromagnet at ambient pressure with T_N= 3.8 K and becomes a superconductor (first order superconducting transition) with applied pressure of the order of 16 kbar at T_c=2.1 K [40]. This transition temperature is nearly 10 times larger than the value found in cubic $CeIn_3$ which is 0.25 K at about 25 kbar [52]. As indicated in the above sections, $CeRhIn_5$ differs somewhat from other Ce based heavy fermion materials, because it appears to be a quasi 2D variant of $CeIn_3$.

The first limited dHvA studies on $CeRhIn_5$ were reported by Cornelius *et al.*[67] using pulsed fields. They measured the Fermi surface in two different field directions due to the anisotropic Fermi surface of this compound. The original measured dHvA frequencies and effective masses by Cornelius *et al.* [67] are given in Table 2.4. But these frequencies are corrected by 4.5% due to an error in their data analysis [68]. After that, we reported a more comprehensive dHvA study throughout the entire Brillouin zone of $CeRhIn_5$ [77]. The de Haas van Alphen measurements of $CeRhIn_5$ and $LaRhIn_5$ will be presented in Chapter 4 in detail.

2.4.4 $LaMIn_5$

On the other hand, $LaMIn_5$ compounds are simple metals crystallized with the same tetragonal structure as $CeMIn_5$. Unlike $CeMIn_5$, they do not have *f* electrons and nor do they have any magnetic or superconducting transitions. They are typical metals

Reproduced with permission of the copyright owner. Further reproduction prohibited without permission.

Table 2.4 Measured dHvA effect frequencies and effective masses for B ‖ [100] and B ‖ [001] in $CeRhIn_5$ reported in Ref [67]. Frequencies in parenthesis are corrected by 4.5% [68].

B ‖ [100]		B ‖ [001]	
F(T)	$m^*(m_e)$	F(T)	$m^*(m_e)$
100 (105)	1.36±0.23	3450 (3605)	0.75±0.05
210 (219)	0.99±0.10	4484 (4686)	1.26±0.05
282 (295)	0.93±0.15	5987 (6256)	2.41±0.16
471 (492)	0.72±0.14		
683 (714)	1.17±0.09		
824 (861)	1.31±0.22		

Table 2.5 Atomic positions and lattice parameters of $LaMIn_5$ family. Data was taken from Robin Macaluso, a graduate student in Department of Chemistry, Louisiana State University.

lattice constant (Å)	$LaRhIn_5$	$LaCoIn_5$	$LaIrIn_5$
a = b	4.6768	4.6399	4.6897
c	7.5988	7.6151	7.5788

Atomic positions for $LaRhIn_5$

	x	y	z
Ce	0	0	0
Rh	0	0	½
In1	½	½	0
In2	0	½	0.30775

Atomic positions for $LaCoIn_5$

	x	y	z
Ce	0	0	0
Rh	0	0	½
In1	½	½	0
In2	0	½	0.31134

Atomic positions for $LaIrIn_5$

	x	y	z
Ce	0	0	0
Rh	0	0	½
In1	½	½	0
In2	0	½	0.30766

Reproduced with permission of the copyright owner. Further reproduction prohibited without permission.

with a Sommerfeld specific heat coefficient, γ, of about 5mJ/mole-K^2 [56]. The crystal structural information of these light metals are given in Table 2.5. A more comprehensive dHvA study of $LaMIn_5$ is discussed in Ref. [83 and 84]. In this study, $LaMIn_5$ were used as a host metal to investigate the formation heavy fermion material of $CeMIn_5$.

Reproduced with permission of the copyright owner. Further reproduction prohibited without permission.

CHAPTER 3

THE DE HAAS VAN ALPHEN EFFECT

3.1 Historical Background

The Landau Quantum oscillatory magnetization or the de Haas van Alphen effect (dHvA) was predicted by Landau [85] in 1930 when he was working on the diamagnetism of free electrons. Within a month or two of Landau's paper, the effect was first observed experimentally by de Haas and van Alphen [86]. In this first experiment, they measured the susceptibility of bismuth in single crystal form with an applied magnetic field up to about 2 Tesla at 14.2 K and found that the susceptibility, χ, was not constant, as is usual for weak magnetic materials, but varied in an oscillatory manner with the field. They have also reported that the amplitude of oscillations diminishes as the temperature is raised and the effect disappears completely above about 30 or 40 K for their maximum fields.

The theoretical explanation of the oscillations was given by Peierls [87] in 1933. This theory is based on Landau's formulation of the energy levels in magnetic field. Although Peierls' calculations qualitatively resembled the experimental data, the calculated magnetization was nearly 70 times smaller than the experimentally observed magnetization. Later, it was understood that the reason for this discrepancy was originating from lack of anisotropy terms in Peierls' calculations. In 1938, Blackman [88] developed Peierls' theory by taking into account the anisotropy. But this theory was still so simplified and was not enough in many cases. In 1939, the detail experimental results on bismuth were published by Shoenberg [89]. Until 1947, despite of Peierls' comment that the dHvA effect should be observed in all metals, most experimentalists

Reproduced with permission of the copyright owner. Further reproduction prohibited without permission.

believed that it was only in bismuth that the effect could be observed in practice. But this wrong belief was broken with Marcus' experimental discovery of the dHvA effect in zinc in 1947 [90]. After that it became evident that the effect could be observed in nearly every polyvalent metal for which good single crystals were available. It is not so surprising that no effect could be seen in any monovalent metals, because theoretical calculations suggested that considerably higher fields would be necessary to observe dHvA oscillations. The significant great theoretical advance was made in 1952 by Onsager [91], who showed that the frequency of the oscillations is directly proportional to the extremal cross-sectional area of the Fermi surface normal to the applied magnetic field. This was a great contribution because measurements of the same effect in different crystallographic directions yielded information on the shape of Fermi surface for metals. In the same years, Dingle [92] also pointed out that electron scattering was broadening Landau levels and this leads to an amplitude reduction of in the dHvA oscillation. Other important theoretical contribution came from Lifshitz and Kosevics [93] in 1954 and 1955. They developed a detailed theory accounting for not only the frequency of oscillations but also their amplitudes and phases. In those years, discovery of a pulsed field method to reach the higher fields (typically 10T) and developments in making single crystals allowed the investigation of the Fermi surface of many metals. In 1960, at a conference (Cooperstown), a surprising mystery was reported which was observed by Priestley [94] that one of the frequencies in magnesium was much higher than expected. The fact that the corresponding orbit area was larger than the hexagonal cross-section of Brillouin zones seemed impossible. The solution of this mystery was soon given as *magnetic breakdown* by Cohen and Falicov [95] in 1961 and detailed work was done by Blount [96] in 1962. Magnetic breakdown is a kind of quantum tunneling between

Reproduced with permission of the copyright owner. Further reproduction prohibited without permission.

states in different zones of equal energy but separated by a small potential barrier. That is, at sufficiently strong magnetic fields the electron could switch tracks from one orbit to another, so that it has a new and sometimes much larger orbit. Another surprising phenomena associated with the dHvA effect was observed at high fields in the noble metals, where an anomalous high harmonic content in the oscillations was observed by Shoenberg [97] in 1962. This effect was interpreted as a *magnetic interaction* (or Shoenberg effect) due to the fact that the field seen by electrons was the magnetic induction, **B**, rather than the applied field, **H**. In general this effect can be ignored, but at high fields and very low temperatures, the amplitude of the oscillation may become large enough for the difference between **B** and **H**. Thus, the contribution of $4\pi\mathbf{M}$ provides a kind of feedback effect to the amplitude. The result of this effect can be seen as frequency mixing and modification of harmonic amplitudes. With the advent of superconducting magnets in 1960s, measuring the oscillations in metals became much more precise due to the steady field. Todays very advanced experimental techniques and improvements in sample preparation allow to us carry out very detailed dHvA studies in more complicated metallic compounds. Combining the dHvA measurements with band structure calculations, we are able to obtain the correct topology of the Fermi surface. In the following sections, first we will talk about the behavior of electrons in a magnetic field and give a detailed explanation of the dHvA effect.

3.2 Quantization of Electron Orbits in a Magnetic Field

When a metal is placed in a magnetic field, **B**, the electrons of this metal are under the influence of the Lorentz force

$$\mathbf{F} = \hbar\dot{\mathbf{k}} = -\frac{e}{c}(\mathbf{v} \times \mathbf{B}), \tag{3.1}$$

Reproduced with permission of the copyright owner. Further reproduction prohibited without permission.

where **v** is the velocity of the electron, e is the magnitude of the electron charge, and c is the speed of light. If, as usually is the case, there is a non zero component of the velocity in the direction of the field, then the electron path will be a helix whose axis lies parallel to **B**. When an electron is in a such a helical orbit, the effect of the magnetic field only alters the direction of **v** and not its magnitude, so the energy of the electron is unchanged, and the electron remains on a constant energy surface.

Prior to the application of the magnetic field **B** , electron states are uniformly distributed in **k**-space (momentum space). In the k_x-k_y plane, they are represented by an infinite square net of points that some of them are shown in Figure 3.1(a). But in the presence of the magnetic field, let's say **B** pointing along the z-direction, electron states are redistributed so that they lie on the rings as shown in Fig.3.1(b). Thus, electrons rotate in a circular path with the cyclotron frequency $w = eB/mc$ (for the free electron case) which is independent of the radius of the orbit. That is, the orbits of electron are quantized. Equation 3.1 states that, in **k**-space, the rate of change of **k** is a vector that is normal to **B**. Therefore, in **k**-space the electron wave vector also moves in an orbit that is in a plane normal to **B**. By integrating equation 3.1, we find

$$\mathbf{k} = -\frac{e}{\hbar c}(\mathbf{r}\times\mathbf{B}), \tag{3.2}$$

This means that the orbits in real space and reciprocal space are geometrically similar but the orbit in **k**-space is rotated through $\pi/2$ with respect to the real space orbit and its radius is $eB/\hbar c$ times the radius of the real space orbits.

As can be seen in the above discussion, the magnetic field has no effect on the electron motion in the k_z-direction; however, in the k_x-k_y plane the electron motion is no longer free electron-like, but it is circular about B_z. Thus, in the k_x-k_y plane an

Reproduced with permission of the copyright owner. Further reproduction prohibited without permission.

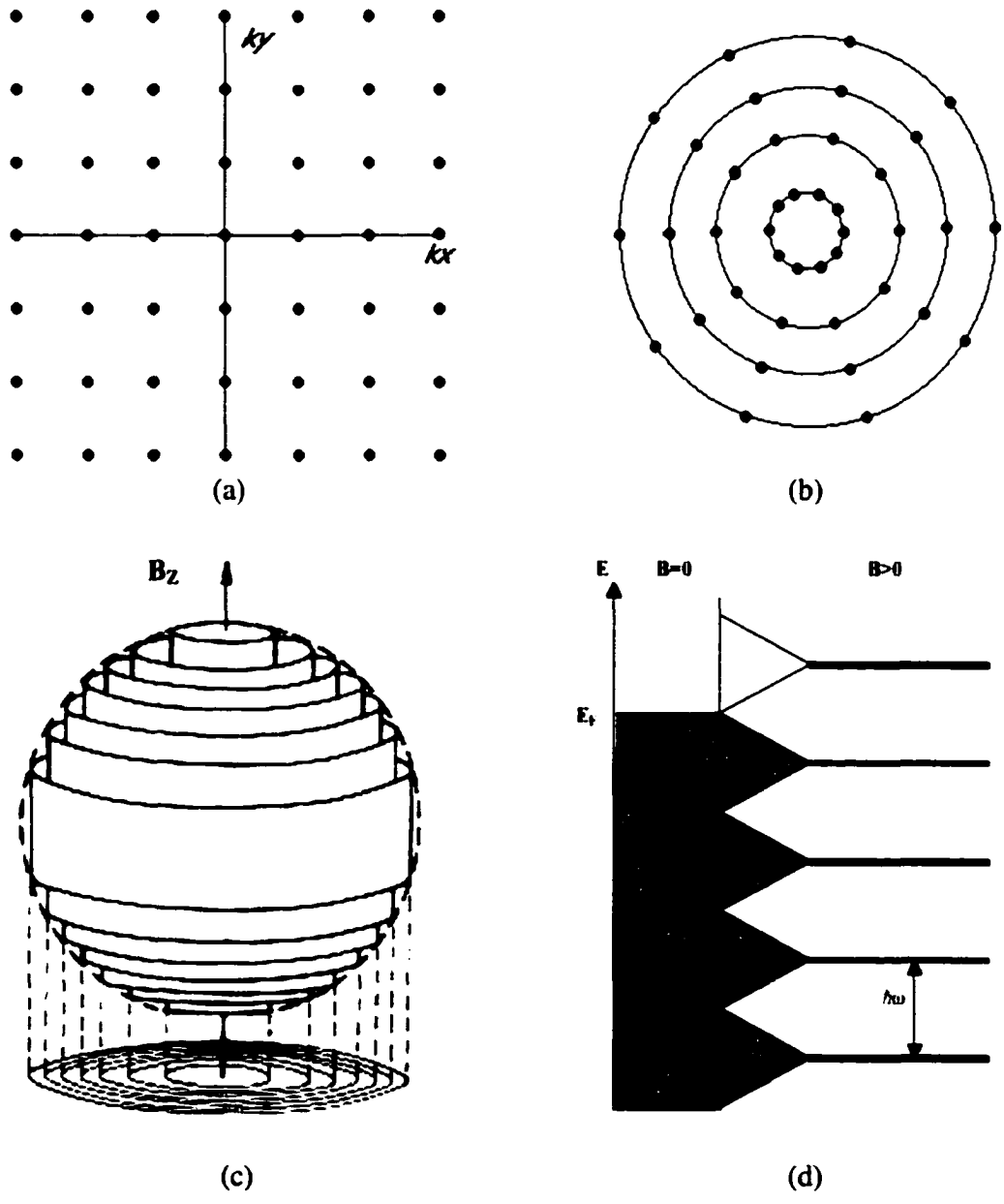

Figure 3.1 (a) Allowed electron orbits in two dimensional k-space in the absence of a magnetic field (b) quantization of electron orbits in two dimensional k-space in the presence of a strong magnetic field. (c) quantization of electron orbits in three dimensional k-space in a strong magnetic field. Allowed energy states lie on the concentric cylinder called Landau levels and the occupied portion of these levels is cut by the Fermi surface. With increasing magnetic field, Landau cylinders expand and they become empty when they pass out of the Fermi surface. (d) A schematic diagram of energy states, filled up to the Fermi energy E_F, split into Landau levels in the presence of magnetic field **B**. Here, the spin of the electron is neglected for clarity. These figures are reproduced from Ref. [10] and [27].

Reproduced with permission of the copyright owner. Further reproduction prohibited without permission.

electron behaves like a two dimensional harmonic oscillator, and we can easily write the quantum mechanical simple harmonic oscillator energy levels as

$$\varepsilon_n = (n + \frac{1}{2})\hbar w_c + \frac{\hbar^2}{2m} k_z^2 \tag{3.3}$$

where n = 0,1,2,..... is a quantum number describing the degree of excitation, and m is the mass of the free electron. This energy expression shows that nothing has changed for motion along the magnetic field direction, the plane wave solution with k_z is still appropriate. However, electron motion in the x-y plane is simple harmonic-like giving quantized simple harmonic energy levels, which are called *Landau levels*. These Landau levels have a concentric circular form in the k_x-k_y plane (Figure 3.1(b)) and they are cylindrical surfaces in the 3-dimentional **k**-space as shown in Figure 3.1(c). Thus in k-space the representative points lie on the Landau cylinders.

The quantization of the electron orbits, first studied by Onsager [91] and Lifshitz [93] independently, is based on the Bohr-Sommerfeld quantization rule. This rule for quantized orbits in a magnetic field can be written as

$$\oint \mathbf{p}.d\mathbf{r} = (n + \gamma)2\pi\hbar , \tag{3.4}$$

where n is an integer and γ is a phase correction which is ½ for free electrons and **p** is the momentum of the free electron in a magnetic field which is given as the sum of two parts; the kinetic momentum and field momentum

$$\mathbf{p} = \mathbf{P}_{kin} + \mathbf{P}_{field} = \hbar k - \frac{q}{c}\mathbf{A} , \tag{3.5}$$

where **A** is a vector potential which is related to magnetic field by $\mathbf{B} = \nabla \times \mathbf{A}$. By using the above equations, an expression can be obtained for the area of the orbit in **k**-space

Reproduced with permission of the copyright owner. Further reproduction prohibited without permission.

such as

$$a_n(\varepsilon) = \frac{2\pi eB}{c\hbar}(n+\gamma). \qquad (3.6)$$

Here a_n is the area of cross-section of a Landau tube cut by a plane normal to **B**. Thus in a magnetic field the area of the orbit in **k**-space is quantized. The equation 3.6 also states that the orbits in **k**-space are spaced so that the area between two successive orbits, n and n+1, differ by $(2\pi Be)/\hbar c$.

As discussed above, when **B** is applied along the z-axis, the permitted values of k_x and k_y is such that **k** lies on the surface of a set of concentric cylinders (Landau levels) whose axis is along the z-direction. These permitted levels are highly degenerate because the permitted levels must be able to accommodate all electrons which in zero field would have occupied these states between levels. Therefore, the states are distributed in a manner similar to that shown in Figure 3.1(d). Some electrons will have their energy raised and others lowered, so that on average the effect of the quantization does not affect the total energy very much.

If **B** is increased, the cylinders in Figure 3.1(c) expand so that the permitted levels move to higher energies and their spacing becomes larger. By the rearrangement of energies as **B** increases, some of the electrons which were originally in their lowest state are forced to enter slightly higher energy states, and some of them which were originally in the highest state are forced to enter lower energy states. However, the situation is very different at the highest filled Landau level. As this level expands its extension in the k_z direction (i.e the height of the cylinder) diminishes very rapidly hence the number of electrons on this level decreases and this tends to zero when the level becomes coincident with the position of the Fermi surface. Thus as the highest

Reproduced with permission of the copyright owner. Further reproduction prohibited without permission.

level starts to expand, the energy of the electrons in this level first rise , but then as the level approaches the Fermi surface, the electrons in the highest level go into the one below, so that on balance the total energy of the system decreases. When the highest level passes the Fermi surface, it becomes completely empty and all of its electrons are in the lower level. As the field increases further, this lower level starts to have its energy raised, so that the energy of the system again starts to increase and the situation repeats. Thus the energy U of the electron assembly shows periodic variations as the field increases and there is a discontinuity in the relationship between U and B each time the outermost energy level crosses the Fermi energy. Since at the absolute zero of the temperature the magnetic moment m is given by

$$m = -\frac{\partial U}{\partial B}. \tag{3.7}$$

As seen in equation (3.7) m, and hence the susceptibility χ also show a periodic variation. If B_1 and B_2 ($B_2 > B_1$) are the fields at two consecutive discontinuities in U, since A_F, the extremal (maximum or minimum) cross sectional area of the Fermi surface, is the same in both occasions, then from equation 3.6, we can write

$$\frac{1}{B_1} - \frac{1}{B_2} = \frac{2\pi e}{\hbar c}\left(\frac{1}{A_F}\right) \tag{3.8}$$

or

$$\Delta\left(\frac{1}{B}\right) = \frac{2\pi e}{\hbar c}\left(\frac{1}{A_F}\right). \tag{3.9}$$

These are the key equations of the dHvA effect, thus these equations show that m is periodic in 1/B and measurement of the period $\Delta(1/B)$ enables us to calculate the cross sectional area of the Fermi surface, A_F. When, in general, the Fermi surface is not

Reproduced with permission of the copyright owner. Further reproduction prohibited without permission.

spherically symmetric, it is possible to obtain several sets of oscillations (several periods) which correspond to different extremal orbits. (For that reason, to get the desired frequency of each period, Fourier Analysis is done on a dHvA data set that is periodic in 1/B.) When the Landau tubes expand and cross the Fermi surface as the magnetic field is increased, the density of states at the Fermi energy also oscillates periodically. As already mentioned in Chapter 1, it is the density of states at the Fermi energy level which influences all electronic, thermodynamic and transport properties of the material, because only the electrons close to the Fermi level can be excited by small amounts of energy. Therefore, we expect that all these properties oscillate if **B** is changed. For instance, the periodic change in magnetoresistance as a function of inverse magnetic field was observed experimentally in some materials and this phenomena was called as Shubnikov-de Haas (SdH) effect. The above discussion is rather qualitative and hand waving for the case of magnetic susceptibility. In the following section, we will discuss the qualitative treatment of dHvA effect.

3.3 Lifshitz-Kosevich (LK) Equation

So far we have considered only the behavior at absolute zero. At temperatures above absolute zero, the permitted energy levels are broadened by an amount of the order of kT, and this has the effect of reducing the amplitude oscillations, though the period is unaffected. At finite temperature, the energy of a system is not given simply by U, but the free energy, F. The free energy of a system of N particles is given by F= U-TS, where U is the internal energy and S is the entropy of the system. By using a nearly free electron approximation, Lifshitz and Kosevich [93, 98] developed a detailed theory of oscillatory magnetization. The detailed discussion of theory of dHvA

Reproduced with permission of the copyright owner. Further reproduction prohibited without permission.

oscillations is given by Gold and Shoenberg [99, 100]. But the principal equations for the oscillatory magnetization are given as

$$\tilde{M}_{//} = -(\frac{e}{c\hbar})^{3/2} \frac{2FkTV}{(2\pi\beta A_F'')^{1/2}} \sum_{p=1}^{\infty} \frac{\exp(-2\pi^2 pkx/\beta B)\cos[\frac{1}{2} p\pi g(m^*)]}{p^{1/2}\sinh(2\pi^2 pkT/\beta B)} \sin(2\pi p(\frac{F}{B} - \gamma) \pm \frac{\pi}{4}) \quad (3.10)$$

or in terms of reduction factors,

$$\tilde{M}_{//} = -(\frac{e^5}{2\pi^5\hbar})^{1/2} \frac{B^{1/2}F}{m^*|A_F''|} \sum_{p=1}^{\infty} p^{-3/2} R_T(p) R_s(p) R_D(p) \sin(2\pi p(\frac{F}{B} - \gamma) \pm \frac{\pi}{4}) \quad (3.11)$$

and

$$\tilde{M}_{\perp} = -\frac{1}{F}\frac{\partial F}{\partial \theta}\tilde{M}_{//}. \quad (3.12)$$

These equations are known as the LK equations. By taking the Fourier transform of these equations, a fundamental frequency F and and its harmonics, nF (n=2,3,...) are obtained. In the above equations, $\tilde{M}_{//}$ and $\tilde{M}_{\perp}$ are the components of oscillatory magnetization in directions parallel and perpendicular to external magnetic field and F is the dHvA frequency ($F = c\hbar A_F/2\pi e$) corresponding to an extremal cross sectional area of the Fermi surface A_F, and p is an integer or the harmonic index, m* is renormalized quasiparticle mass for extremal cross sectional area of the Fermi surface, and γ is a phase constant. A_F'' is called the curvature factor which measures the curvature of the Fermi surface at the extremal orbit. The sign in front of the $\pi/4$ is positive when the extremal area is minimum and negative when it is a maximum. The terms $R_T(p)$, $R_S(p)$ and $R_D(p)$ in the above LK equations are temperature reduction, spin reduction, and Dingle reduction factors, respectively. These reduction factors, described

Reproduced with permission of the copyright owner. Further reproduction prohibited without permission.

in the following section, govern the amplitude of the dHvA oscillations as a function of temperature, applied field, and interference from opposite spin states.

3.4 Reduction Factors in LK Equation

The reduction factors included in LK equation can be derived by an idea that the Fermi surface is not sharp, but instead the Fermi level is split into two sheets by spin effects and broadened by sample inhomogeneities and finite temperature. That means the dHvA frequencies are not sharply defined either. These effects are equivalent to phase smearing and reduce the dHvA amplitude. First, the finite temperature damps the dHvA oscillation by a factor,

$$R_T(p) = \frac{\pi\lambda}{\sinh \pi\lambda} = \frac{2\pi^2 pk\mathrm{T}/\beta H}{\sinh(2\pi^2 pk\mathrm{T}/\beta H)}\ , \tag{3.13}$$

where $\beta = e\hbar/m^*c$. In the dHvA data, the temperature dependence of the amplitude of the oscillatory component gives the effective masses for the carriers.

Second, $R_D(p)$ is the Dingle reduction factor due to the finite scattering time of the electrons, and it is given as

$$R_D(p) = \exp\left(\frac{-2\pi^2 pkT_D}{\beta H}\right)\ , \tag{3.14}$$

where $T_D = \hbar/2\pi\tau k$ is known as the Dingle temperature [92] (τ is a finite relaxation time). From the field dependence of amplitude, one can obtain T_D and hence τ.

Finally, $R_S(p)$ is the spin reduction factor. In a magnetic field **B**, the spin degeneracy of the electronic energy levels is lifted and each energy level splits into a spin up and spin down. The superposition of the spin up and spin down oscillations have a contribution to the dHvA amplitude as

Reproduced with permission of the copyright owner. Further reproduction prohibited without permission.

$$R_S(p) = \cos(\frac{\pi}{2} pg \frac{m^*}{m}), \tag{3.15}$$

where g is the spin-splitting factor and p is the harmonic number.

Other types of reduction factors such as sample and magnetic inhomogeneity can often damp the amplitude of oscillations. For example , if the field distribution is inhomogeneous across the sample, the additional reduction factor is given by

$$R_{\Delta H} = \frac{\sin(\pi p F \Delta H / H^2)}{(\pi p F \Delta H / H^2)}, \tag{3.16}$$

where ΔH is the inhomogeneity in the field along the sample. If the sample has inhomogeneous compositions, thus, if there are some defects in the sample then the amplitude of oscillations is reduced by the factor

$$R_{\Delta F} = \exp(\frac{-2\pi^2 pkx'}{\beta H}), \tag{3.17}$$

where $x' = \beta(\Delta F)/\pi k$ and ΔF is the spread in frequency over the sample. As can be seen by the above damping factors, dHvA oscillations require the very lowest possible temperature and the highest possible magnetic fields with samples of maximum purity.

3.5 dHvA Effect in the Heavy Fermion Systems

The observation of dHvA effect has played a unique role in the development of the physics of metals. It is very capable of yielding precise and detailed information on the Fermi surface. The observation of magnetic oscillations not only gives access to the shape of Fermi surface, but also to the quasiparticle cyclotron effective masses, Fermi velocities, scattering rates and g-factors. As already mentioned in Chapter 2, the heavy fermion systems exhibit quite unusual behavior compared to normal metals. These interesting and anomalous properties of the heavy fermion systems originate from the

Reproduced with permission of the copyright owner. Further reproduction prohibited without permission.

highly correlated *f* electrons whose nature displays either localized or itinerant behavior or both. In this regard, the dHvA effect is undoubtedly a unique probe to study heavy fermion systems due to its capability of yielding precise information about the Fermi surface, the cyclotron effective mass, and the scattering life time of the conduction electrons. In heavy fermion systems, the LK equation describes dHvA oscillations quite well, like conventional materials, except for highly enhanced quasiparticle masses, ranging up to more than a hundred times the expected band masses [101]. Because of the strong correlation energy in heavy fermion materials, ordinary perturbation theories or conventional band structure calculations are not likely to provide a successful description of heavy electron phenomena. In general it is thought that the mass enhancement arises from many body interactions, in particular through hybridization between conduction electrons and localized but highly correlated 4*f* and 5*f* electrons on the rare earth sites of the heavy fermion alloys.

There have been several attempts to derive a theory of the dHvA effect appropriate to heavy fermion systems. Among these, Luttinger [102] and Bychkov and Gorkov [103] showed that the functional form of the LK equation is left unchanged by the electron-electron interaction, but certain parameters in the LK equation such as the effective mass and the g-factor, need to be modified as a consequence of the many body interaction. In addition, Fowler and Prange [104] and Engelsberg and Simpson [105] worked on the influence of electron–phonon interaction on the dHvA effect. They showed that the effective mass in the LK equation needs to be enhanced by a factor of $(1+\lambda)$, where λ is a parameter which is characteristic of the electron-phonon interaction strength. Wasserman and Springford [106] obtained a general theory of dHvA effect in an

Reproduced with permission of the copyright owner. Further reproduction prohibited without permission.

interacting system which preserves the structure of the original non-interacting LK theory and they applied their extended LK theory, including electron-electron and electron-phonon interaction, to analyse several problems such as heavy fermions and type II superconductors.

Experimentally, the dHvA effect has been observed in a variety of heavy fermions [46,74], including UPt_3, $CeCu_6$, $CeCu_2Si_2$, and CeB_6. Common features in these experiments are the observation of heavy quasiparticles with mass comparable to those deduced from C_p and χ, and sharply defined Fermi surfaces that in many cases agree well with those predicted by band theory, despite the strong electron-electron interaction.

3.6 Experimental Techniques

3.6.1 Introduction

The $Ce_xLa_{1-x}MIn_5$ single crystals were prepared with the Indium (In) flux method by J. L. Sarrao and P.G. Pagliuso at the Los Alamos National Laboratory. Single crystals of these compounds were grown by combining stoichiometric amounts of high purity Ce, Co, La, Rh, Ir and In. First, the desired stoichiometric amounts of these reactants were placed in an alumina crucible and then this crucible itself was placed in a sealed evacuated quartz ampoule. Then this ampoule was heated over several hours to 1100 °C, where the molten elements homogenized, and kept at that temperature for 2 hours and then it was slowly cooled down to 700 °C. At this point, the ampoule was placed in a cup of a centrifuge and quickly spun. Therefore, the crystals and In flux (still liquid) were separated. Most of the samples were obtained as a columnar shape with their long axis along the tetragonal *c*-axis [78]. In order to separate a single crystal from the columnar shape remove residual flux from the sample we used either a solution of 25% HCl acid in H_2O or a razor blade.

Reproduced with permission of the copyright owner. Further reproduction prohibited without permission.

The dHvA effect is essentially a low temperature phenomenon, in most cases liquid helium temperature or lower temperatures are required to observe the oscillations. For a large Fermi surface, oscillations are also a high field phenomenon, in most cases to see oscillations, the applied field should be larger than 1.5 T [107]. In general, the signal amplitudes of the typical dHvA signal detection equipment are of the order of 10^{-5} volts. Of course, producing high purity strain-free single crystals and having the right crystal orientations are the major issues to study in the dHvA effect. Because of several limiting factors, the sample size should not be bigger than a few mm. As an example, the sample must be confined to a sufficiently homogenous region of the magnet. Secondly, the signal-noise ratio should be very small. In a dHvA oscillation, there is a general tendency for noise levels to increase with increasing sample size. The other restriction, for example, is that in the pulse field method, large samples are prone to induced eddy currents and these currents increase the sample temperature. In the following sections, we will discuss the experimental methods used to observe dHvA oscillations in this work. These methods are largely complementary and they have either some advantages or some disadvantages compared to each other.

3.6.2 The Torque Method

Some of the measurements mentioned throughout this dissertation were made by using a capacitive torque cantilever at a temperature between 4 and 1.3 K at the National High Magnetic Field Laboratory (NHMFL), Tallahasse, FL. The earliest use of a capacitive torque cantilever was reported by Brooks *et al.* [108]. Ever since, this technique has become a standard technique for measuring dHvA oscillations in high

Reproduced with permission of the copyright owner. Further reproduction prohibited without permission.

field. The capacitive torque cantilever used in this work consists of a thin metal "T" shape Be-Cu foil and a parallel fixed metal coated Si base plate. The schematic of this cantilever is shown in Figure 3.2. The distance between the flexible cantilever plate and the fixed plate is about 800 μm. The samples were mounted on the top of "T" by using GE varnish and situated inside a brass can. The cantilever probe allowed for *in situ* rotation of the sample. In the presence of a magnetic field, the interaction between applied magnetic field and magnetic moment of the sample creates a torque, $\tau = \mathbf{M} \times \mathbf{B}$ as shown in Figure 3.2. This torque deflects the T-shaped cantilever and changes the capacitance between the cantilever and the fixed reference plate. In order to monitor the change in capacitance we used a General Radio 1616 capacitance bridge operating at 1KHz (it can detect changes better than a part in 10^6) coupled with a PAR 124A lock-in amplifier.

The measured oscillations in the torque arise from the anisotropy in the areas of the Fermi surface, such that

$$\tau = -\frac{1}{F}\frac{dF}{d\theta}\bar{M}\,\mathrm{HV}, \tag{3.18}$$

where F is the dHvA frequency, θ is angle of the applied field, $\bar{M}$ is the magnetization given with LK equation and V is the volume of sample. As can be seen from the above equation, if the Fermi surface has roughly spherical shape, the change in $dF/d\theta$ will be zero, therefore the torque signal will also be zero. In addition to that , since τ is inversely proportional to F, this technique is most sensitive to low frequencies. A possible drawback of this technique is that the Fermi surface of the sample must be anisotropic. If the applied field is along the symmetry axis of the sample, then the net

Reproduced with permission of the copyright owner. Further reproduction prohibited without permission.

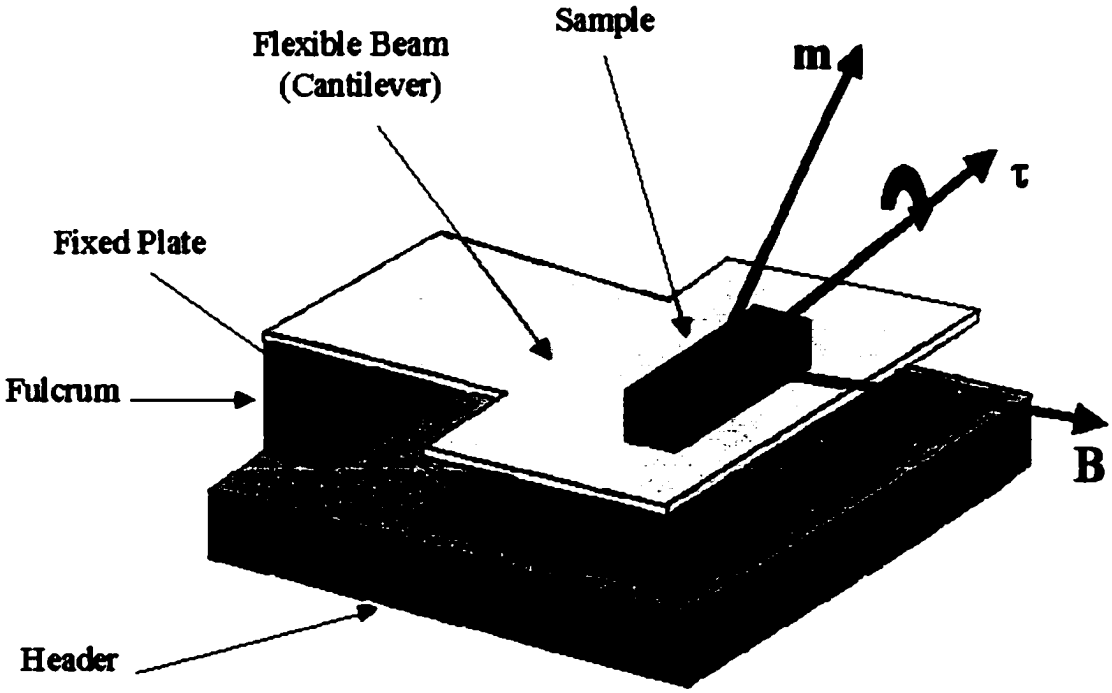

Figure 3.2 The schematic of a capacitive cantilever magnetometer. The sample is attached to the flexible plate. By applying a magnetic field **B**, the torque $\boldsymbol{\tau} = \mathbf{m} \times \mathbf{B}$ deflects the lever. Measurement of deflection gives information about sample magnetization.

Reproduced with permission of the copyright owner. Further reproduction prohibited without permission.

torque on the sample will be zero. Another drawback of this technique is that the applied magnetic field should be high, because as can be seen from equation 4.1, τ is directly proportional to H, that is, for the lowest field the torque signal drops off rapidly. In this study measurements were carried out up to 20 Tesla (T) and 30 T using a superconductive and a resistive magnet.

3.6.3 The Pulsed Field Method

During the early 1950s superconducting magnets were not available for observing Landau Quantum Oscillations. Iron magnets, limited to 2 or 3 T, were being used. Although some water cooled coils in a few special installations were available, generator ripples and poor homogeneity made their use difficult. To overcome these difficulties, associated with inhomogeneous fields and limitations of electromagnets, Shoenberg [107, 109, 97] developed a pulsed field technique to observe the higher frequency dHvA oscillations.

In the work reported here, a 50 T pulsed magnet with 24 mm diameter bore was used to observe dHvA oscillatoins at the NHMFL, Los Alamos. The measurements were made at temperatures down to 0.4 K by pumping on ^{3}He and ^{4}He reservoirs. A typical pulse magnet used at NHMFL consists of about 300 turns of rectangular cross section wire (2 x 3 mm) in ten layers. The height of the magnet is about 100 mm. Because of the huge stresses on the magnet, some special strong alloy wires and additional reinforcements are used to hold the coils together. The schematic of a pulse magnet and experimental set up used in this work is shown in Figure 3.3. In order to produce high pulsed fields, a 1.6 mega joule capacitor bank was charged to 10kV and then discharged thorough the magnet. Because of the high current on the coil (peak

Reproduced with permission of the copyright owner. Further reproduction prohibited without permission.

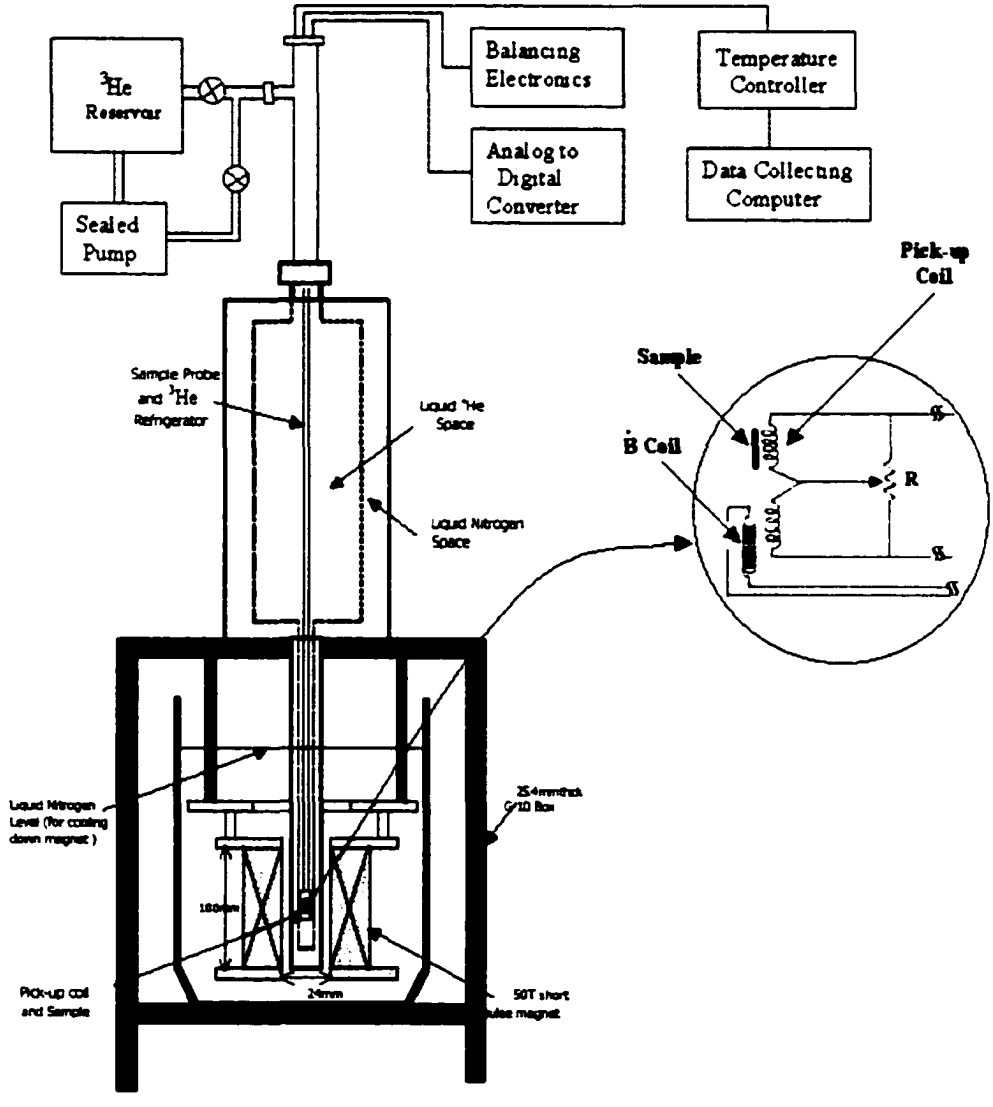

Figure 3.3 The schematic of the experimental set up for pulse field measurement.

Reproduced with permission of the copyright owner. Further reproduction prohibited without permission.

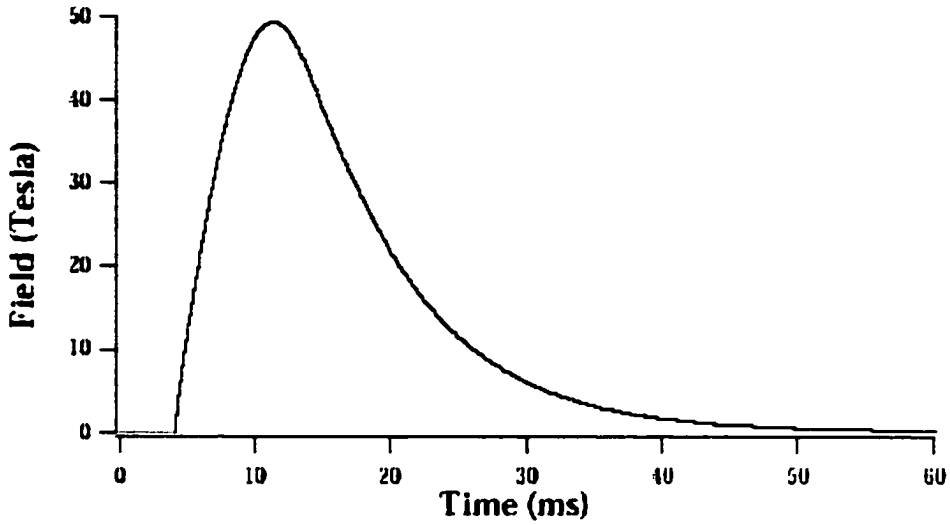

Figure 3.4 Field profile of 50 Tesla pulse field magnet at LANL.

current can reach 25kA), the magnet heats up quickly. For that reason, liquid nitrogen is used to cool down the magnet and to decrease power dissipation. The magnet used had a rise time from zero to 50 T of approximately 6 ms and the field decreased to zero in 25-30 ms. The field profile of the magnet is shown in Figure 3.4.

To measure the oscillatory magnetization, a set of compensated pickup coils was used as shown in the inset to Fig 3.3. These are two coils which are made as equal (i.e NA is the same, where N is the number of turns and A is the cross sectional area) to each other as possible such that the applied field induces the same voltage in each coil. One coil, called pickup coil, is for sample and the other, called cancellation coil, is for balance. The sample pick up coil was a small solenoid made from copper wire wound with an inner diameter of 0.38mm. A counter wound cancellation coil was wound co-

Reproduced with permission of the copyright owner. Further reproduction prohibited without permission.

axially on the outer diameter of the central pickup coil. The number of turns on the cancellation coil was adjusted to balance the induced voltage in the inner coil in the absence of the sample, so they form a balanced pair. Both coils were connected to an external voltage balancing and an amplification circuit. When the sample was inserted into the pickup coil, a large imbalance in the pickup coil pairs was observed due to magnetization of the sample. With the external balancing circuitry we adjusted this imbalance using a 10 T pulse.

The field produced by the pulsed magnet was measured with a coil which is separated from the sample pickup coil and the cancellation coil. This coil is often called " *B dot coil*" ($\dot{B}$=dB/dt) and has a known value of NA. The magnetic field B is measured by integrating the voltage V, which is induced in the B dot coil, over the time interval of the pulse. This voltage is proportional to dB/dt, thus, B(t)= C $\int$(dB/dt)dt, where C is the field conversion factor. In this study, C was calibrated by using the dHvA frequency of the copper wire in the pickup coil.

The major concern of this method is heating of the sample due to eddy currents. In order to avoid heating of the sample, the sample geometry can be selected such as the radius of the sample is much smaller than its length. In this case, Joule heating due to eddy currents can be greatly reduced [110]. The samples used in this method were either etched down (using a 25% HCl in H_2O solution) or chopped to dimension of < 0. 4 mm to reduce their diameter. By choosing small samples, it can be both avoided eddy current and minimized the effect of field inhomogeneity.

Reproduced with permission of the copyright owner. Further reproduction prohibited without permission.

3.6.4 Field Modulation Method

For a third technique, a modulation coil and a pair of balanced pick up coils were used to measure dHvA oscillations. The pick up coil was inserted inside the modulation coil and they were situated on the sample probe. After placing the sample inside the pickup coil, the sample probe was placed in the center of a homogeneous (superconductor) magnet. Then an AC current was passed through a modulation coil to produce a modulation field. (To maximize the dHvA signal amplitude, different frequencies were used.) That is, a small time dependent AC modulation field $h_o \cos wt$ and large homogenous field H were superimposed. By using a lock-in amplifier (PAR 124A), the voltage output v, from the imbalance in coil was measured as

$$v = c\frac{dM}{dH}(-h_0 w \sin wt), \tag{3.19}$$

where h_o is the magnitude of the modulation field and w is the modulation frequency. Although the field modulation measurements for the dHvA effect have some sensitivity advantage over the torque measurements (near symmetry axes $d\theta/dF$ can be small and small torque signals are produced), they have a disadvantage for the low frequencies (F < 1kT) due to difficulty of producing a modulation field of sufficient magnitude to give large values of dM/dH.

Reproduced with permission of the copyright owner. Further reproduction prohibited without permission.

CHAPTER 4

DHVA MEASUREMENT ON $Ce_xLa_{1-x}RhIn_5$ *

In this chapter, we will report the results of experimental measurements on $Ce_xLa_{1-x}RhIn_5$ compounds. In this work, the dHvA measurement were first carried out on the host metal $LaRhIn_5$. Then Ce ion was substituted in $LaRhIn_5$ compounds with different incremental steps up to pure $CeRhIn_5$. This is a powerful method to understand the formation of the heavy fermion state in Ce_xLa_{1-x} -intermetalic compounds. In other words, it is a very useful method to investigate the nature of *f* electrons and to observe the change in effective masses and Fermi surface topology of the host metal. As discussed in the previous chapter, the experiments were done with three different techniques. The concentrations of the samples and the techniques used for dHvA measurements are given in Table 4.1. Because of the anisotropic tetragonal structure of all of the samples, the Fermi surface of the samples were measured with the field along both the [001] and [100] directions.

4.1 dHvA Measurements on $LaRhIn_5$

The dHvA frequencies and effective masses of pure $LaRhIn_5$ were measured for both [100] and [001] crystallographic directions at NHMFL, Tallahassee. In addition, in order to determine Fermi Surface shape, angular dependence measurements were made on this sample. The dHvA frequencies and effective masses were measured by using the field modulation technique at the temperature down to 1.75 K at NHMFL

---

*Part of this Chapter has been published in " Localized *f* electrons in $Ce_xLa_{1-x}RhIn_5$: de Haas van Alphen Effect" U. Alver, R. G. Goodrich, N. Harrison, D. W. Hall, E. C. Palm, T. P. Murphy, S. W. Tozer, P. G. Pagliuso, N. O. Moreno, J. L. Sarrao, and Z. Fisk, *Phys. Rev. B*, **64** 180402 (2001).

Reproduced with permission of the copyright owner. Further reproduction prohibited without permission.

Table 4.1 Techniques used for dHvA measurement on $Ce_xLa_{1-x}RhIn_5$ compounds.

Method	Sample($Ce_xLa_{1-x}RhIn_5$)	Crystallographic Orientation
Pulse field	x=0.1, 0.5, 0.6, 0.75	H ‖ [001]
	x=0.1, 0.4, 0.5, 0.6, 0.75, 0.9, 0.97	H ‖ [100]
Field Modulation	x= 0.00, 0.1, 0.25	H ‖ [001]
	x=0.00	H ‖ [100]
Torque	x=0.01, 0.05, 0.90, 0.97, 1.00	H ‖ [001]
	x=0.01, 0.05, 0.25, 1.00	H ‖ [100]

Table 4.2 Measured frequencies and cyclotron masses of $LaRhIn_5$.

B ‖ a		B ‖ c	
Frequency	Effective Mass	Frequency	Effective Mass
F1=365	0.086 ± 0.016	f1=601	
F2=443	0.097 ± 0.114	f2=3654	0.61 ± 0.03
F3=783	0.096 ± 0.034	f3=3849	
		f4=4593	0.65 ± 0.02
		f5=4995	0.66 ± 0.05
		f6=5800	0.56 ± 0.06
		f7=6302	0.62 ± 0.03
		f8=7710	1.08 ± 0.11

Tallahassee. The analysis of measurements, i.e. calculation of the effective masses and frequencies, will be given in detail in the following sections of this chapter. The measured frequencies of the metalic $LaRhIn_5$ are shown in Figure 4.1 and measured cyclotron effective masses are given Table 4.2 for both crystallographic directions. We observed three fundamental dHvA frequencies, F1, F2 and F3 along the [100] direction and eight dHvA frequencies, f1 to f8 and their harmonics along the [001] direction. As shown in these figures, the measured frequencies span the range from about 600T to 6300T for the field parallel to [001] direction and the range from about 360 to 780T for the field parallel to [100].

Reproduced with permission of the copyright owner. Further reproduction prohibited without permission.

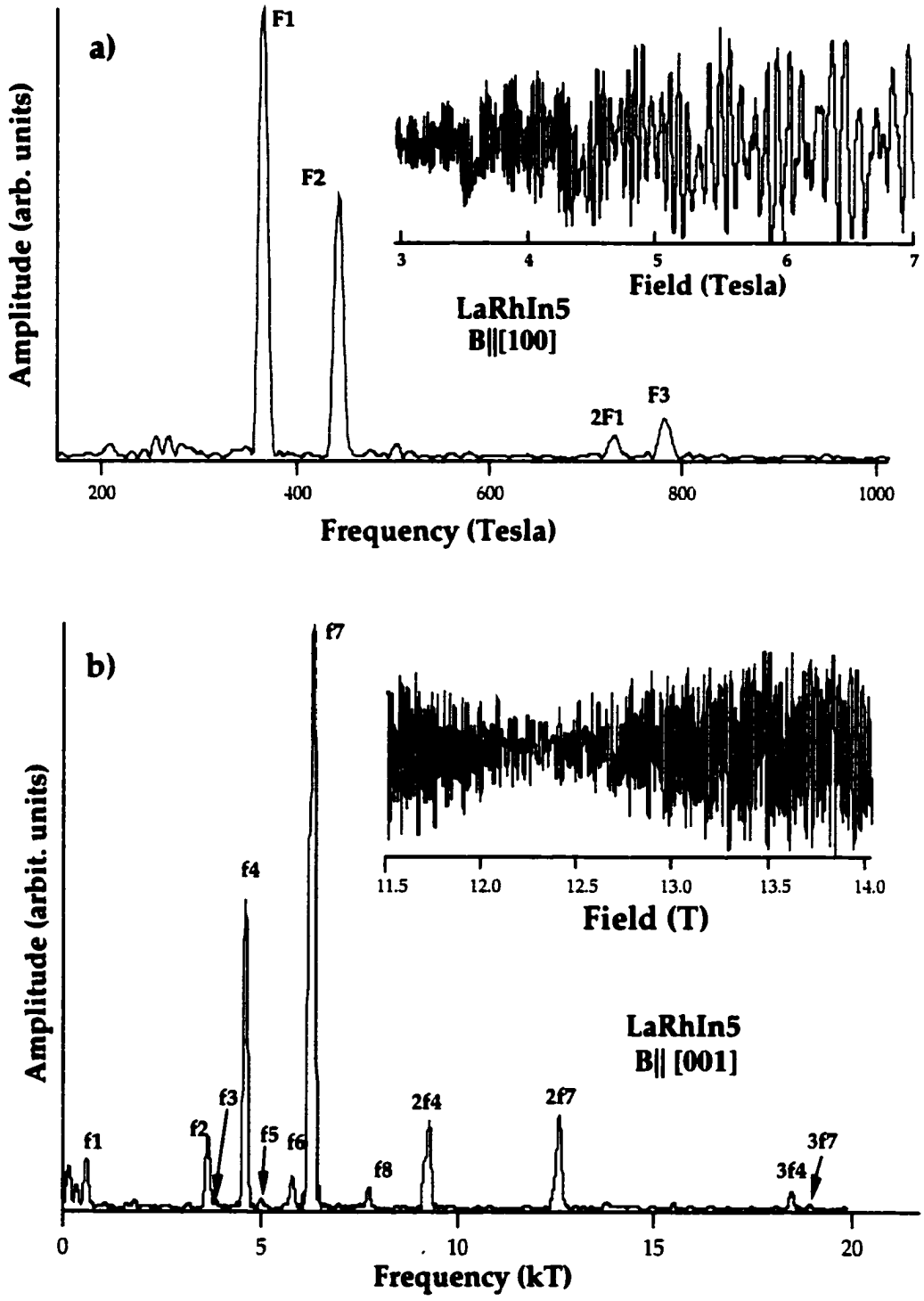

Figure 4.1. dHvA oscillation (inset) and its Fourier transform for $LaRhIn_5$ a) for the field along the [100] direction at T=2.44K, b) for the field along the [001] direction at T= 1.75K.

Reproduced with permission of the copyright owner. Further reproduction prohibited without permission.

4.2 dHvA Measurements on $CeRhIn_5$

DHvA measurements of $CeRhIn_5$ were made at NHMFL, Tallahassee by using cantilever magnetometry. The details of this technique are given in Chapter 3 and physical properties of $CeRhIn_5$ are given in Chapter 2 in this dissertation. The measurements were carried out at temperatures from 20 mK to 500 mK by pumping ^3He and ^4He reservoirs and at the applied field from 5 to 18T by using a superconductor magnet. Complete field rotations in the (100) and (001) planes of the tetragonal structure are obtained. The measured dHvA frequencies are shown in Figure 4.2 for the field along [100] and [001] directions. As can be seen, there are several fundamental frequencies and several combinations (especially with the F_7; e.g. F_7-F_6= 1302T). Similar field combinations were found in all field directions. The origin of these combinations might be the strong magnetic interactions between electrons on different parts of the Fermi surface or torque interactions due to the use of a cantilever. Either of these effects can give rise to series of frequencies that are combinations of two fundamental ones [99]. The angular dependence of measured frequencies is given in Fig. 4.3. As can be seen, the frequency range spans 100 T to 5 kT for the field applied near [001]. In addition, measurements show that the Fermi surface of $CeRhIn_5$ has both small pockets of 3D character and large undulating cylinders that should give rise to a 2D character in other properties. The measured cyclotron mass of carriers, determined from the temperature dependence of the dHvA amplitude, and the calculated cyclotron mass, determined from band theory, are summarized in Table 4.3 and Table 4.4 for both [100] and [001] direction respectively. As seen in these tables, all measured effective masses are greater than the free electron mass and are anisotropic, varying

Reproduced with permission of the copyright owner. Further reproduction prohibited without permission.

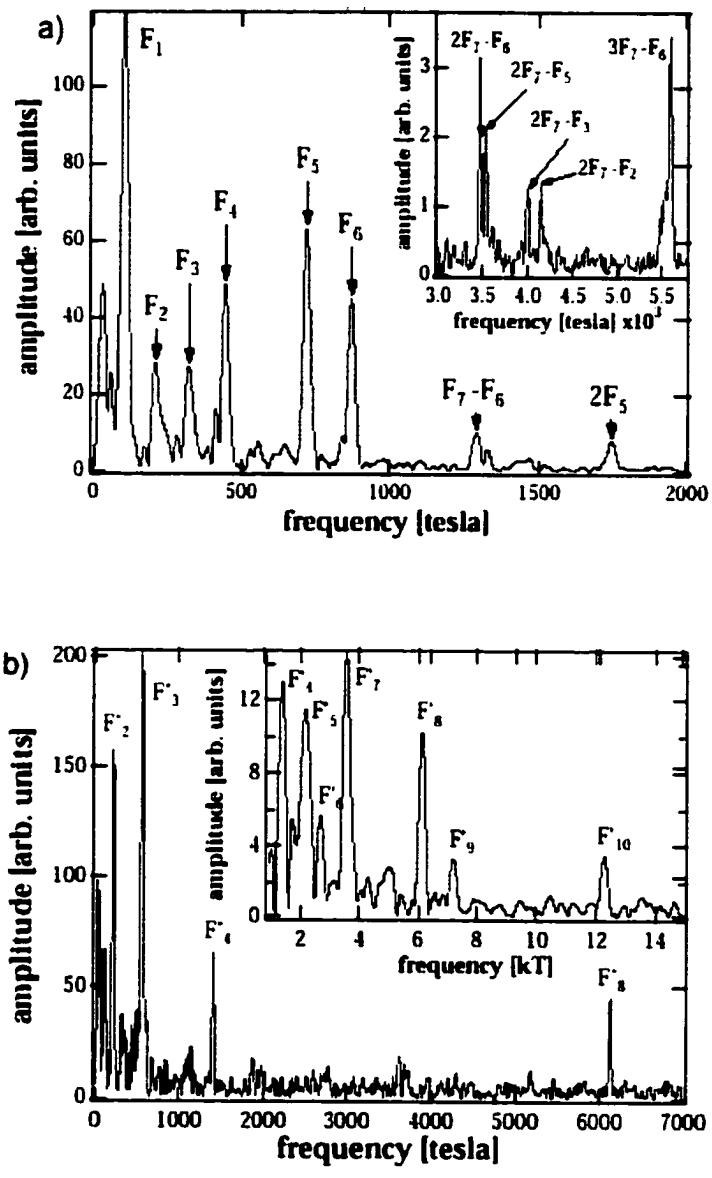

Figure 4.2 a) dHvA frequencies of $CeRhIn_5$ with the field along the [100] direction. The inset shows some of the high frequencies that are the combinations of the fundamentals. b) dHvA frequencies of $CeRhIn_5$ with the field along the [001] direction.

Reproduced with permission of the copyright owner. Further reproduction prohibited without permission.

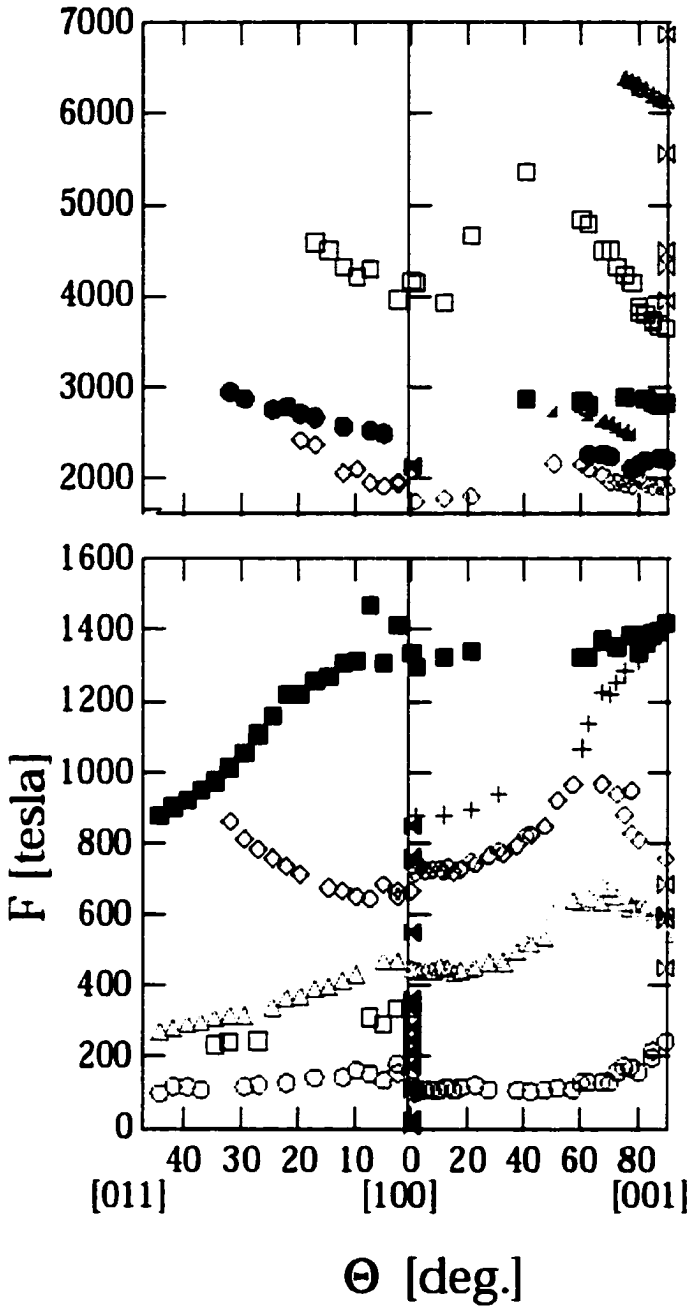

Figure 4.3. Angular dependence of dHvA frequencies for $CeRhIn_5$. Calculated frequencies for [001] and [100] directions are indicated with bowties.

Reproduced with permission of the copyright owner. Further reproduction prohibited without permission.

Table 4.3 Measured and calculated dHvA frequencies and measured effective masses for $CeRhIn_5$ with B along the [100]. Frequencies listed by Cornelius have been corrected by 4.5% (Ref. [68]).

Calculated F(T)	Measured F (T)	F(T)[68]	Measured m *
2139	F_7=2176		
849	F_6=874	861	3.3±0.6
761	F_5=722	714	2.0±0.8
551	F_4=446	492	3.9±0.9
362			
342			
337	F_3=324	295	5.5±1.0
283			
245			
214	F_2=212	219	2.9±0.4
175			
110	F_1=106	105	3.3±0.6
26			
22			
21			
10			
9			

Table 4.4 Measured and calculated dHvA frequencies and measured effective masses for $CeRhIn_5$ with B along the [001]. Frequencies listed by Cornelius have been corrected by 4.5% (Ref. [68]).

Calculated F(T)	Measured F (T)	F(T)[68]	Measured m *
12326	F'_{10}=12280		
12126			
11268			
6878	F'_9= 7200		
5562	F'_8= 6120	6256	6.1±0.3
4502		4686	(8.4±1.0)[68]
4331			
3951	F'_7=3600	3605	4.6±1.0
	F'_6=2740		
	F'_5=2160		
	F'_4=1412		4.5±0.3
686			
597			
585	F'_3=562		
451			
	F'_2=216		
	F'_1=115		

Reproduced with permission of the copyright owner. Further reproduction prohibited without permission.

from $2m_0$ to $6m_0$ depending on direction. In addition to experimental Fermi surface measurements, total energy and band structure of $CeRhIn_5$ were calculated with the full-potential electronic structure method and the Fermi surface of $CeRhIn_5$ was calculated by using a fine mesh method [77]. The Fermi surface sheets, formed three double degenerate bands, shown in Figure 4.4a, Figure 4.4b and Figure 4.4c. In these figures, Γ, the center of conventional Brillouin zone, is at the corner of cubes. In Figure 4.4a the lowest energy sheet which consists of hole surfaces centered around Γ and X. In Figure 4.4b, the sheet has both electron and hole surfaces. The sheet shown in Figure 4.4c is mostly an electron surface, but a large hole surface is also seen on that sheet.

When we compare the calculated and measured frequencies shown in Table 4.3 we see that there are 17 calculated frequencies. Five of them ranging from 9 to 26 T were not observed experimentally for the field along the [100] direction. The reason for this is that, these frequencies are too low to be observed in the field range from about 7 to 18 T. That is, the number of oscillations for given field range is not enough to observe these frequencies. For example, for a 10 T orbit there is only 1 oscillation, and for a 26 T orbit there are only about 2 oscillations in the field range from 7 to 18 T. But below 7 T we could not observe any clear dHvA frequency. Therefore, data analysis in this direction was done for the field range between 7 and 18 T. However, as seen in Table 4.3, the 7 measured frequencies are in the same range as predicted frequencies from the band calculation. Thus, it appears that for the field in this direction the measurements give the strong support to the predicted Fermi surface.

But the agreement between the calculated and measured frequencies is not as good for the field in the [001] direction. Although we have observed 10 frequencies

Reproduced with permission of the copyright owner. Further reproduction prohibited without permission.

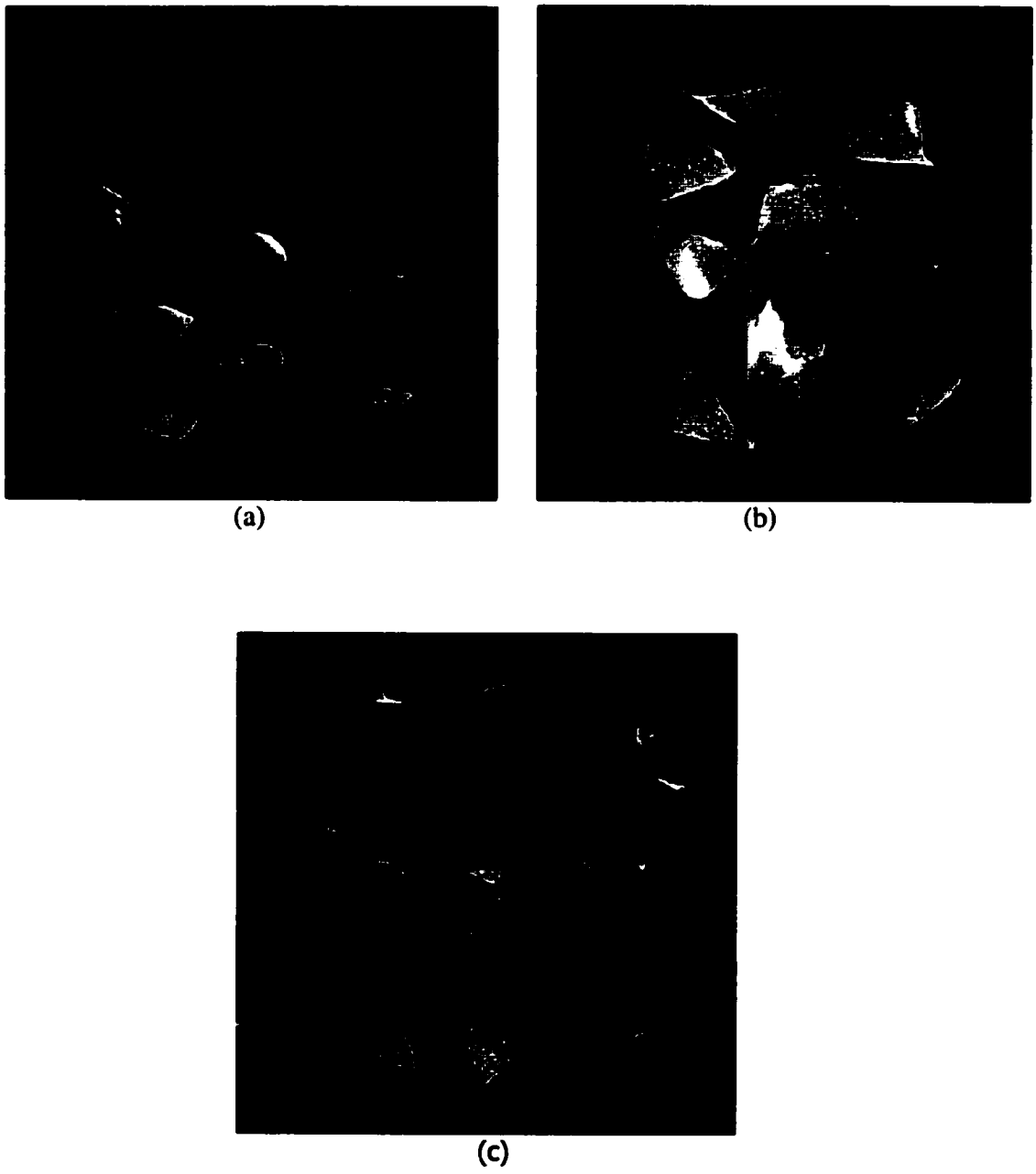

Figure 4.4 a) The first, b) the second and c) the third sheet of parametric $CeRhIn_5$ Fermi surface. The electron surfaces are illuminated.

Reproduced with permission of the copyright owner. Further reproduction prohibited without permission.

from the dHvA experiment, 13 frequencies were calculated from band theory. We have observed only one high frequency, 12280 T, out of three calculated high frequencies. This high frequency only is observed at 20 mK and it indicates that this orbit has a very large effective mass. The fact that only one rather than three frequencies were observed may indicate the electron surface is much more cylindrical than is obtained from band theory. For the remainder of the frequencies, only the total number observed frequencies agree with the calculation, but there is a considerable size difference between calculated and measured orbits. The reason for this disagreement might be the behavior of 4*f* electron in $CeRhIn_5$ because the band calculations are based on the assumptions of a completely itinerant 4*f* electron in Ce atoms. As will be seen in the following section this is not the case. We have clearly observed that the 4*f* electron in Ce atom is almost entirely localized. In this case, a new band calculation, including localized *f* electron behavior, is required to predict a more realistic Fermi surface.

4.3 dHvA Measurement on $Ce_xLa_{1-x}RhIn_5$

The samples used for these measurements were single crystals of $Ce_xLa_{1-x}RIn_5$ intermetalics with x=0.00, 0.01, 0.05, 0.10, 0.25, 0.40, 0.50, 0.60, 0.75, 0.90, 0.97, and 1.00. We have already discussed the samples for x=0.00 and x=1.00 in section 4.1 and 4.2 respectively. In the following sections we will present the results of the dHvA measurements for the rest of the samples.

4.3.1 Measurements of dHvA Frequencies of the $Ce_xLa_{1-x}RhIn_5$ Compounds

All frequency measurements were carried out on the single crystals of $Ce_xLa_{1-x}RhIn_5$ compounds with the field along the [100] and [001] directions. The dHvA data sets, recorded with three different techniques mentioned in Chapter 3, were analyzed in the following way: the recorded field values were converted to inverse field (in this

Reproduced with permission of the copyright owner. Further reproduction prohibited without permission.

way dHvA signal would be seen as periodic), so that dHvA data set was interpolated to produce a new data set in 1/B. Then this interpolated data set was subjected to Fourier Transform to determine the frequencies. In this work, two different programs, written in Igor Pro* and Labview**, were used to analyze the dHvA frequencies. Three versions of a Fourier transform algorithm were used to determine the dHvA frequency: preliminary analysis was done with a fast Fourier Transform (FFT) and in many cases a discrete Fourier Transform (DFT) and super fast Fourier Transform (SprFFT) were used to increase the frequency resolution. Figure 4.5a) and b) show a cantilever dHvA signal and associated Fourier spectra for x=0.05 at 1.3K with the field along the [100] direction. For this field direction, similar to $LaRhIn_5$, three fundamental frequencies, F1, F2 and F3, and their harmonics were observed for all of the samples in the series. In pulse field measurement, most of data sets were analyzed for falling field due to the long fall time (about 25ms) compared to the rise time (about 6 ms). Figure 4.6 shows both falling and rising field data for x = 0.5 at 1.43K for B || [001] and Figure 4.7 shows its corresponding Fourier transform for falling pulsed field data in the field range between 20 and 30T. In this field direction, seven fundamental dHvA frequencies, f1, f2, f3, f4, f5, f6 and f7, were observed for all of the samples in the series. Although the lowest frequency f1 appears to be very weak in this pulse field measurement in Fig.4.7, it was observed to be a distinct peak in the cantilever measurements. One of the problems of pulsed field measurements is that the pulse field signal amplitudes are proportional to dM/dH and this factor is small for low frequencies. On the other hand, torque cantilever measurements are most sensitive to

* Igor Pro v.3 by Wave Metrics, Inc. P.O. Box 2088, Lake Oswego, OR, 97035
**Labview, 4.1 by National Instrument

Reproduced with permission of the copyright owner. Further reproduction prohibited without permission.

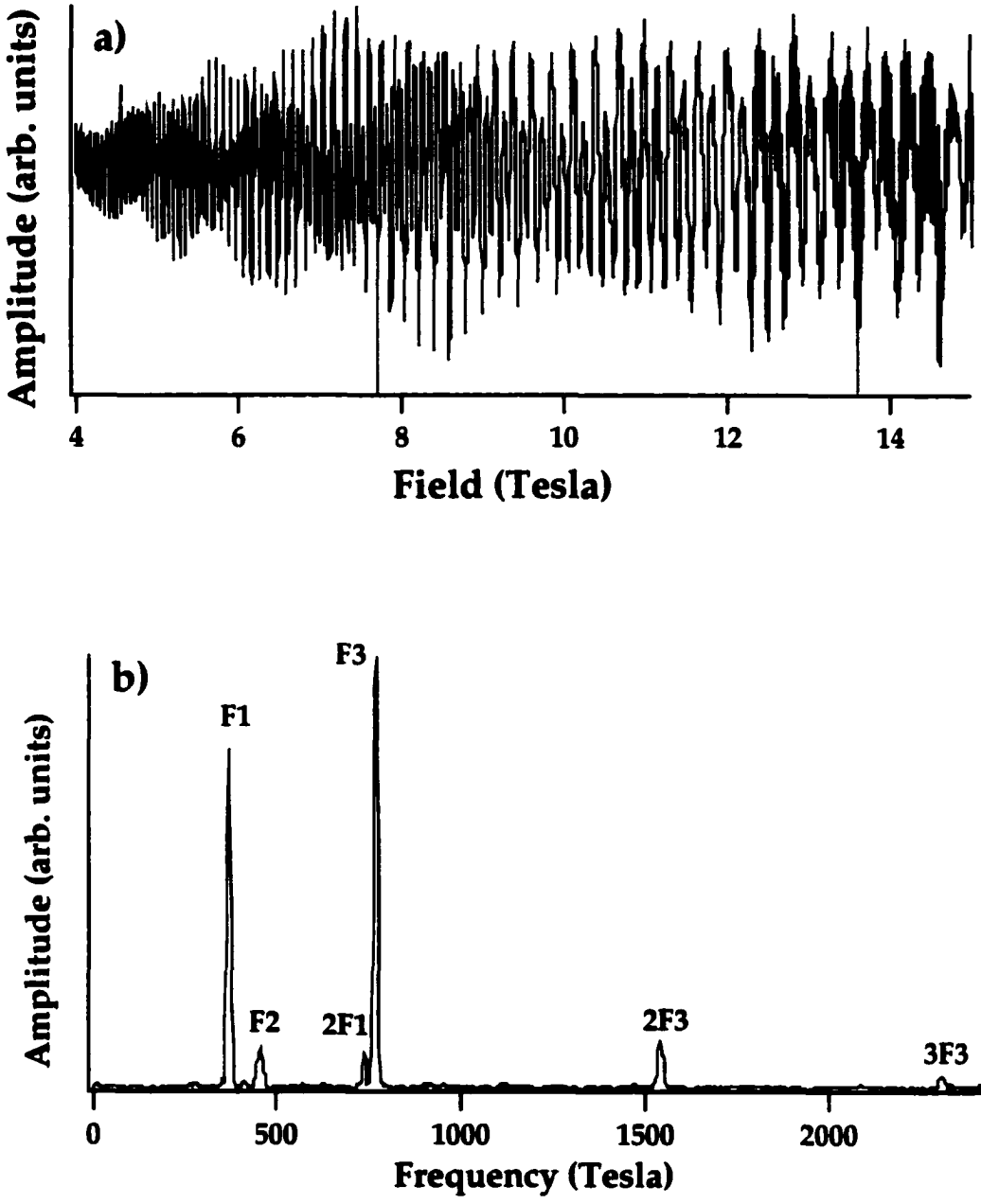

Figure 4.5 a) The torque oscillation of the $Ce_{0.05}La_{0.95}RhIn_5$ sample at 1.3 K for B || [100] and b) its corresponding Fourier transform.

Reproduced with permission of the copyright owner. Further reproduction prohibited without permission.

Reproduced with permission of the copyright owner. Further reproduction prohibited without permission.

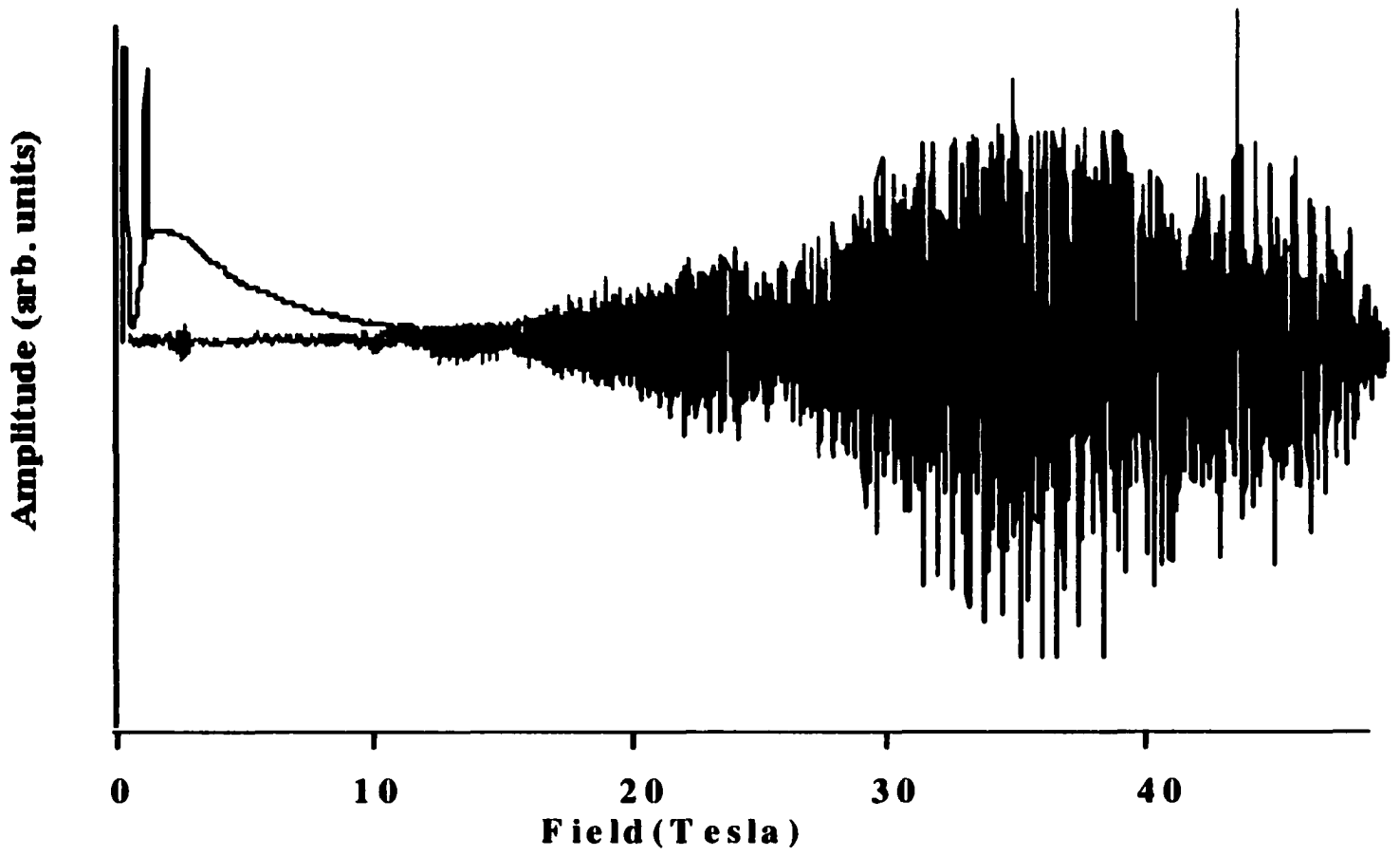

Figure 4.6. Pulse field data for $Ce_{0.5}La_{0.5}RhIn_5$ for the field along the [001] direction at 1.43K. The dark lines represent the rising field and the light lines represent the falling field.

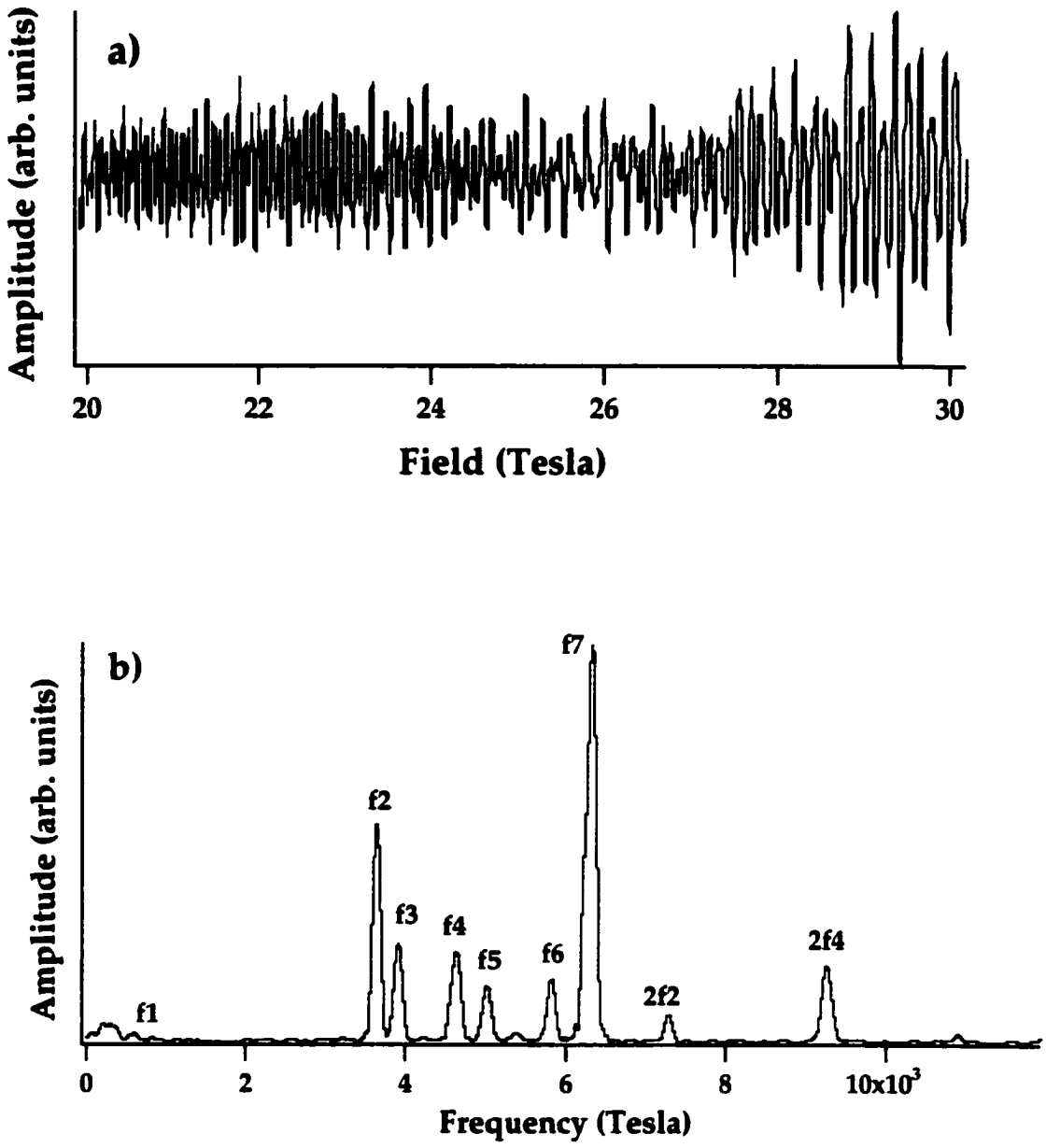

Figure 4.7 a) dHvA oscillations of a pulsed measurement for $Ce_{0.5}La_{0.5}RhIn_5$ at 1.43 K for B || [001] and b) its corresponding Fourier transform.

Reproduced with permission of the copyright owner. Further reproduction prohibited without permission.

low frequencies due to the $1/F$ factor in their signal amplitude. Moreover, as can be seen in Fig. 4.7, we could not observe the 7710 T orbit of $LaRhIn_5$ along the series. Throughout this investigation, we have observed frequencies other than the fundamental frequencies listed above. Some of these are due to harmonics of the fundamental frequencies and some are combination frequencies that can arise in a variety of ways.

4.3.2 Concentration Dependence of Frequencies

After determining the dHvA frequencies for each sample for both orientation, we studied the concentration dependence of the measured frequencies. Figure 4.8a) and Figure 4.8b) show the Ce concentration dependence of the measured dHvA frequencies for the magnetic field along the [100] and [001] direction, respectively, with x = 0 being pure $LaRhIn_5$. In these plots, the dotted lines are included only as a guide to the eye. As can be seen in these figures, there is only a small change in frequencies with increasing Ce concentration for both field directions. Within the experimental error due to the sample alignment relative to magnetic field direction and width of the Fourier analysis peaks there are no changes in frequencies for B || [001]. These frequency measurements indicate that the volumes of the Fermi surface of $LaRhIn_5$ and $CeRhIn_5$ are the same. Thus, there is no significant dependence on the Fermi surface topology on x, apart from two small exceptions: First, one very low frequency in $LaRhIn_5$ of about 7 T, originating from a packet that occupies less than 1 part in 10^4 of the Brillouin zone volume, is not present in these alloys [111]. Second, two distinct but closely spaced frequencies, f6 and f7 (for B || [001]), can only be individually resolved for $x \leq 0.95$. For the low frequencies seen with B || [100], a slight

Reproduced with permission of the copyright owner. Further reproduction prohibited without permission.

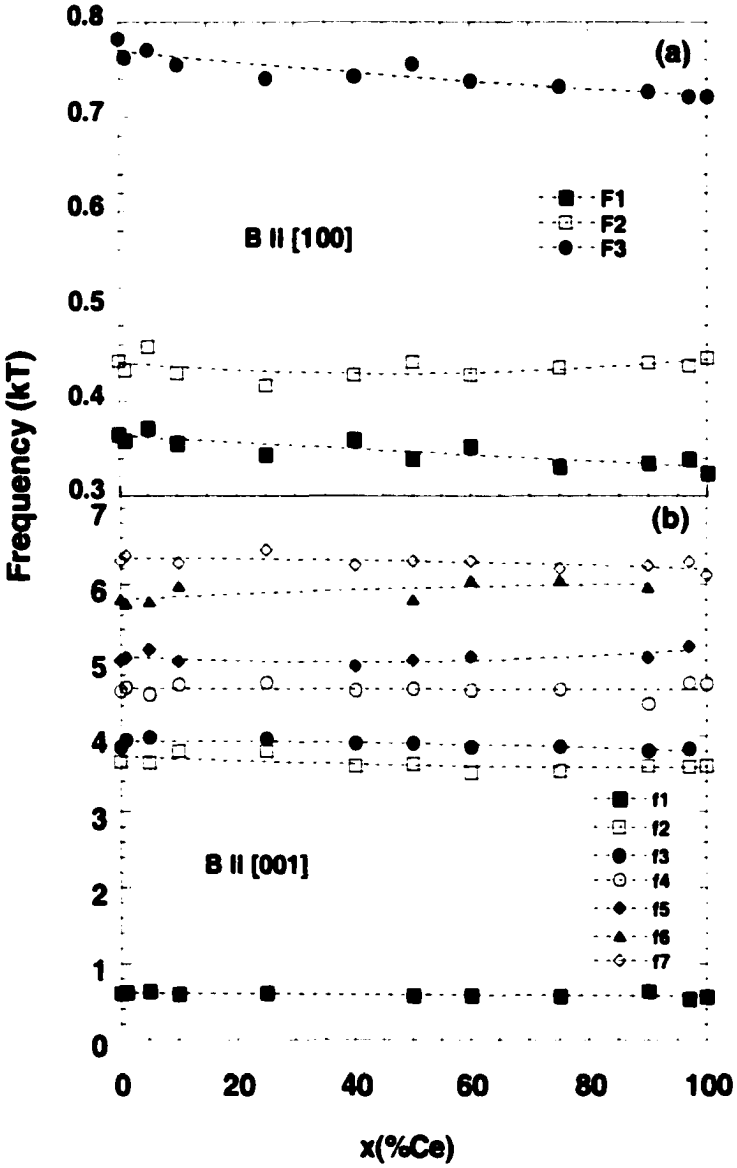

Figure 4.8 a) Concentration dependence of dHvA frequencies for B || [100] and b) for B || [001]. The dotted lines are a guide for the eye.

Reproduced with permission of the copyright owner. Further reproduction prohibited without permission.

(~5-10%) decrease in F1 and F3 is observed with F2 unchanged. It should be noted that the changes in these low frequencies are again within the experimental errors as mentioned before.

As we discussed in section 4.2, there was some degree of similarity between the dHvA data and the itinerant 4*f* electron band structure for the field along the [100] direction. However, the calculated and measured frequencies were not in agreement for B ‖ [001]; for example, the average fractional frequency difference between calculated and measured values, $[(F_{exp}-F_{BS})/F_{exp}]$, is 0.44 for B ‖ [001]. Therefore, it was unclear from the measurements and calculations whether the 4*f* electrons are itinerant or localized. The results presented in Figure 4.8 show that, because of absence of any strong dependence of the frequencies on x, the addition 4*f* electrons do not change the Fermi surface volume and, therefore, they must be almost entirely localized. Of course, this conclusion is rigorous, because it does not depend on the ability of the band structure calculations reproduced with experimental data.

Similar to $CeRhIn_5$, the localized 4*f* electron picture was observed in a number of heavy fermion system, for example CeB_6 [112], $CeRu_2Si_2$ [113], $CeAl_2$ [114], and $CeCu2Si_2$ [115], at high fields. It has been concluded that, by using similar experiments in La analogues, all these heavy fermion compounds [112-115] exhibit localized *f* electron behavior at high magnetic fields where *f* alignment occurs. In other words, the Fermi surface topology of these compounds is similar to their La analogues.

4.3.3 Measurements of Cyclotron Masses of the $Ce_xLa_{1-x}RhIn_5$ Compounds

The effective masses of carriers on various orbits throughout the series were determined from the temperature dependence of the dHvA signal. Temperature measurements were performed at least for five different temperatures in the range 0.45 $K \leq T \leq 6K$, and monitored using calibrated Cernox thermometers for the field parallel

Reproduced with permission of the copyright owner. Further reproduction prohibited without permission.

to [100] and [001] directions . In order to calculate the cyclotron mass of the carriers, an interval (a field range) containing a fixed number of oscillations is chosen along the 1/B axis and the same interval is used for each temperature. Using the result of Fourier transform analysis, the amplitudes of each frequency, A, were determined from the peak heights. Then the determination of cyclotron mass was done in two different ways: first, the amplitude, A of each frequency was plotted against temperature T. An example is shown in Figure 4.9 for x = 0.97 for the field range of 20–30 T. Then, this temperature dependence was compared with the following theoretical reduction factor, R_T in the LK equation;

$$R_T = \frac{\pi\lambda}{\sinh(\pi\lambda)} = \frac{\frac{2\pi^2 pkcT}{e\hbar H}m^*}{\sinh(\frac{2\pi^2 pkcT}{e\hbar H}m^*)}, \tag{4.1}$$

or, rearranging the above equation,

$$R_T = \frac{z_1}{\exp(z_2)-\exp(-z_2)}, \tag{4.2}$$

where

$$z_2 = \frac{2\pi^2 pkcT}{e\hbar H}m^* \quad \text{and} \quad z_1 = 2z_2. \tag{4.3}$$

That is, the amplitude vs. temperature graph was fitted by using equation 4.2 . The fitted curve is shown as a solid line in Figure 4.9. From the fit equation the parameters z_2 and z_1 was obtained and m* was calculated. The mean field (or center of field) H in equation 4.3 were obtained by taking the average of starting and final field in the chosen interval range.

In the second way, the calculation of m* was done iteratively. First, ln(A/T) was plotted against T. and by using linear regression, the slope, which is equal to zm^*/H

Reproduced with permission of the copyright owner. Further reproduction prohibited without permission.

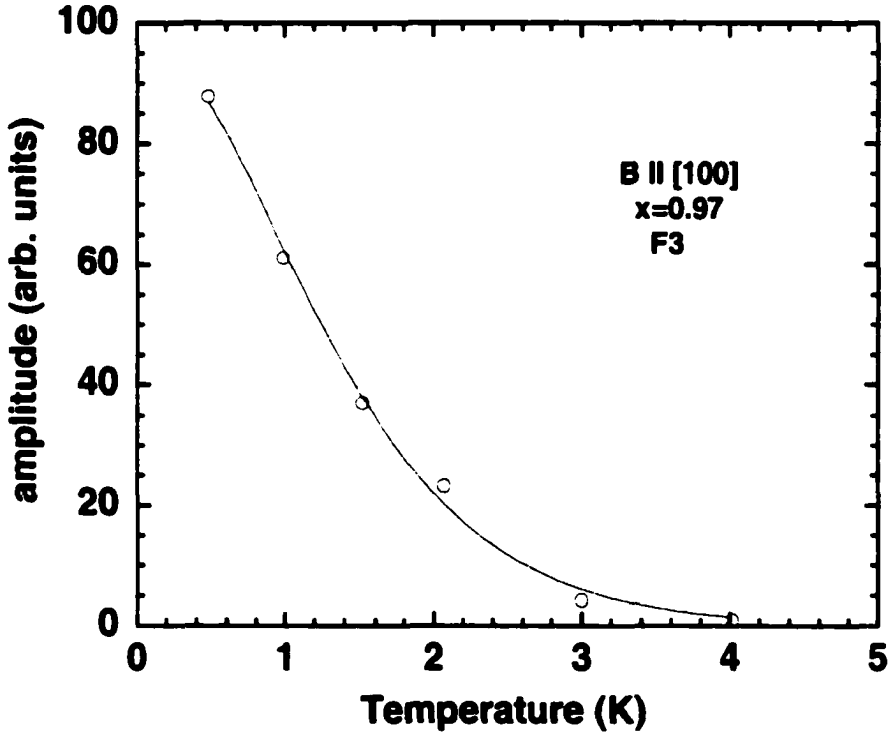

Figure 4.9 Mass plot of $Ce_{0.97}La_{0.03}RhIn_5$ for the F3 orbit with the field along the [100] direction. The solid line represents the fit corresponding to the reduction factor R_T in the LK equation.

Reproduced with permission of the copyright owner. Further reproduction prohibited without permission.

(where z =constant and $H = H_{mean}$) was obtained as a first estimation. Then, using R_T in the LK equation,

$$\ln(A[1-\exp(\frac{-2(\frac{zm^*T}{H})}{T})]) \qquad (4.4)$$

was plotted vs temperature, T and from its slope a new value of zm^*/H was determined. This new value was put back into Equation 4.4 and refit by linear regression. This procedure is repeated until the mass no longer change significantly. In both cases the m* values were the same. But the second way is an approximation for the $\sinh z_2$ and not as accurate at very low temperatures (mK). The values of effective masses determined using these procedures and measured frequencies of $Ce_xLa_{1-x}RhIn_5$ alloys ($0 \leq x \leq 1$) are summarized in Table 4.5 for B || [100] and in Table 4.6 for B || [001].

4.3.4 Concentration Dependence of Effective Masses

The effective masses of $Ce_xLa_{1-x}RhIn_5$ compounds were plotted against the Ce concentration. The concentration dependence of m* for B || [100] and for B || [001] are shown in Figure 4.10 and Figure 4.11 respectively. As can be seen from these figures, when La ions are replaced by Ce ions, the effective mass of the carriers initially increases slowly with increasing Ce concentration near x = 0.4 and then remains nearly constant until x = 0.75. But for Ce concentrations greater than 90%, a marked increase is observed in the rate of change of m* with increasing Ce concentration. This fact indicates that the interaction of conduction electrons with localized moments enhance the masses. The variation in the effective mass m* on increasing x from the single impurity limit ($x \rightarrow 0$) to the impurity lattice limit (x = 1), has yet to be understood.

Reproduced with permission of the copyright owner. Further reproduction prohibited without permission.

Table 4.5 Measured dHvA frequencies and effective masses for $Ce_xLa_{1-x}RhIn_5$ with the field along [100] direction.

x(%Ce)	Frequency	Effective Mass	Temp. Range	Field Range
0	365	0.086 ± 0.016	2.44-4.2K	2-7T
	443	0.097 ± 0.114		
	783	0.096 ± 0.034		
1	359	0.146±0.005	4.2-9K	5-12T
	433	0.184 ± 0.003		
	763	0.236 ± 0.001		
5	372	0.43 ± 0.03	2-3.75K	4-15T
	458	0.34 ± 0.09		
	771	0.21 ± 0.02		
10	365	0.21 ± 0.05	0.45-10K	4-15T
	439	0.31 ± 0.07		
	770	0.35 ± 0.05		
25	344	0.75 ± 0.16	1.6-4.4K	8-15T
	413	0.54 ± 0.27		
	744	0.61 ± 0.18		
40	360		0.43-4.5K	4-15T
	428	0.42 ± 0.03		
	743	0.37 ± 0.01		
50	340		0.5-4K	4-15T
	442	0.40 ±0.05		
	756	0.44 ± 0.16		
60	353		0.4-4.5K	6-15T
	428	0.38±0.044		
	738	0.45±0.028		
75	331		0.5-4K	4-15T
	438	0.58 ± 0.08		
	744	0.74 ± 0.14		
90	329		0.5-4K	4-15T
	441	1.01 ± 0.16		
	741	0.72 ± 0.11		
97	339		0.5-4K	4-15T
	449	1.04 ± 0.18		
	737	0.89 ± 0.05		
100	106	3.3±0.6	20-500mK	7-18T
	212	2.9±0.4		
	324	5.5±1.0		
	446	3.9±0.9		
	722	2.0±0.8		
	874	3.3±0.6		
	2176			

Reproduced with permission of the copyright owner. Further reproduction prohibited without permission.

Table 4.6 Measured dHvA frequencies and effective masses for $Ce_xLa_{1-x}RhIn_5$ with the field along [001] direction.

x(%Ce)	Frequency	Effective Mass	Temp.Range	Field Range
0	601		1.75-4.17K	5-17T
	3654	0.61 ± 0.03		
	3849			
	4593	0.65 ± 0.02		
	4995	0.66 ± 0.05		
	5800	0.56 ± 0.06		
	6302	0.62 ± 0.03		
1	617	0.25 ± 0.02	1.66-5.1K	8-11T
	3405			
	3944	0.73 ± 0.03		
	4640	0.74 ± 0.03		
	5034	1.14 ± 0.58		
	5747			
	6376	0.71 ± 0.01		
5	633	0.33 ± 0.27	1.5-4.4K	6-7T
	3647	0.64 ± 0.07		
	3978	0.49 ± 0.27		
	4558	0.58 ± 0.11		
	5139			
	5775	2.32 ± 0.47		
10	599		0.48-8K	15-17T
	3527	0.51±0.04		
	3798	0.53±0.03		
	4618	0.67±0.09		
	4985			
	5975			
	6273	0.59±0.04		
25	612		1.7-4.2K	15-17T
	3795	0.71±0.09		
	3964	0.67 ± 0.15		
	4706	1.10 ± 0.72		
	6446	1.05 ± 0.05		
40			0.45-4.5K	20-30T
	3600	0.9±0.08		
	4515	1.17±0.1		
	6310	1.35±0.03		
50	579		0.5-4K	20-30T
	3629	0.95 ± 0.02		
	3903	1.20 ± 0.03		
	4619	1.72 ± 0.05		
	4997	1.08 ± 0.03		
	5801	0.99 ± 0.03		
	6301	1.53 ± 0.04		

Reproduced with permission of the copyright owner. Further reproduction prohibited without permission.

Table 4.6 continued.

60	590		1.5-5.5K	20-30T
	3512	0.68±0.01		
	3849	1.25±0.06		
	4610	1.39±0.05		
	6051	1.625±0.09		
	6200	1.51±0.06		
75	3531	0.78 ± 0.01	1.35--4.2K	20--30T
	3858	0.88 ± 0.03		
	4613	1.46 ± 0.01		
	6051			
	6200	1.75 ± 0.06		
90	643		1.8--4.2K	22--28T
	3599	1.20 ± 0.08		
	3802			
	4422	1.55 ± 0.03		
	5028			
	5964			
	6239	2.25 ± 0.30		
97	530		1.3--3.34K	21--28T
	3597	1.67 ± 0.03		
	3829			
	4700	2.78 ± 0.4		
	5179			
	6295	3.73 ± 0.55		
100	115		20-500mK	7-18T
	216			
	562			
	1412	4.5±0.3		
	2160			
	2740			
	3600	4.6±1.0		
	6120	6.1±0.3		
	7200			
	12280			

Reproduced with permission of the copyright owner. Further reproduction prohibited without permission.

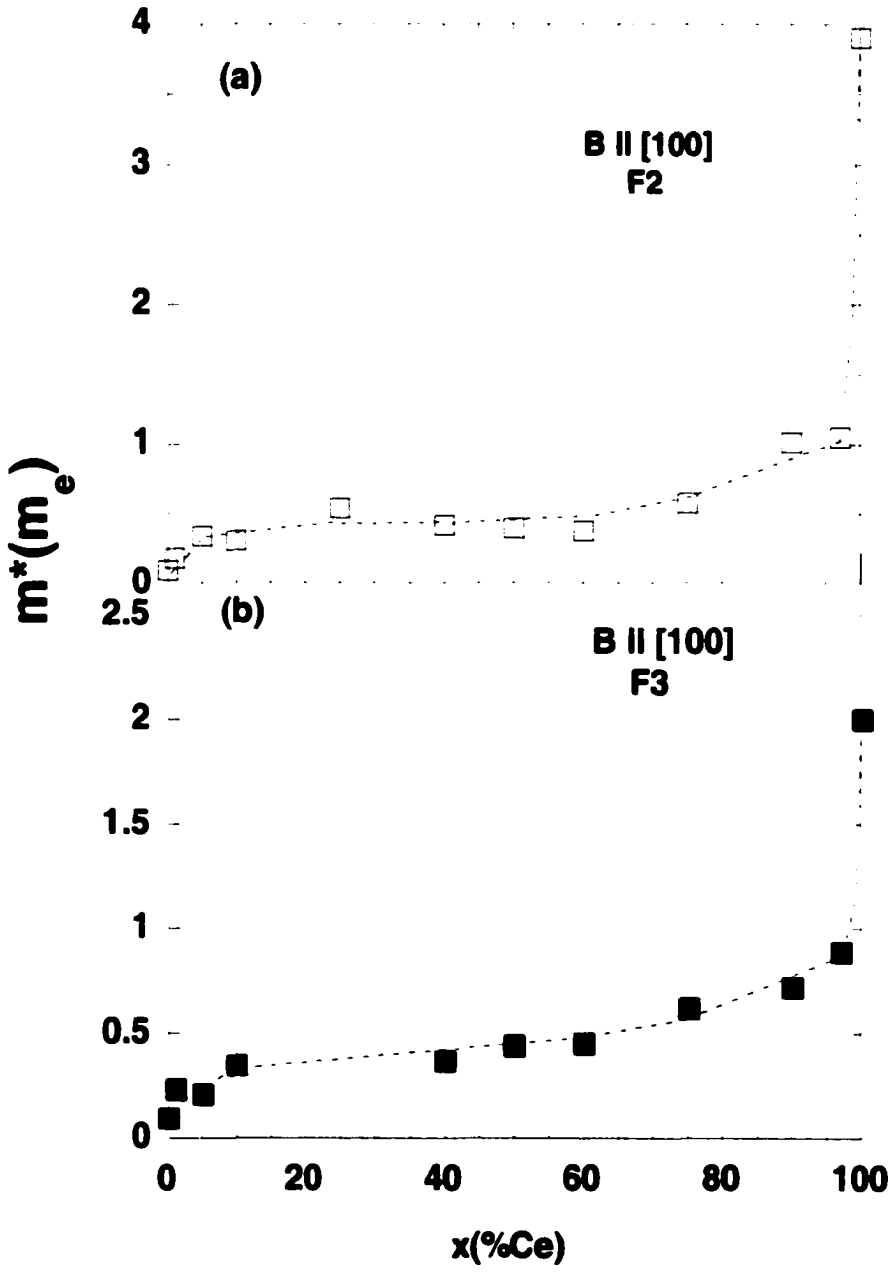

Figure 4.10 Concentration dependence of effective masses for B || [100] for two frequencies a) F2 and b) F3. The dotted lines are a guide for eye.

Reproduced with permission of the copyright owner. Further reproduction prohibited without permission.

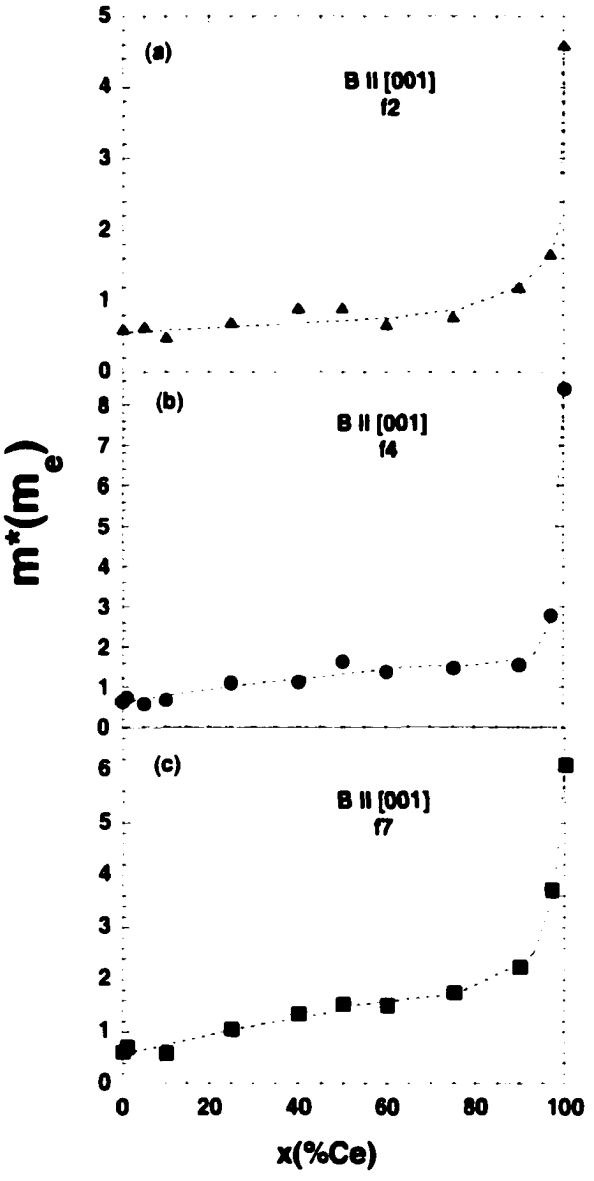

Figure 4.11 Concentration dependence of the effective masses for B || [001] a) for f2 b) for f4 c) for f7 orbits. The dotted lines are a guide for the eye. The value of effective masses for x=1 for f4 orbits was taken from Ref. [68].

Reproduced with permission of the copyright owner. Further reproduction prohibited without permission.

One theory of the concentration dependent mass enhancement is that due to Gor'kov and Kim [116]. The model of Gor'kov and Kim [116], which considers two impurity terms, appeared to explain a quadratic dependence in $Ce_xLa_{1-x}B_6$ over a limited range of x. However, this model cannot account for the non-monotonic dependence of m* on x observed in $Ce_xLa_{1-x}RhIn_5$ displayed in Figure 4.10 and 4.11.

4.3.5 Field Dependence of Effective Masses

In addition to concentration dependence of m*, the field dependence of effective masses was studied for two different frequencies. These results are shown in Figure 4.12 for B || [001]. As seen from this Figure, the effective masses of carries change as a function of the applied magnetic field. As an example, the change in mass for f7 orbit was recorded as 69% in the field ranging between 15T and 45T with x = 0.50. Because m* varies with field, we tried to restrict our analysis at a specified field range. Field dependent effective masses have been observed in a number of heavy fermion systems, including $CeRu_2Si_2$ [113], CeB_6 [117], and $CeCu_6$ [118]. In these compounds, it is observed that the values of effective masses decrease as the applied field increases and the change of m* is nearly a quadratic function of the applied field. A model describing the mass decrease with increasing field was discussed by Wasserman et al. [119]. Our results shown in Fig 4.12 show completely different field dependence for different concentrations of Ce unlike the previously reported [113, 117, 118]. In some cases, particularly at high magnetic fields, m* may actually increase with magnetic fields. To our knowledge, there is no theory that has discussed this type of result.

4.3.6 Measurement of the Dingle Temperatures

In 1952, Dingle [92] suggested that if electron scattering is taken into account, the Landau levels are broadened and this causes a reduction in the dHvA oscillation

Reproduced with permission of the copyright owner. Further reproduction prohibited without permission.

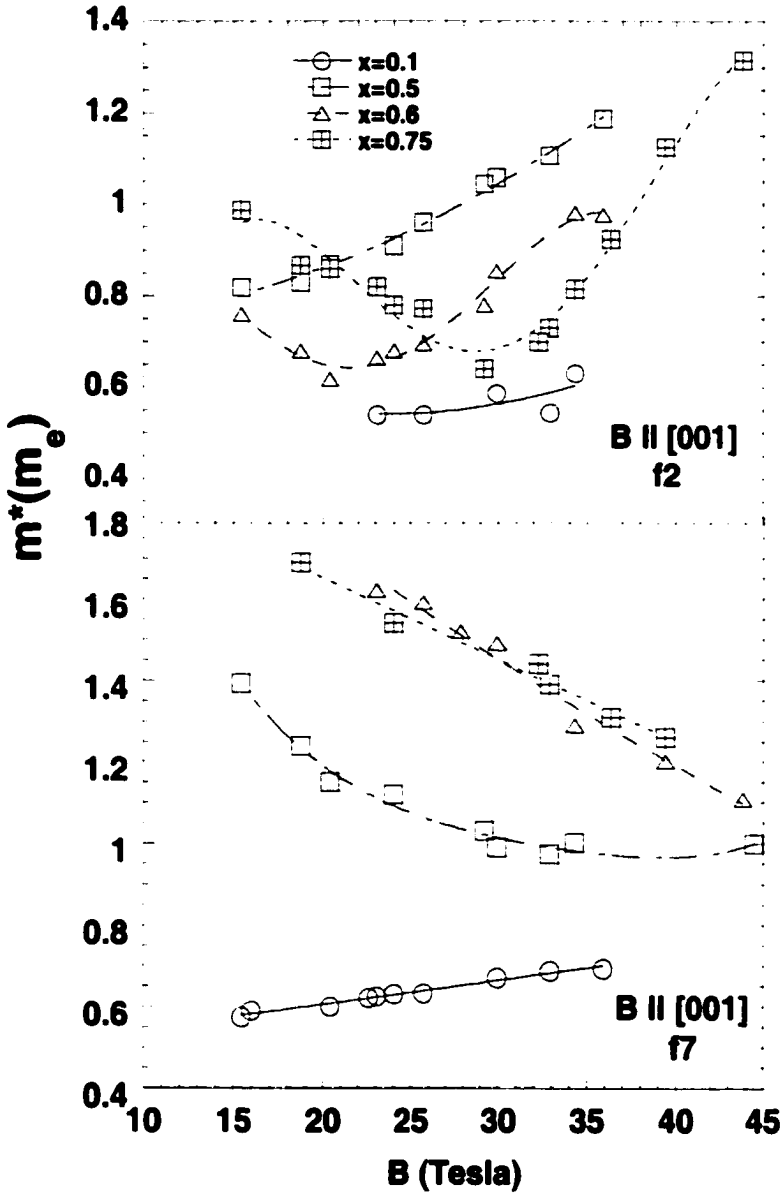

Figure 4.12 The field dependence of effective masses for f2 and f7 orbits at the selected concentration for B || [001].

Reproduced with permission of the copyright owner. Further reproduction prohibited without permission.

oscillation amplitude. This reduction in amplitude is known as the Dingle reduction factor R_D, and it is given by equation (3.14) as explained in the previous Chapter. This equation for p^{th} harmonic can also be expressed as

$$R_D = \exp(-\frac{apT_D}{H}), \tag{4.5}$$

where a=14.69 (m^*/m_0) Tesla/K, and T_D is the Dingle temperature which is related to the relaxation time τ, with $T_D = \hbar/2\pi k_B\tau$.

The field dependence of the amplitude A_p of the dHvA oscillation can be given as [25]

$$A_p = \frac{C_p T H^{-n} R_D}{\sinh(apT/H)}, \tag{4.6}$$

in this equation the values of C_p and n depend on particular methods of measurement. For example, n = 1/2 if the magnetization M is just measured like in the field modulation method and n = 5/2 if dM/dH is measured as in the pulse field method, however n =-1/2 if the torque method is used. The p dependence of C_p usually comes from the basic equation (3.10).

In order to determine the T_D from the field dependence of A_p, we made a plot of $\ln(A_pH^n\sinh(apT/H))$ against 1/H which should be linear with a slope of apT_D. This plot is known as the Dingle plot. Figure 4.13 shows the Dingle plots of $Ce_xLa_{1-x}RhIn_5$ compounds for several concentrations in pulsed field data for a f7 orbit. From the slopes of the straight lines, the values of the Dingle temperatures T_D were determined. As can be seen in the Fig.4.13, the change in Dingle temperature with concentration is small, especially at high concentrations. This result indicates that the arbitrary substitution of La by Ce contributes very little (or within the experimental uncertainty

Reproduced with permission of the copyright owner. Further reproduction prohibited without permission.

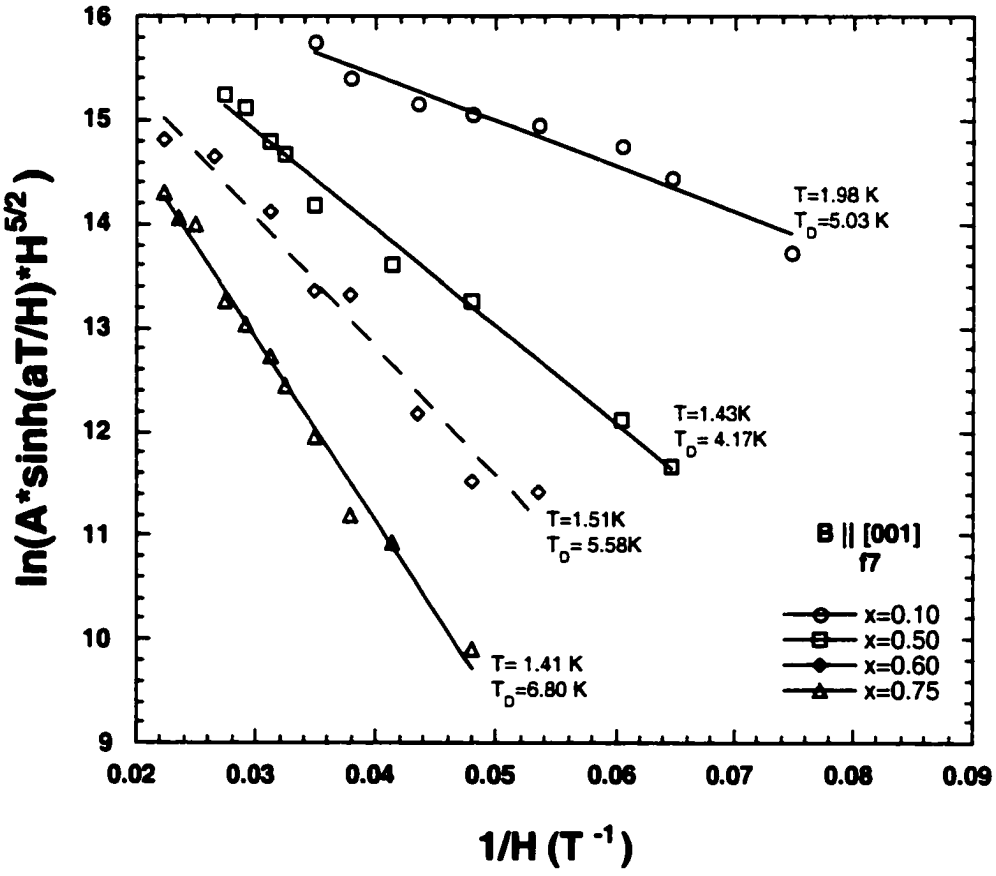

Figure 4.13 Dingle plot of $Ce_xLa_{1-x}RhIn_5$ compounds for f7 frequency. The Dingle temperatures T_D are determined from the slope of the straight lines.

Reproduced with permission of the copyright owner. Further reproduction prohibited without permission.

nothing) to the average quasiparticle scattering rate. Similar results were also observed in $Ce_xLa_{1-x}B_6$ alloys [120]. In order to estimate the sample quality, we measured the mean free path l which is related to the relaxation time τ by [120]

$$l = (\frac{2\hbar F}{eB^2})^{1/2} \frac{eB}{m^*}\tau \ , \tag{4.7}$$

or, in terms of TD, l can be written as

$$l = (\frac{e\hbar^3}{2\pi^2 k_B^2})^{1/2} \frac{F^{1/2}}{m^* T_D} \ , \tag{4.8}$$

where F is the measured dHvA frequency.

The Dingle temperatures and calculated mean free path l are given in Table 4.7. As seen from this table, the mean free path l seems to decrease with increasing Ce concentration. But, at high concentration (above x = 0.5) the measured values of l are very close to each other. That is, the substitution of La with Ce (or vice versa) does not contribute to the quasiparticle scattering rate.

Table 4.7 Dingle temperatures and free path for f7 orbits in $Ce_xLa_{1-x}RhIn_5$.

x	T_D(K)	l(Å)
0.10	5.03	2073
0.50	4.17	966
0.60	5.58	726
0.75	6.80	513

4.3.7 Spin Dependence of Carriers

The applied magnetic field lifts the spin degeneracy of the energy level and each energy level splits in two. The effect of this spliting is exactly equivalent to a phase difference ϕ between the oscillations coming from the spin-up and spin-down electrons.

Reproduced with permission of the copyright owner. Further reproduction prohibited without permission.

The spin interference factor, $R_S = \cos(p\pi gm^*/2m_e)$, causes the amplitudes of the harmonics of a given frequency to be modulated by a factor that depends on the effective mass m* and Lande g factor for a given orbit. When only one spin state contributes to the signal this reduction factor is not present and for pulsed field data, dM/dH, the amplitudes of the harmonics are proportional to $A_p/p^{1/2}$, where A_p is the amplitude of the p^{th} harmonic. In order to observe the spin dependence of carriers, we plot $\ln (A_p/p^{1/2})$ against harmonic numbers p over six Ce concentration for $Ce_xLa_{1-x}RhIn_5$ intermetallics where multiple harmonics were observed. As shown in Figure 4.14 for x = 0.5 and higher concentration the plot of $\ln (A_p/p^{1/2})$ against harmonic number p yields a straight line. This indicates that dHvA oscillations originate from only one spin direction because the spin splitting reduction factor is not present any longer. At x = 1 the plot is not linear and both spins contribute to the signal. This type of behavior recently was observed in $Ce_xLa_{1-x}B_6$ and the sign of the dominant spin channel was further found to be consistent with the model of Edwards and Green [120-122]. According to their model, the high magnetic field phase of heavy fermion systems is similar to that of the field induced ferromagnet. The spin-down electrons have effective masses that are more greatly enhanced by spin fluctuations and suffer from disorder scattering, causing them to no longer contribute to the dHvA signal [120-122]. In the present case, the 4*f* moments are only partially aligned in the range of measurement fields used.

Reproduced with permission of the copyright owner. Further reproduction prohibited without permission.

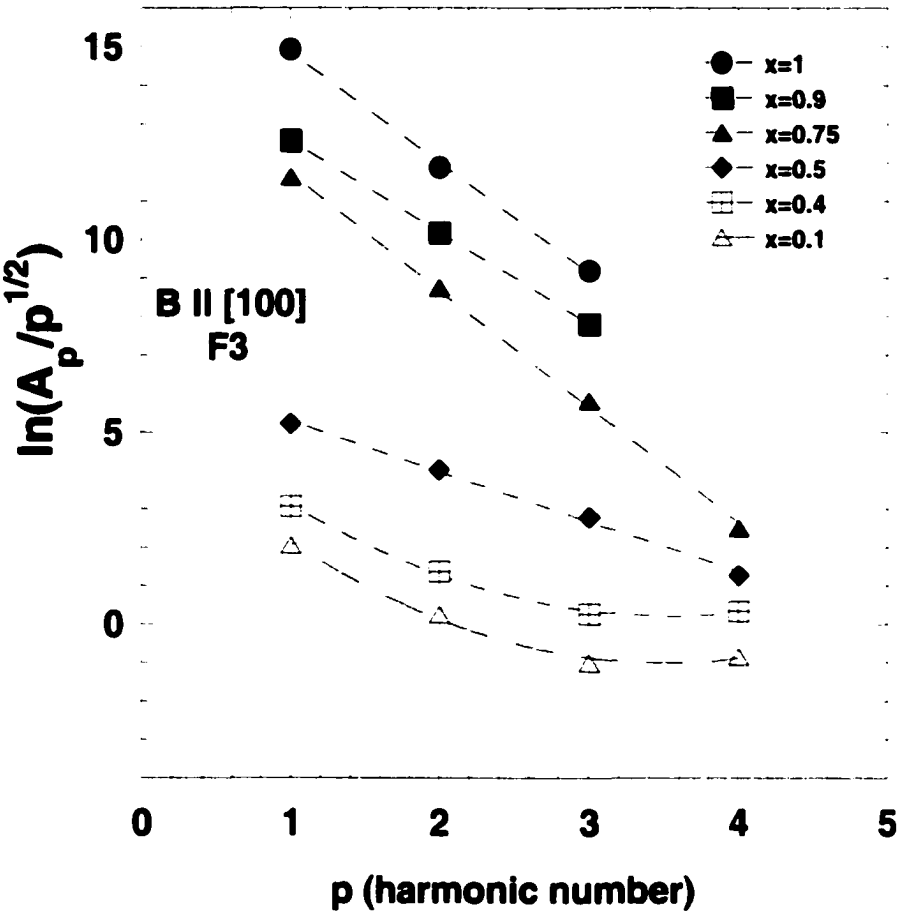

Figure 4.14 A plot of $\ln[A_p/p^{1/2}]$ versus harmonic index p for the F3 frequency, for which several harmonics could be observed. The dHvA signal is dominated by a single spin for $x \geq 0.5$, evidenced by the straight line.

Reproduced with permission of the copyright owner. Further reproduction prohibited without permission.

CHAPTER 5

DHVA MEASUREMENTS ON $Ce_xLa_{1-x}CoIn_5$

In this chapter, the result of the dHvA measurements on $Ce_xLa_{1-x}CoIn_5$ compounds will be reported. The measurements presented in this chapter were made at NHMFL, Los Alamos and Tallahassee by using the pulsed field and the torque method. The measurements were made on single crystals of $Ce_xLa_{1-x}CoIn_5$ with the field along the [001] and [100] direction, but along the [100] direction we could not observe any dHvA frequency. In addition, we also could not observe any dHvA frequency for x greater than 30%Ce with the field along [001] direction.

5.1 dHvA Measurements on $LaCoIn_5$

The measurements on metallic $LaCoIn_5$ was performed in the temperature range of 0.43 K to 4.53 K with magnetic fields up to 30 T by using the pulsed field method. The dHvA frequencies of $LaCoIn_5$ were determined by performing Fourier transforms. The dHvA signal and its corresponding Fourier transform for B || [001] are shown in Figure 5.1. As can be seen in Figure 5.1, for pure $LaCoIn_5$ nine fundamental frequencies, which are labeled f1 to f9, and their harmonics are observed for the field along the [001] direction. We observed that most of the measured frequencies in $LaCoIn_5$ is very close to measured frequencies in $LaRhIn_5$. This indicates that the Fermi surface of $LaCoIn_5$ are very similar to the Fermi surface of $LaRhIn_5$. The effective masses of carriers along this direction were determined from the temperature dependence of dHvA amplitudes as discussed in Chapter 4. The measured dHvA

Reproduced with permission of the copyright owner. Further reproduction prohibited without permission.

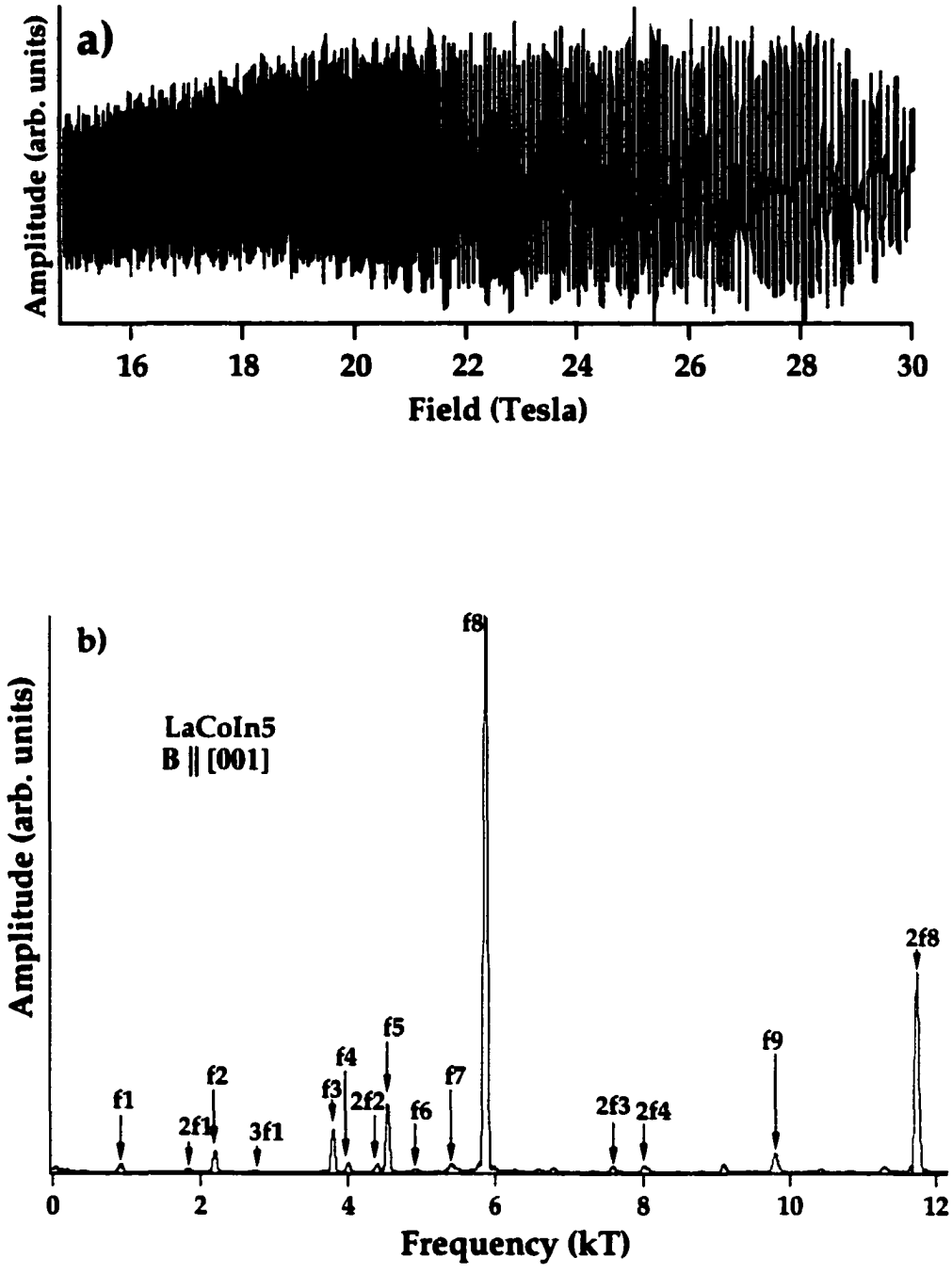

Figure 5.1 a) dHvA oscillation measured in pulsed field of $LaCoIn_5$ at 0.43 K b) Frourier transform of the signal shown in a).

Reproduced with permission of the copyright owner. Further reproduction prohibited without permission.

Table 5.1 Measured dHvA frequencies and effective masses for $LaCoIn_5$ with the field along [001].

Frequency (T)	Effective Masses
f1=910	0.022 ± 0.005
f2=2198	0.937 ± 0.005
f3=3796	0.603 ± 0.012
f4=4006	0.849 ± 0.012
f5=4544	0.995 ± 0.009
f6=4930	0.968 ± 0.045
f7=5405	1.044 ± 0.010
f8=5870	1.002 ± 0.012
f9=9792	

frequencies and effective masses are summarized in Table 5.1. As can be seen from Table 5.1, the values of effective masses vary between 0.022 and 1.044 m_0. Therefore, $LaCoIn_5$ is regarded as a light metal, not a heavy fermion.

5.2 dHvA Measurement on $CeCoIn_5$

As discussed in Chapter 2, $CeCoIn_5$ is a member of the recently discovered $CeMIn_5$ (M= Co, Rh, Ir) family. $CeCoIn_5$ is an ambient pressure heavy fermion superconductor at 2.3K [77]. This material, like the other family members, crystallizes in a tetragonal structure and consists of alternating layers of $CeIn_3$ (a heavy fermion antiferromagnet in which superconductivity can be induced with applied pressure [39]) and $CoIn_2$ stacked along the c-axis. In other words, $CeCoIn_5$ appears to be a quasi-two-dimensional (2D) variant of $CeIn_3$. Movshovic *et al.* [54] have shown a power law temperature dependence in the specific heat and thermal conductivity suggesting strongly that superconductivity in $CeCoIn_5$ is unconventional.

Reproduced with permission of the copyright owner. Further reproduction prohibited without permission.

The measurements reported here were carried out at the NHMFL, Tallahassee, FL using a rotating torque cantilever. The measurements were made at temperatures between 20 and 500mK in applied magnetic fields ranging from 5 to 18 Tesla. The sample used for this measurement was a single crystal of $CeCoIn_5$ and etched in a 25% HCI in H_2O solution to make a sample of appropriate size for the measurement. The sample was mounted on a cantilever with a GE varnish. Temperature dependent measurements of the dHvA amplitude and complete field rotations were made in the (100) and (001) planes of the tetragonal structure. As shown in Figure 5.2, the dHvA frequencies of $CeCoIn_5$ were determined by performing Fourier Transforms for the field along the [001] direction. In this direction, six fundamental and associated harmonics are observed. The fundamental frequencies are summarized in Table 5.2. As the field rotated away from the [001], the signals became stronger due to the larger values of $dF/d\theta$ away from the axis. The dHvA frequencies were measured for angles between [001] and [100] and between [001] and [110] as shown in Figure 5.3. Similar angular dependence of dHvA frequencies was observed by Onuki and Settai [123]. In addition, they have also reported the band structure calculation of $CeCoIn_5$ by assumption of the itinerant $4f$ electron. The effective masses of carriers for three orbits were determined for the field applied along the [111]. The observed frequencies and effective masses for the field along the [111] are summarized in Table 5.3. The effective masses couldn't be determined for the field [100] and [001] due to a near zero slope in the frequency vs. angle plots that causes very small signals and a rapidly diminishing signal with increasing temperature. Similar to $CeIrIn_5$ and $CeRhIn_5$, we observed $1/\cos(\theta)$ dependence, indicating the existence of a cylindrical Fermi surface, for the F_3, F_4 and

Reproduced with permission of the copyright owner. Further reproduction prohibited without permission.

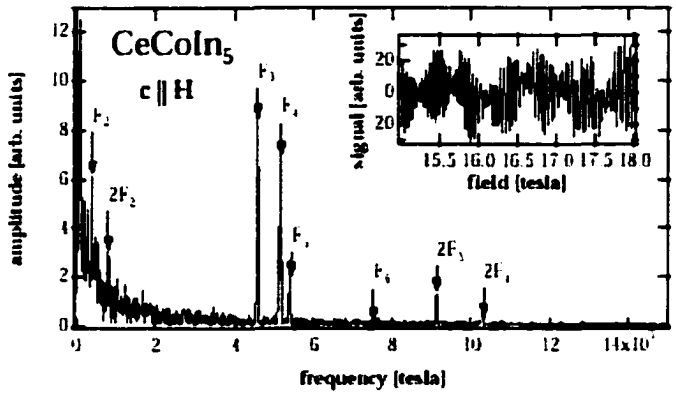

Figure 5.2 The Fourier transform of dHvA oscillations shown in the inset for the field along the c-axis. Both F_1 and F_6 are difficult to see in this Fourier transform. The amplitude of F_1 and F_6 grow with the increasing angle. (F_6 is observable at high fields.)

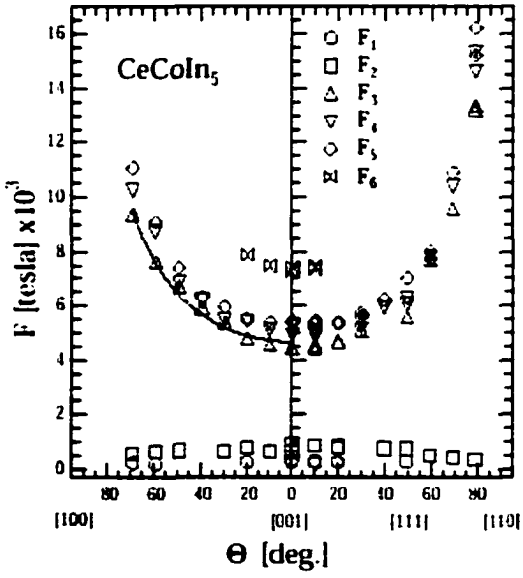

Figure 5.3 Angular dependence of the dHvA frequencies for $CeCoIn_5$.

Reproduced with permission of the copyright owner. Further reproduction prohibited without permission.

Table 5.2 Measured dHvA frequencies for $CeCoIn_5$ with the field along [001].

Symbol	Frequency (T)
F_6	7535
F_5	5401
F_4	5161
F_3	4566
F_2	411
F_1	267

Table 5.3 dHvA frequencies and measured effective masses for $CeCoIn_5$ with the field along [111].

Symbol	Frequency (T)	$m^*(m_e)$
F4	6064	20.3 ± 0.7
F3	5550	12.2 ± 0.2
F2	760	8.7 ± 2.2

F_5 branches. These three branches are closely spaced frequencies, corresponding to the extremal areas on an undulating cylinder. However, fewer frequencies are observed for $CeCoIn_5$ than for $CeRhIn_5$ [77] or $CeIrIn_5$ [79]. Some of the frequencies observed in the $CeRhIn_5$ and $CeIrIn_5$ are due to holes in the cylinders, and band structure calculations support this assignment. The cause of the reduced number of observed frequencies in $CeCoIn_5$ cannot be the very heavy carriers, because, based on heat capacity [56], the mass enhancement expected in all the members of the $CeMIn_5$ family is comparable. The cylindrical surface in $CeCoIn_5$ appears to be closed with no holes and much more two dimensional (2D)-like than in either of the other family members.

The existence of three closely spaced frequencies for the field applied along the [001] indicates that there are very small undulations on the cylinder in $CeCoIn_5$ when it

Reproduced with permission of the copyright owner. Further reproduction prohibited without permission.

is compared to the undulations on the cylinder in $CeRhIn_5$ and $CeIrIn_5$. In addition, the number of low frequencies in $CeCoIn_5$ is much smaller than either the Rh or Ir analogs so that there is a smaller number of electrons exhibiting 3D behavior. These results indicate that many transport properties and cooperative phenomena that are seen in $CeCoIn_5$ should be much more 2D in character than those found in either $CeRhIn_5$ or $CeIrIn_5$. The fact that the T_c in $CeCoIn_5$ is 5 times higher than that observed in $CeIrIn_5$ would suggest that the increasingly 2D-electronic structure has a direct correlation with enhanced T_c. Studies of the Fermi surface of $CeRhIn_5$ at pressures adequate to produce superconductivity would be valuable in confirming this supposition because the T_c of $CeRhIn_5$ under pressure is comparable to that of $CeCoIn_5$.

5.3 dHvA Measurements on $Ce_xLa_{1-x}CoIn_5$

Single crystalline samples of $Ce_xLa_{1-x}CoIn_5$, with x = 0.00, 0.01, 0.05, 0.10, 0.15, 0.20, 0.25, 0.30, 0.50 were used for the dHvA measurements. But dHvA signal could not be observed for x = 0.50. The measurements were carried out in the temperature range of 0.45 K to 9.5 K by using the pulsed field technique where the magnetic field reaches 50T in approximately 8 ms and falls to zero in 20-30 ms. All measurements reported here were made with the field along the [001] direction. We also have made the dHvA measurements with the field along the [100] direction for x=0.25, but we could not observe any frequency. All frequencies measured in $Ce_xLa_{1-x}CoIn_5$ were determined by performing the Fourier transform on the measured data set, and the effective masses of carriers were determined from the temperature dependence of the dHvA signal. The detailed explanation of frequency analysis and effective mass calculations are given in detail in Chapter 4. An example of the dHvA signal and its

Reproduced with permission of the copyright owner. Further reproduction prohibited without permission.

corresponding Fourier transform for x = 0.10 at 1.47 K is shown in Figure 5.4. for B || [001]. In this field direction, seven fundamental dHvA frequencies, f1, f3, f4, f5, f6, f7 and f8, were observed for all of the samples in the series. The measured fundamental frequencies and the effective masses of $Ce_xLa_{1-x}CoIn_5$ alloys for $0.00 \leq x \leq 0.30$ are summarized in Table 5.4.

5.3.1. Concentration Dependence of Frequencies

The concentration dependence of measured dHvA frequencies is given in Figure 5.5 for B || [001] with x = 0 being pure $LaCoIn_5$. The dotted lines included in the graph are just a guide for the eye. As seen in Figure 5.5, the frequencies increase in a continuous manner as the concentration x increases (except for f1 and f2 orbits not shown in Figure 5.5). For example, the change in frequency for f3 orbit is measured to be 2.11% up to x = 30%Ce. This increment in frequency indicates that the volume of the Fermi surface also increases with increasing Ce concentration. That is, the addition of 4*f* electrons to $LaCoIn_5$ changes the Fermi surface volume. Based on these results, the nature of the *f* electron in the $CeCoIn_5$ seems to be itinerant, even though we could not investigate the complete alloy series in all ranges from x = 0 to x = 1. The band structure calculation of $CeCoIn_5$ [123] also supports our itinerant 4*f* electron conclusion. In addition, it is seen that the measured frequencies of $Ce_xLa_{1-x}CoIn_5$ are very close to those of $Ce_xLa_{1-x}RhIn_5$. This result suggests that the shapes of Fermi surface of these two alloys seem to be very similar for $0.00 \leq x \leq 0.30$

5.3.2 Concentration Dependence of Effective Masses

It is observed that below 20 T the measured data is very noisy and the temperature dependence of the dHvA amplitude shows a deviation from the predicted

Reproduced with permission of the copyright owner. Further reproduction prohibited without permission.

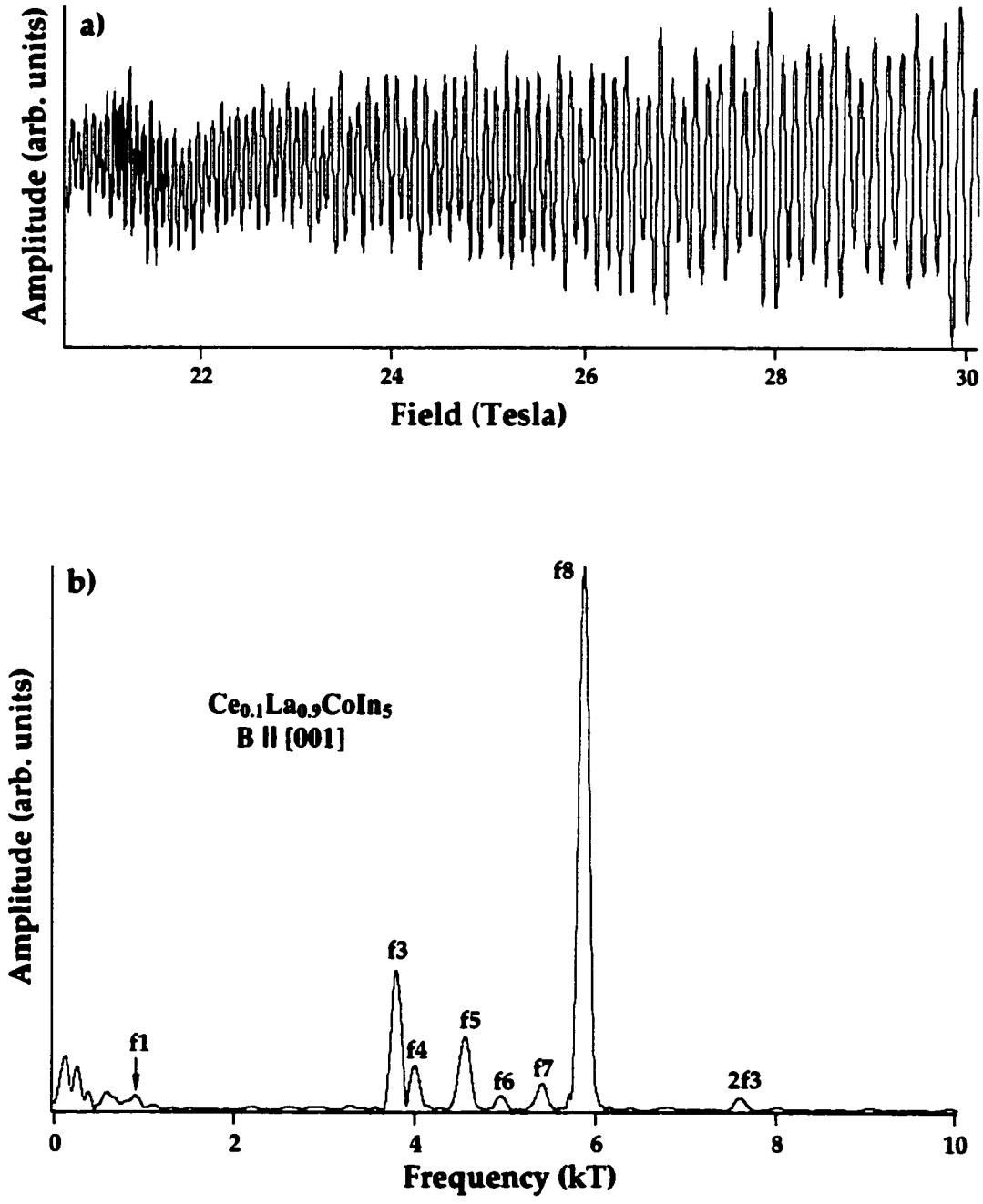

Figure 5.4 a) dHvA oscillation of pulsed field measurement for $Ce_{0.1}La_{0.9}CoIn_5$ at 1.47 K for B || [001] and its corresponding Fourier transform.

Reproduced with permission of the copyright owner. Further reproduction prohibited without permission.

Table 5.4 Measured dHvA Frequencies and effective masses for $Ce_xLa_{1-x}CoIn_5$ for B || [001].

x (%)	Frequency	Effective Mass	Field Range	Temp. Range
0	910	0.022 ± 0.005	15-30T	0.43-4.53K
	2198	0.937 ± 0.005		
	3796	0.603 ± 0.012		
	4006	0.849±0.012		
	4398	1.77±0.11		
	4544	0.995 ± 0.009		
	4930	0.968 ± 0.045		
	5405	1.044 ± 0.01		
	5870	1.002 ± 0.012		
	9792			
1	907		20-30	1.43-10.59K
	2175	0.925±0.0447		
	2740			
	3800	0.81±0.05		
	4011	1.02±0.06		
	4544	1.10±0.05		
	4938	1.02±0.03		
	5404	1.05±0.06		
	5879	1.15±0.01		
5	906		20-30	1.47-9.55K
	2143			
	3808	0.84±0.03		
	4025	1.15±0.04		
	4550	1.23±0.005		
	4806			
	4947	1.23±0.03		
	5398	1.19±0.06		
	5866	1.458±0.025		
10	910		20-30T	1.5-7.01K
	3811	0.95±0.06		
	4017	1.24±0.09		
	4570	1.45±0.076		
	4952	1.50±0.06		
	5419	1.50±0.02		
	5876	1.52±0.1		
15	3843	1.15±0.011	29-35T	0.5-6K
	4080	1.37±0.07		
	4569	1.61±0.1		
	4986	1.59±0.10		
	5440	1.56±0.08		
	5916	1.58±0.03		
20			20-30	0.5-3.5K
	3874	1.29±0.07		
	4621	1.70±0.2		
	5007			
	5430			
	5898	1.65±0.1		
25	3873	1.33±0.02	30-40T	0.44-4.51K
	4097	1.78±0.14		
	4559	1.902±0.05		
	5022	1.84±0.05		
	5475	1.79±0.05		
	5941	1.8±0.04		
30	3878		33-50T	0.5-2K
	4620			
	5017			
	5494			
	5951			

Reproduced with permission of the copyright owner. Further reproduction prohibited without permission.

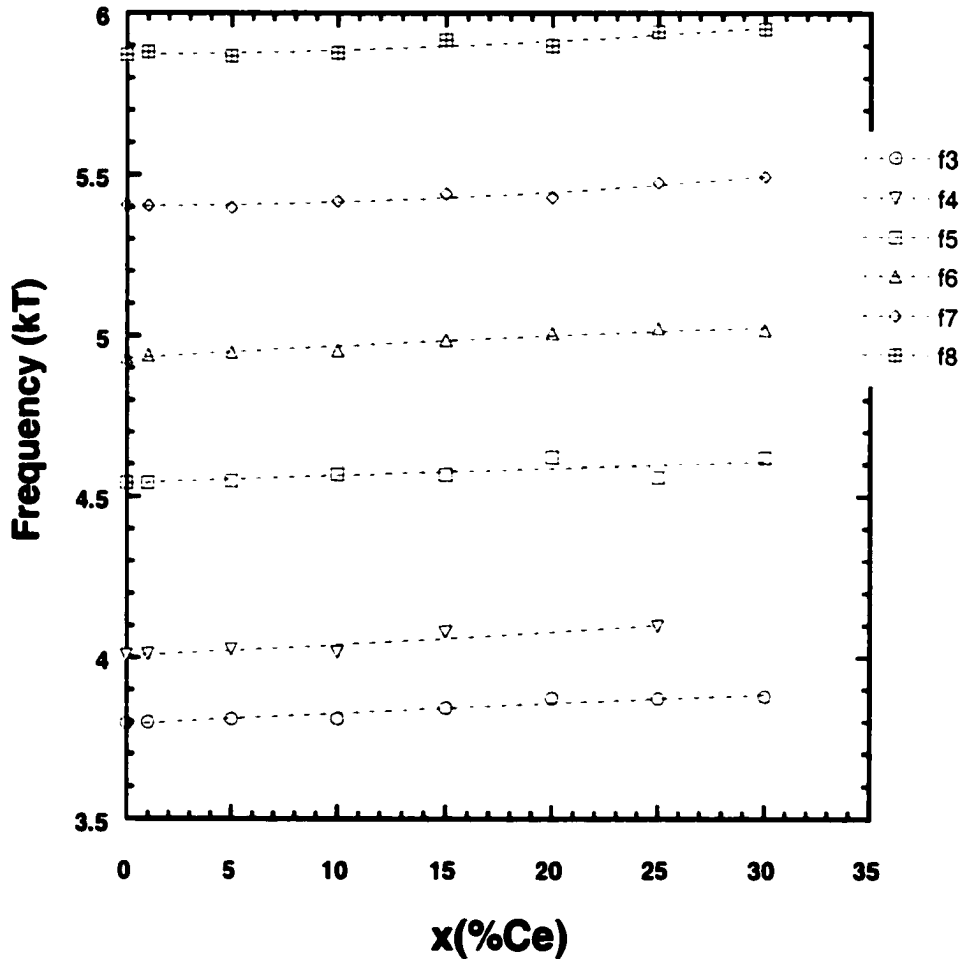

Figure 5.5 Concentration dependence of dHvA frequencies for $Ce_xLa_{1-x}CoIn_5$ with the field along [001] direction. The dotted lines are a guide for the eye.

Reproduced with permission of the copyright owner. Further reproduction prohibited without permission.

Liftshitz-Kosevich behavior. For that reason, the effective mass calculations of carriers were made in the field range 20-50 T. Similar to $Ce_xLa_{1-x}RhIn_5$, the field dependence of effective masses was studied for the frequencies f3, f5 and f7 and it was observed that there is no significant change in effective masses as a function of the applied magnetic field, even though some scattering was observed at low field and high field. Figure 5.6 shows the concentration dependence of effective masses for f2, f3, f4, f5, f6, f7 and f8 orbits with uncertainty in the calculation of effective masses. As can be seen in Figure 5.6, the effective masses of the carriers increases monotonically with increasing Ce concentration due to many body interaction. The solid lines are the curve fits to a quadratic form: $m^*=m_0(a+bx+cx^2)$ (where m_0 is the effective mass for $LaCoIn_5$ and x is the impurity concentration). Within experimental uncertainty, these fit lines (especially for f3, f4, f5 and f6) seem to be in good agreement with the theory presented by Gor'kov and Kim [116]. According to Gor'kov and Kim, if two impurity terms are considered, an additional x^2 correction term needs to be added to both the specific heat coefficient γ (proportional to m^*) and the magnetic susceptibility χ, as well as a linear x dependence.

5.3.3 The Dingle Temperature

The Dingle temperatures T_D (= $\hbar/2\pi k_B\tau$) are determined from the field dependence of the dHvA amplitude as explained in detail in Chapter 4. Figure 5.7 shows the Dingle plots of each sample for pulsed field data. The solid straight lines are the linear fit to the data. From the slopes of these straight lines, the Dingle temperatures T_D of the samples were calculated. T_D and m^*T_D are plotted against the concentration in Figure 5.8. As shown in Figure 5.8, the slope of the straight lines or the Dingle

Reproduced with permission of the copyright owner. Further reproduction prohibited without permission.

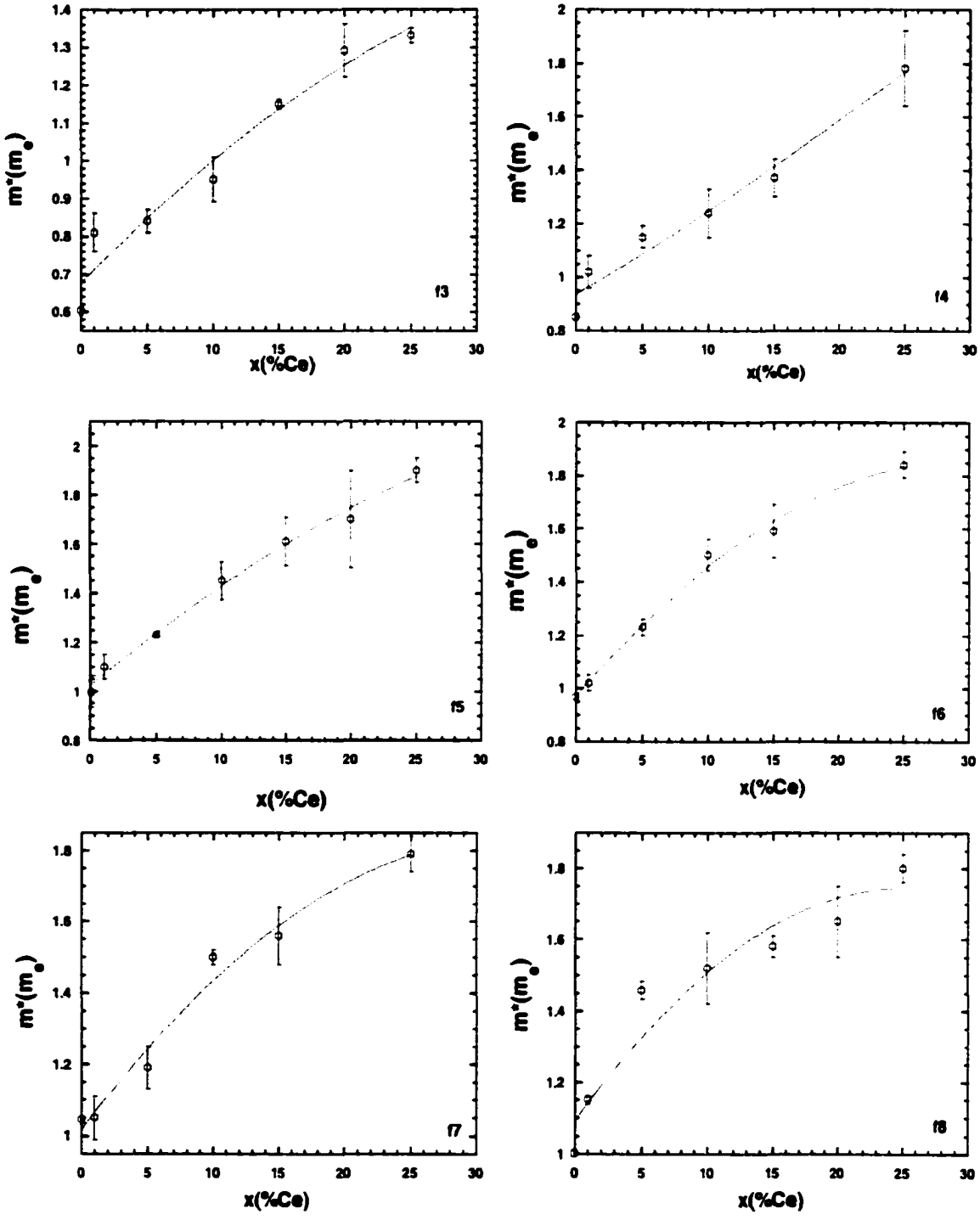

Figure 5.6 Concentration dependence of effective masses for $Ce_xLa_{1-x}CoIn_5$ with the field along the [001] direction. The solid lines represent the quadratic fit.

Reproduced with permission of the copyright owner. Further reproduction prohibited without permission.

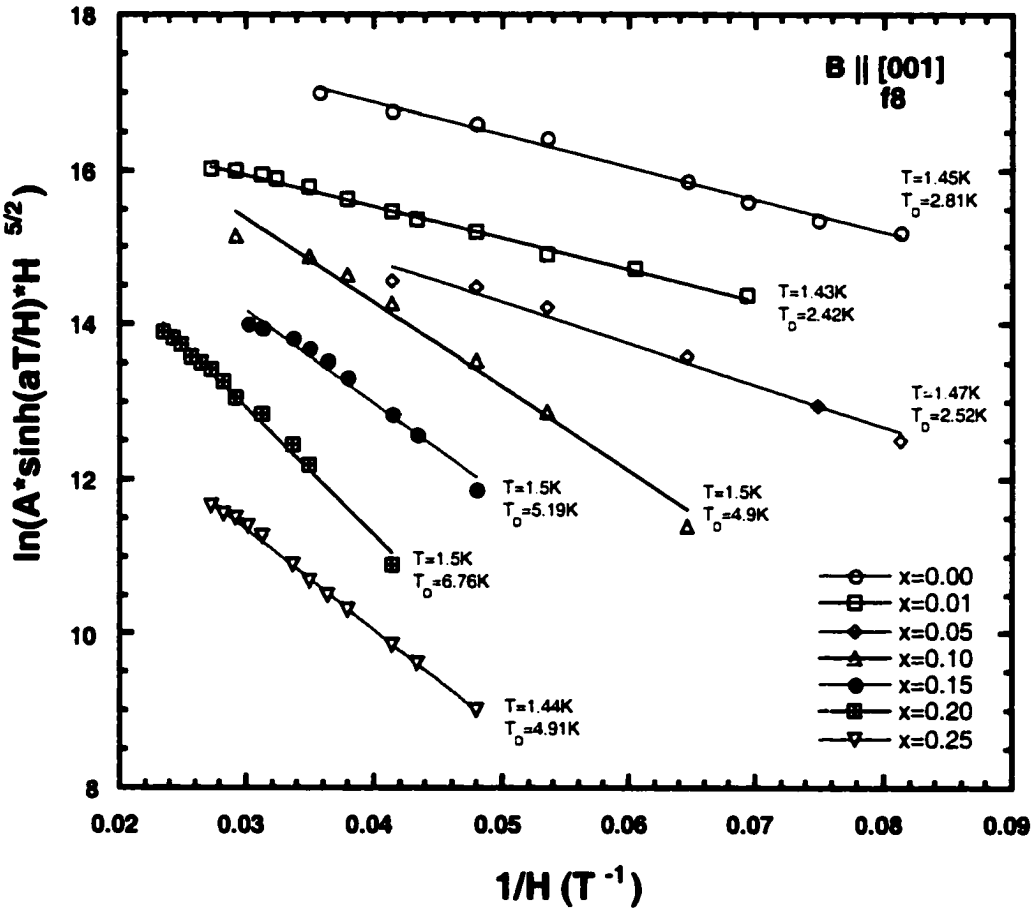

Figure 5.7 Dingle plot of some $Ce_xLa_{1-x}CoIn_5$ compounds for f8 frequency. The Dingle temperatures are determined from the slope of the straight lines.

Reproduced with permission of the copyright owner. Further reproduction prohibited without permission.

Table 5.5 Dingle temperatures and mean free path for f8 orbits in $Ce_xLa_{1-x}CoIn_5$.

x	T_D(K)	l (Å)
0.00	2.81	2121
0.01	2.42	2140
0.05	2.62	1619
0.10	4.90	799
0.15	5.19	728
0.20	6.76	534
0.25	4.91	677

temperature of samples changes with the Ce concentration . Unlike $Ce_xLa_{1-x}RhIn_5$ alloys, substitution of La by Ce seems to effect the quasiparticle scattering rate. In addition, the mean free path l for each sample is calculated by using equation 4.7. The Dingle temperatures T_D and the mean free path l for each sample are given in Table 5.5. As can be seen from this table, l also seems to depend on x at high concentrations.

5.3.4 Spin Dependence of Carriers

In the presence of high magnetic fields, if there are contributions to dHvA amplitude from both spin up and spin down electrons, these contributions appear in dHvA signal as spin reduction factor, $R_S = \cos(p\pi gm^*/2m_0)$. But, if only one spin state is contributing to the signal, this reduction factor is not present in the dHvA signal and then for pulse data the plot of $\ln(A_p/p^{1/2})$ against p (where A_p is the amplitude of the p^{th} harmonic) gives a straight line. In order to check the nature of the spin dependence of carriers, we made plots of $\ln(A_p/p^{1/2})$ vs. harmonic numbers p for the concentrations x =0.00, 0.01, 0.05 and 0.10. (We could not observe more than the second harmonic for the rest of the concentration.). As shown in Figure 5.8, we observe a nonlinear dependence of $\ln(A_p/p^{1/2})$ on p. In other words, we could not observe any single spin contribution to dHvA signal for the given concentrations.

Reproduced with permission of the copyright owner. Further reproduction prohibited without permission.

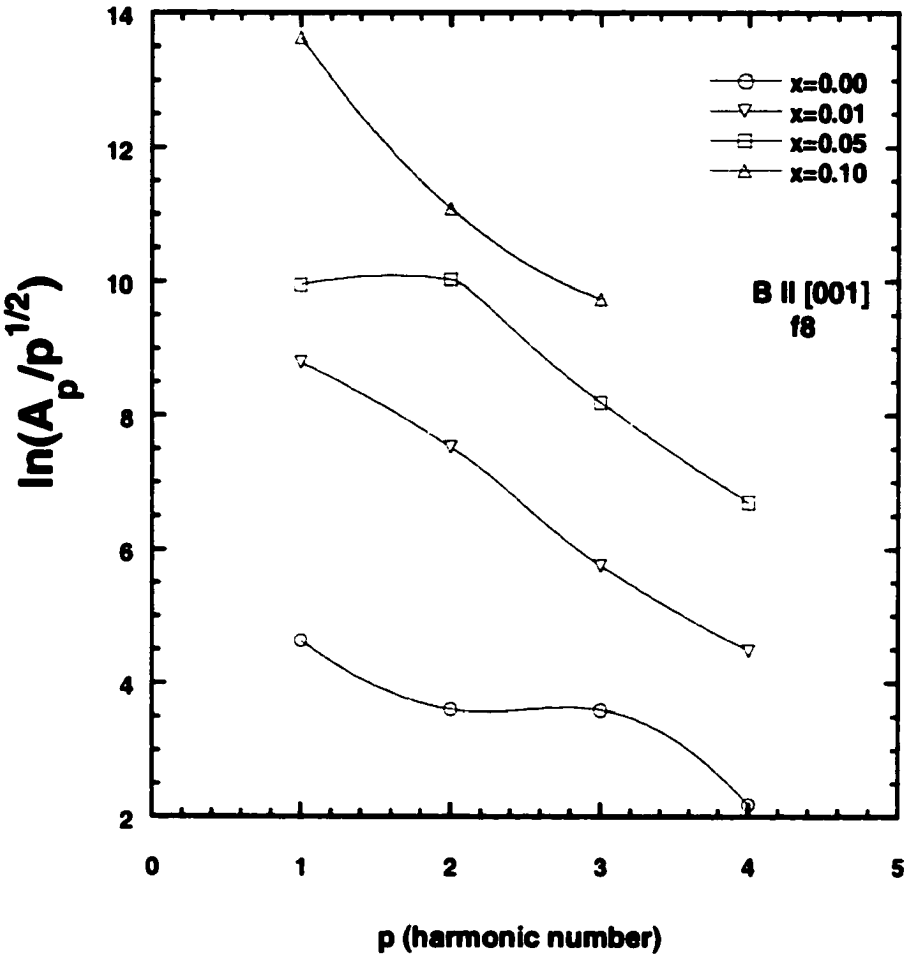

Figure 5.8 A plot of $\ln(A_p/p^{1/2})$ versus the harmonic number p for the f8 frequency.

Reproduced with permission of the copyright owner. Further reproduction prohibited without permission.

CHAPTER 6

DHVA MEASUREMENTS ON $Ce_xLa_{1-x}IrIn_5$

6.1 dHvA Measurement on $Ce_xLa_{1-x}IrIn_5$

Here and in the following section, the results of dHvA measurement in $Ce_xLa_{1-x}IrIn_5$ will be presented. All measurements reported in this chapter were made at NHMFL, Los Alamos by using the pulsed field technique in the temperature range between 0.49 and 9.5K. Similar to Rh and Co intermetalic compounds, the measurement on $Ce_xLa_{1-x}IrIn_5$ compounds were performed with the field along the [100] and [001] directions. The single crystals of $Ce_xLa_{1-x}IrIn_5$ compounds used in these measurements included: x = 0.03, 0.05, 0.10, 0.15, 0.20, 0.25, 0.30, 0.50 and 0.90. However, no dHvA signal was observed for $x \geq 0.30$.

DHvA frequencies of $Ce_xLa_{1-x}IrIn_5$ alloys were obtained by using the same method described in section 4.3.1. An example of the dHvA oscillations and its Fourier transform for x =0.03 for the field parallel to the [100] direction at 1.43 K is shown in Figure 6.1. In this field direction three peaks, F1, F2 and F3 were observed as the fundamental frequencies of dHvA oscillations. However, for the field along the [001] direction we observed 4 fundamental frequencies, f1, f2, f3 and f4, throughout the series. Figure 6.2 shows these frequencies and their oscillation signal for x = 0.10 at 0.49 K. Other than these frequencies, only for x = 0.03 a low frequency at 641 T and two high frequencies at 9696 and 14046 were observed, but they were not observed for the rest of samples as shown in Figure 6.2. The effective masses of the samples were

Reproduced with permission of the copyright owner. Further reproduction prohibited without permission.

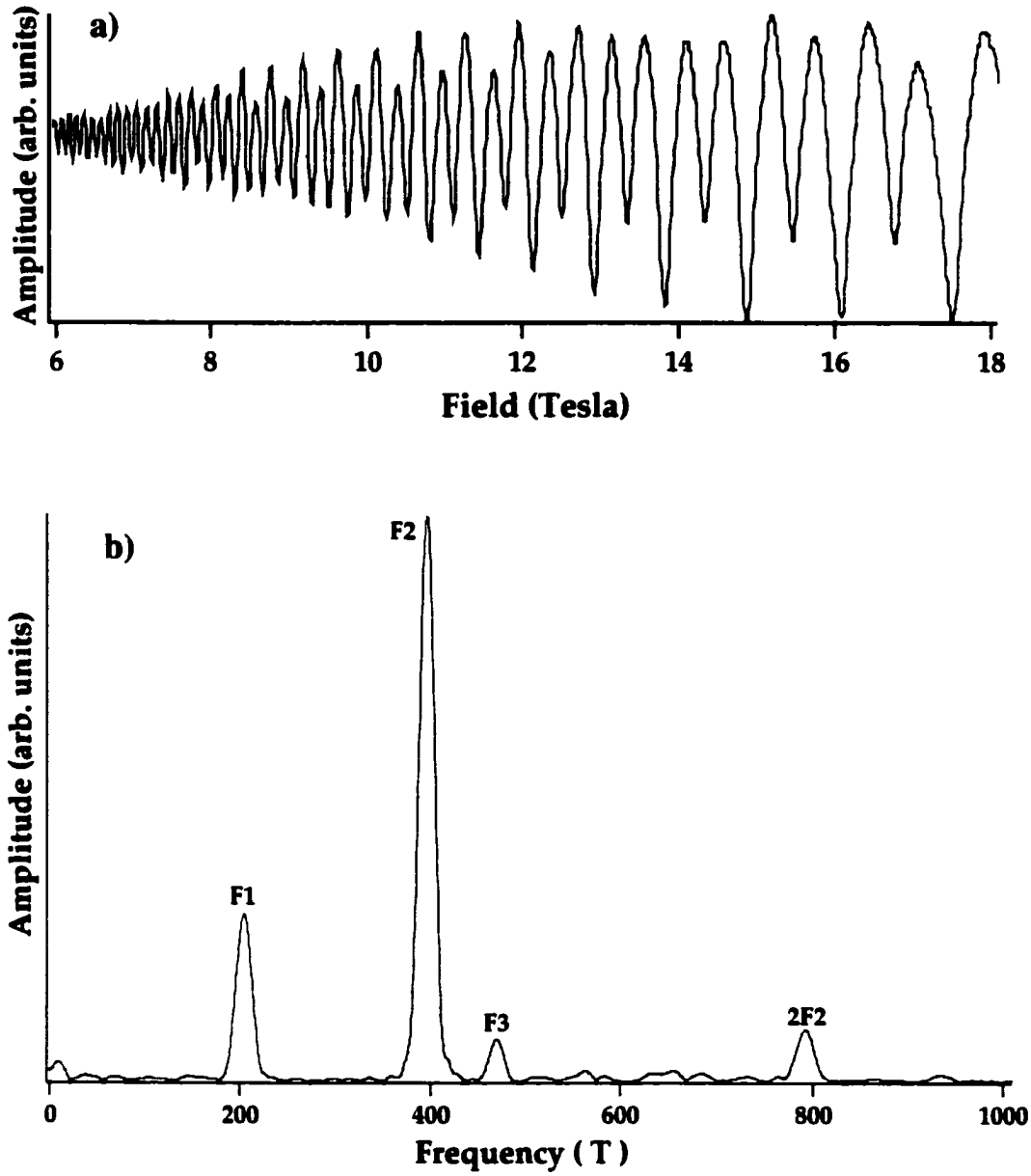

Figure 6.1 a) The pulsed field dHvA oscillation of the $Ce_{0.03}La_{0.97}IrIn_5$ sample at 1.43 K for B || [100] and b) its corresponding Fourier transform.

Reproduced with permission of the copyright owner. Further reproduction prohibited without permission.

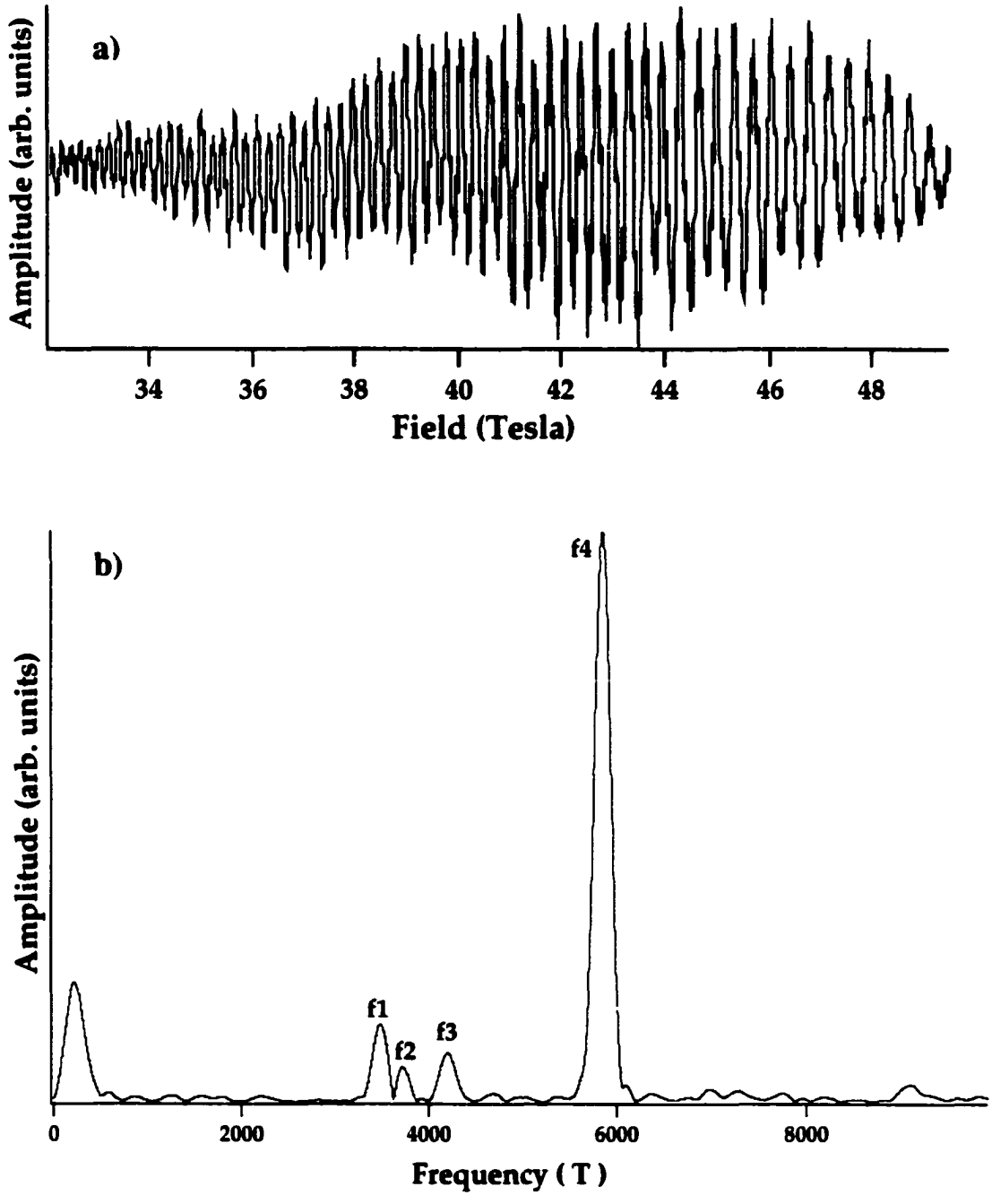

Figure 6.2 a) dHvA oscillations of pulsed field measurements for $Ce_{0.1}La_{0.9}IrIn_5$ at 0.49 K for B || [001] and b) its corresponding Fourier transform.

Reproduced with permission of the copyright owner. Further reproduction prohibited without permission.

obtained by using a temperature reduction factor in the Liftshitz-Kosevich formula as explained in section 4.3.3. The measured effective masses and frequencies are given in Table 6.1 for B || [100] and in Table 6.2 for B || [001] respectively.

6.2 Concentration Dependence of the Frequencies

The measured dHvA frequencies of the samples are plotted against Ce concentrations for both the field along the [100] and [001] direction as shown in Figure 6.3 a) and b) respectively. From Figure 6.3 a), we can see that even though frequencies F1 and F2 do not change with x, there is a noticeable change in the frequencies F3 and F4. Similarly, for B || [001] direction, within the experimental error, the frequencies increase with increasing x, as does the volume of the Fermi surface. For instance, the frequency increment for the f3 orbit was measured as about 4% for $0.03 \leq x \leq 0.25$. In addition, the dHvA frequencies reported by Haga *et al.* [79] on the CeIrIn5 seem to support the increment in frequency for $Ce_xLa_{1-x}IrIn_5$ samples. For example, the frequencies α_3, α_2, and β_2 measured by Haga *et al.* (see Table 2.3) seem to be extensions of frequencies f1, f2 and f4 measured in this study. These results state that the nature of the 4*f* electrons added to metallic LaIrIn5 must be itinerant. This itinerant picture of the 4f electrons in CeIrIn5 was also confirmed by the band structure calculation [79] as stated in section 2.4.1.

6.3 Concentration Dependence of Effective Masses

The temperature damping factor R_T in the Liftshitz-Kosevich formula was used to calculate the effective masses of quasiparticles as discussed in section 5.3.3. The plots of $m^*(m_e)$ against concentrations for f1, f2, f3 and f4 orbits are shown in Figure 6.4 for B || [001]. As can be seen from Figure 6.4, the error in effective mass

Reproduced with permission of the copyright owner. Further reproduction prohibited without permission.

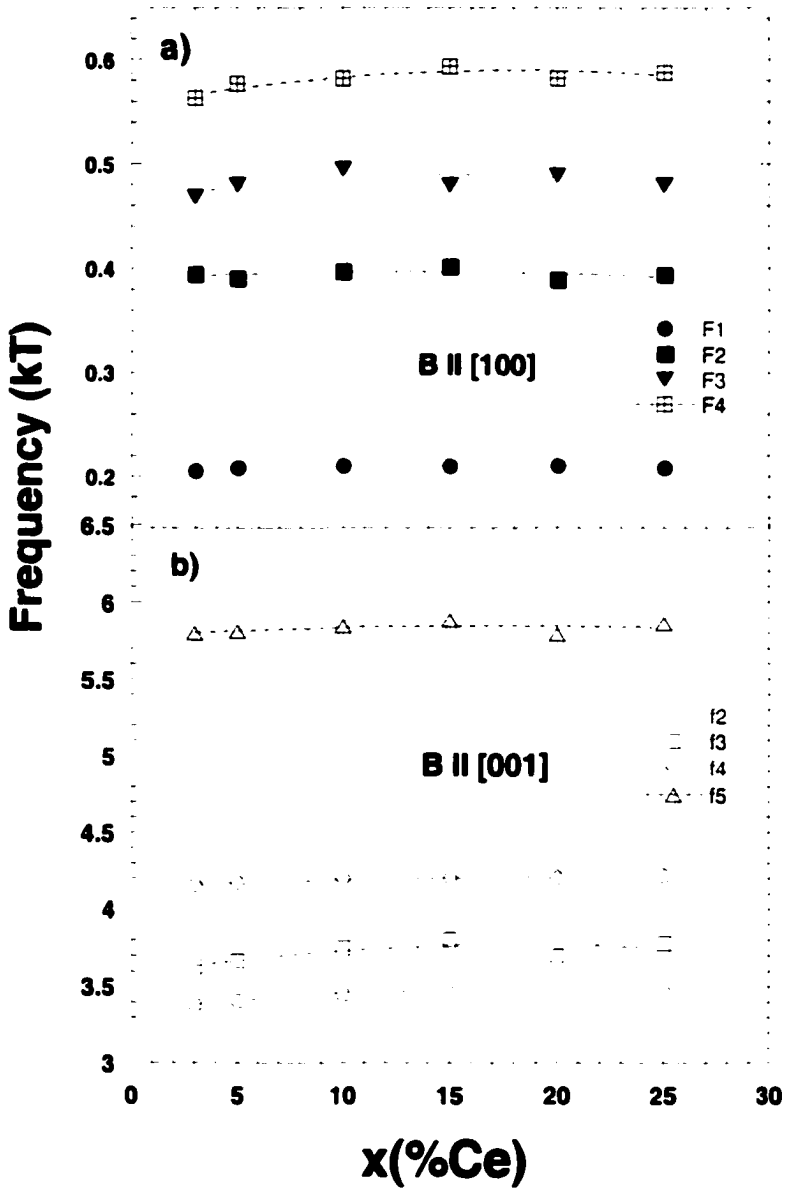

Figure 6.3 a) Concentration dependence of dHvA frequencies for B || [100] and b) for B || [001]. The dotted lines are a guide for the eye.

Reproduced with permission of the copyright owner. Further reproduction prohibited without permission.

measurements is very big, which indicates that the dHvA data is not in agreement with the temperature reduction factor R_T in the Liftshitz-Kosevich equation. The solid lines in Figure 6.4 represent quadratic fits to data. As can be seen from this figure, within the experimental uncertainties, the fits seem to be in agreement with the data, except for the f4 orbits. That is, the two impurity theory of Gor'kov and Kim [116] seems to be valid especially for low concentrations of $Ce_xLa_{1-x}IrIn_5$ compounds. The effective masses of carriers for B || [100] were able to be obtained only for x = 0.03, 0.05 and 0.10 samples. The frequencies, effective masses, and the worked field and temperature ranges for the data are shown in Table 6.1 for B || [001] and in Table 6.2 for B || [100].

6.4 The Dingle Temperature

The Dingle temperatures of $Ce_xLa_{1-x}IrIn_5$ samples for x = 0.03, 0.05, 0.10, 0.15 and 0.20 are shown in Figure 6.5 for the f4 orbit at 1.5 K. Unlike the $Ce_xLa_{1-x}RhIn_5$ and $Ce_xLa_{1-x}CoIn_5$ compounds, the Dingle temperatures T_D (or m^*T_D) in the $Ce_xLa_{1-x}IrIn_5$ compounds increase with increasing Ce concentration as shown in Figure 6.6. That is, the addition of the Ce impurities to $LaIrIn_5$ seems to reduce the dHvA amplitude very rapidly due to the increasing probability of electron scattering. In addition, we have also noticed that the Dingle temperatures observed in $Ce_xLa_{1-x}IrIn_5$ samples are much higher than those of $Ce_xLa_{1-x}RhIn_5$ and $Ce_xLa_{1-x}CoIn_5$ compounds. The reason for this might be the poor quality of the samples. The mean free paths l measured for given x are shown in Table 6.3. As seen from this table, as the result of the high Dingle temperatures, the measured l values for $Ce_xLa_{1-x}IrIn_5$ are smaller than the l values for $Ce_xLa_{1-x}RhIn_5$ and $Ce_xLa_{1-x}CoIn_5$.

Reproduced with permission of the copyright owner. Further reproduction prohibited without permission.

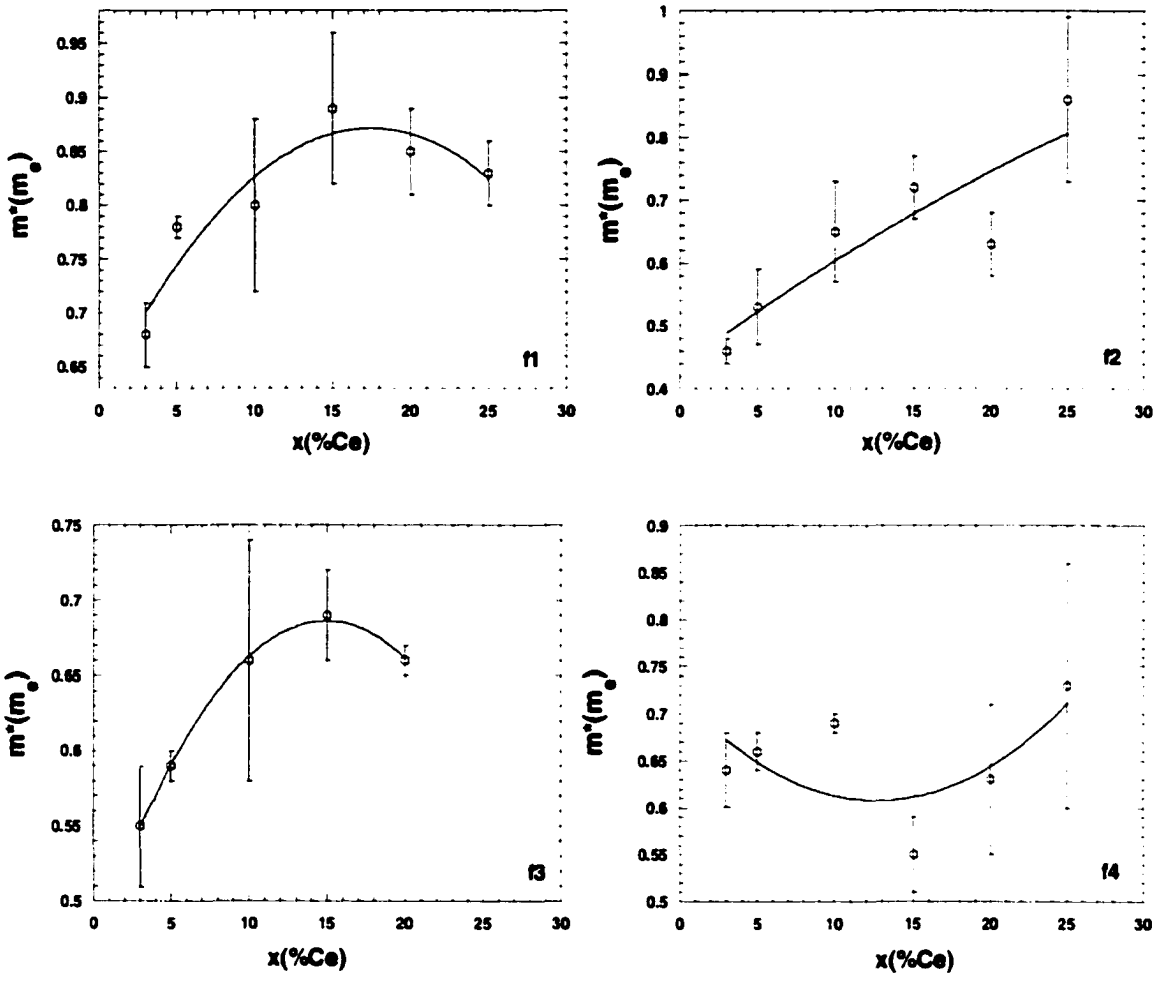

Figure 6.4 Concentration dependence of effective masses for $Ce_xLa_{1-x}IrIn_5$ for B || [001]. The solid lines are a quadratic fit to the data.

Reproduced with permission of the copyright owner. Further reproduction prohibited without permission.

Table 6.1 Measured dHvA frequencies and effective masses for $Ce_xLa_{1-x}IrIn_5$ with the field along the [001] direction.

x (%)	Frequency	Effective Mass	Field Range	Temp. Range
3	641		25-35T	1.46K-7.56K
	f1=3380	0.68±0.03		
	f2=3629	0.46±0.02		
	f3=4160	0.55±0.04		
	f4=5798	0.64±0.04		
	9696	1.04±0.03		
	14046	1.16±0.03		
5	3405	0.78±0.01	25-40T	0.49-5.5K
	3665	0.53±0.06		
	4175	0.59±0.01		
	5812	0.66±0.02		
10	3450	0.80±0.08	30-45T	0.49-7.5K
	3750	0.65±0.08		
	4198	0.66±0.08		
	5845	0.69±0.01		
15	3538	0.89±0.07	30-50T	1.44-9.49K
	3805	0.72±0.05		
	4205	0.69±0.03		
	5883	0.55±0.04		
20	3400	0.85±0.04	37-48T	1.54-7.5K
	3700	0.63±0.05		
	4207	0.66±0.01		
	5790	0.63±0.08		
25	3461	0.83±0.03	30-50T	0.43-4.51K
	3780	0.86±0.13		
	4216			
	5859	0.73±0.13		

Reproduced with permission of the copyright owner. Further reproduction prohibited without permission.

Table 6.2 Measured dHvA frequencies and effective masses for $Ce_xLa_{1-x}IrIn_5$ with the field along the [100] direction.

x (%)	Frequency	Effective Mass	Field Range	Temp. Range
3	205	0.21±0.004	6-18T	1.43-8.95
	395	0.13±0.003		
	469	0.21±0.04		
	563			
5	208	0.25±0.01	6-18T	1.58-10.05
	391	0.31±0.02		
	480			
	577			
10	210		6-18T	1.42-7.4
	397	0.28±0.04		
	495			
	582			
15	210		6-18T	1.44-7.47
	390			
	480			
	594			
20	210		6-18T	1.42-9.5
	402			
	489			
	582			
25	208		6-18T	0.43-11.49
	394			
	480			
	588			

Reproduced with permission of the copyright owner. Further reproduction prohibited without permission.

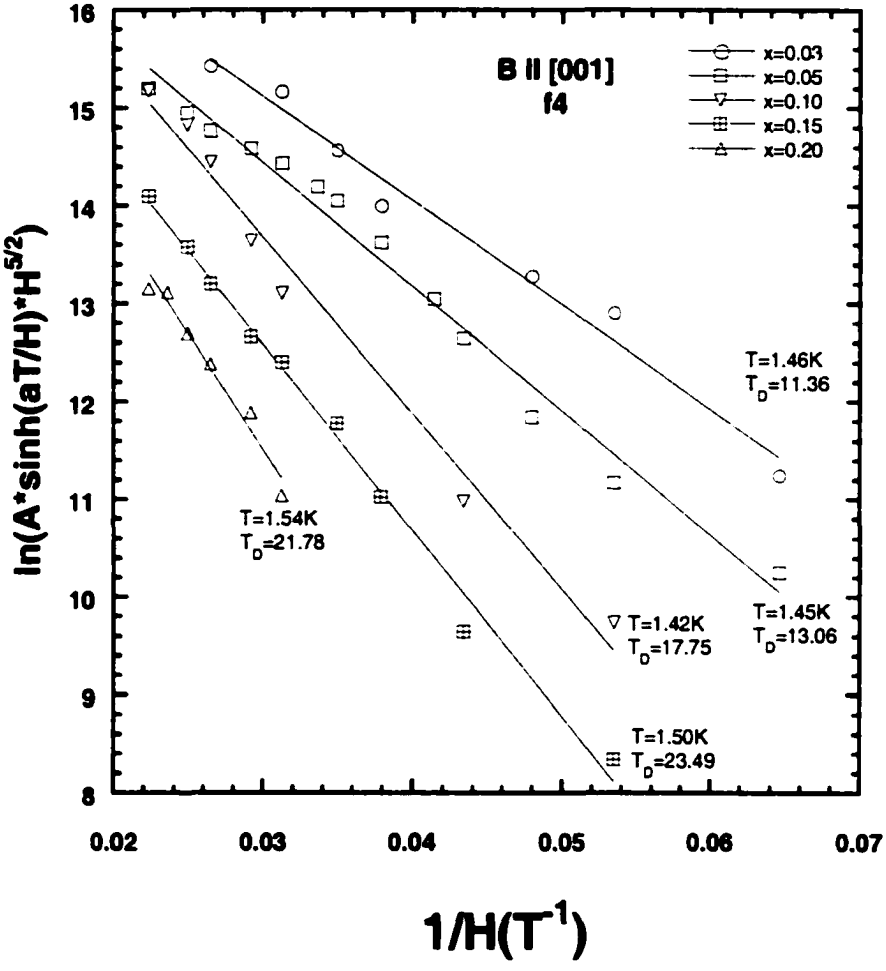

Figure 6.5 Dingle plot of $Ce_xLa_{1-x}IrIn_5$ compounds for f4 orbits for different concentrations.

Reproduced with permission of the copyright owner. Further reproduction prohibited without permission.

Table 6.3 Dingle temperatures and mean free path l for the f4 orbit in $Ce_xLa_{1-x}IrIn_5$.

x	T_D(K)	l (Å)
0.03	11.36	813
0.05	13.06	687
0.10	17.75	485
0.15	23.49	461
0.20	21.78	430

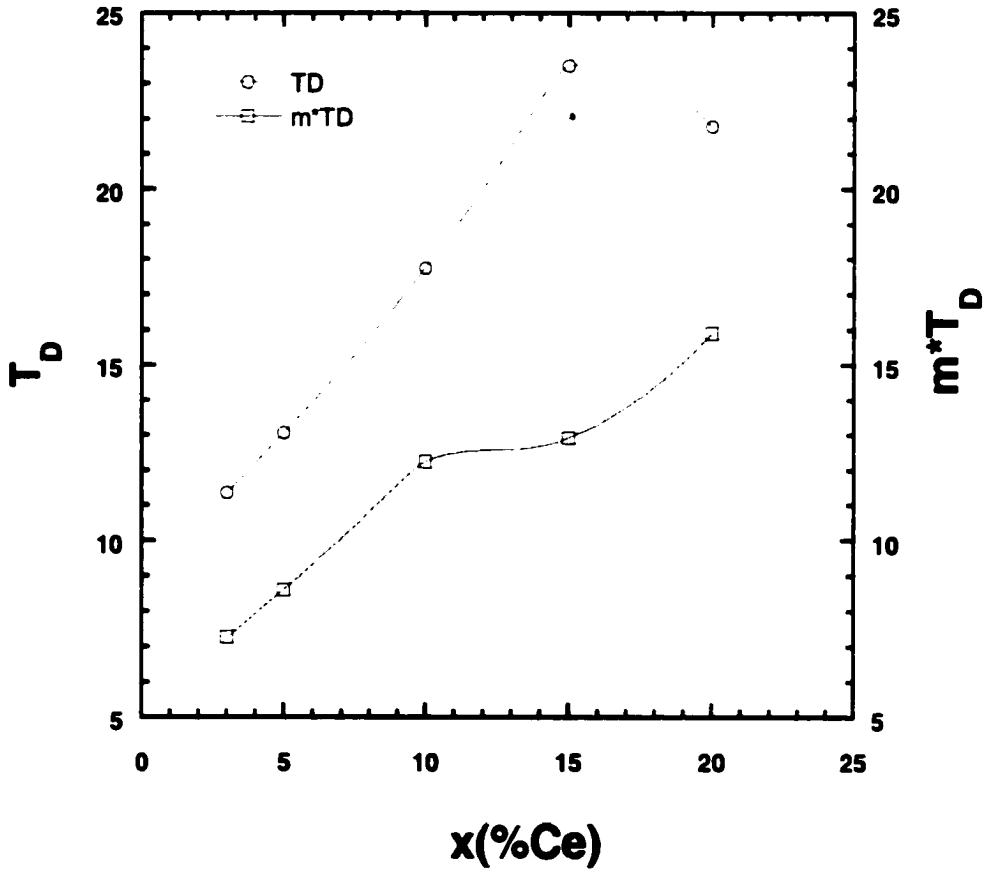

Figure 6.6 Plot of concentration dependence of Dingle temperature, T_D and m^*T_D for the f4 orbit.

Reproduced with permission of the copyright owner. Further reproduction prohibited without permission.

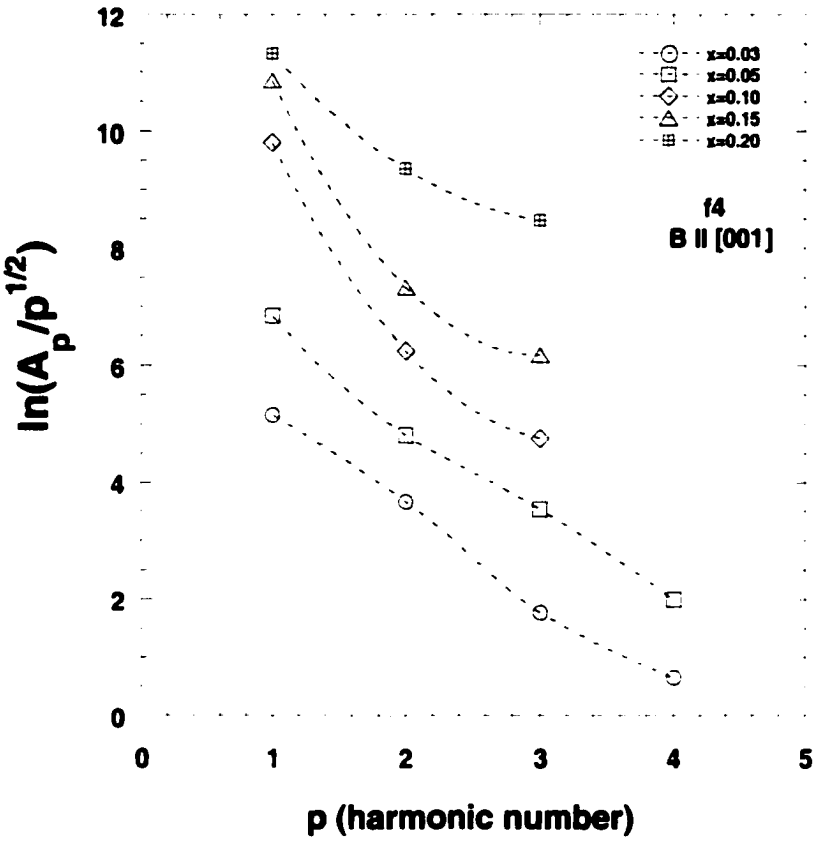

Figure 6.7 A plot of $\ln(A_p/p^{1/2})$ against the harmonic number p for the f4 orbit in $Ce_xLa_{1-x}IrIn_5$.

6.5 Spin Dependence of Carriers

The spin dependence of carriers is studied as described in section 4.3.7. As shown in Figure 6.7, the plot of $\ln(A_p/p^{1/2})$ against p (harmonic number) exhibits a nonlinear behavior for the alloys of $Ce_xLa_{1-x}IrIn_5$. That is, the measurements on these alloys do not reveal the existence of any single spin channel dependence at low concentrations.

Reproduced with permission of the copyright owner. Further reproduction prohibited without permission.

CHAPTER 7

SUMMARY AND CONCLUSIONS

We have performed a detailed de Haas van Alphen (dHvA) study on the $Ce_xLa_{1-x}MIn_5$ (M = Rh, Co, Ir) alloys to investigate the topology of the Fermi surface from the metallic $LaMIn_5$ to the heavy fermion $CeMIn_5$.

In the first chapter of this dissertation, the theory of electrons in metals is discussed. The heavy fermion materials which exhibit very large effective masses at low temperatures are presented in the second chapter. Then the $CeMIn_5$ (M = Rh, Co, Ir) compounds are introduced as newly discovered heavy fermion superconductors. Among these materials, $CeCoIn_5$ and $CeIrIn_5$ exhibit superconductivity at ambient pressure with T_c = 2.3K and T_c = 0.4K respectively, whereas $CeRhIn_5$ orders antiferromagnetically at 3.8 K at ambient pressure. The interest in these materials comes from the fact that they appear to be quasi-two dimensional variants of $CeIn_3$ which is an ambient-pressure antiferromagnet .

The dHvA effect, the measurement of the oscillatory part of the magnetization, and measurement techniques are presented in a qualitative fashion in the third chapter. The Lifshitz-Kosevich equation is outlined as a general theory of the dHvA effect. In this study, single crystals of $Ce_xLa_{1-x}MIn_5$ with various compositions were used and the dHvA magnetization measurements were made with three different techniques at two different laboratories. Both the torque method and the field modulation method were carried out at National High Magnetic Field Laboratory (NHMFL), Tallahassee, FL.

Reproduced with permission of the copyright owner. Further reproduction prohibited without permission.

The pulsed field technique was performed at NHMFL, Los Alamos, NM. The details are given in the relevant section of this dissertation.

The results of dHvA measurements on $Ce_xLa_{1-x}RhIn_5$ were presented in Chapter 4. The dHvA frequencies of the spin unpolarized metallic $LaRhIn_5$ with low effective masses (less than free electron masses) were investigated for the field along the [100] and [001] directions. In addition, similar to $LaRhIn_5$, the results of dHvA measurements of heavy fermion $CeRhIn_5$ with the energy-band calculations were presented. But it is observed that the band structure calculations and the dHvA measurements of frequencies do not agree with each other (especially for the [001] direction). Then the results of dHvA measurement of $Ce_xLa_{1-x}RhIn_5$ compounds with various doping levels were outlined. From the concentration dependence of frequencies, it was demonstrated that there is no change in the measured frequencies throughout the series. That is, the addition of a $4f$ electron into $LaRhIn_5$ does not change the Fermi surface. Moreover, this result shows that the $4f$ electron in Ce atom is localized, not delocalized as suggested by the band calculations. From the temperature dependence of dHvA amplitudes, the effective masses of the carriers as a function of Ce concentration were reported. It was demonstrated that the effective mass increases slightly at low concentration and remains nearly constant until concentration $x = 0.75$. For $x = 0.90$ and above, the enhancement is increased dramatically. However, the x dependence of effective masses is not in agreement with Gor'kov and Kim's theory [116]. The Dingle temperature measurements on $Ce_xLa_{1-x}RhIn_5$ showed that Ce impurities do not to contribute to the electron scattering rate. Furthermore, the field dependence of cyclotron masses was studied and it was seen that the application of

Reproduced with permission of the copyright owner. Further reproduction prohibited without permission.

magnetic field changes the effective masses, but these mass changes were not uniform over the concentration ranges. In addition, it was observed that for x = 0.50 and higher concentrations, the dHvA oscillations originate from only one spin direction.

In Chapter 5, the results of the dHvA experiments on CeCoIn5 and $Ce_xLa_{1-x}CoIn_5$ (for x = 0.00, 0.01, 0.05, 0.10, 0.15, 0.20, 0.25, 0.30) were described for the B || [001] direction. No dHvA signal has been seen above x = 0.30. From the angular dependence of the measurements it was observed that many the transport properties of $CeCoIn_5$ originate much more from its two dimensional character than those found in either $CeRhIn_5$ or $CeIrIn_5$. Unlike the $Ce_xLa_{1-x}RhIn_5$, dHvA measurements on $Ce_xLa_{1-x}CoIn_5$ reveal that the Fermi surface changes significantly with increasing Ce concentration, x. This result is in agreement with the 4*f*-itenerant band model [123]. In addition, it is observed that the effective masses of carriers increase with x. This enhancement of the effective masses with concentration x is also in good agreement with the existing theory of the magnetic impurity interaction [116]. Moreover, from the Dingle temperature results it is concluded that addition of impurities (Ce ions) increases the electron scattering rate. The spin dependence studies show that there is no single spin dependence to the dHvA signal below x = 0.10.

Finally, the results of the dHvA measurement on $Ce_xLa_{1-x}IrIn_5$ are presented for both B || [001] and [100] directions in Chapter 6. We have only been able to observe dHvA signals for the sample x = 0.03, 0.05, 0.10, 0.15, 0.20 and 0.25. The concentration dependence of frequencies showed that the volume of the Fermi surface increases with increasing Ce concentration for both field directions. Therefore, it has been concluded that the 4*f* electrons in Ce atom are itinerant, as suggested by the band

Reproduced with permission of the copyright owner. Further reproduction prohibited without permission.

theory calculations [79]. Similar to $Ce_xLa_{1-x}CoIn_5$ case, the effective masses of $Ce_xLa_{1-x}IrIn_5$ showed an enhancement with x and this enhancement seems to be in agreement with the theory of magnetic impurity. The increment in Dingle temperature with x suggests that substitution of La by Ce increases the electron scattering rate. Spin dependence studies have concluded that both spin up and spin down electrons contribute to the dHvA signal for below x = 0.20.

Overall, the results of the dHvA measurements on $Ce_xLa_{1-x}MIn_5$ family show that;

i)Several pieces of the Fermi surface of $Ce_xLa_{1-x}MIn_5$ seem to be similar to each other.

ii) The itinerant 4f electron picture of band structure calculations is in agreement with experiments for M = Co, Ir and in disagreement for M = Rh.

iii) The measured effective masses of all the family are increasing with increasing Ce concentration. The enhancement in the mass for Co and Ir is in agreement with the existing theory.

iv) The replacement of La by Ce contributes to the electron scattering rate for M = Co and Ir not for M = Rh.

v) for each of the series, there is no single spin dependence below 10 % Ce. However, x = 0.5 and higher concentration measurements on Rh series show that dHvA oscillations originate from only one spin direction.

Reproduced with permission of the copyright owner. Further reproduction prohibited without permission.

REFERENCES

1. Drude P., *Annalen der Physik* **1**, 566 and **3**, 369 (1900)

2. Lorentz, H., *Proc. Amsterdam Acad.*, **7**, 438, 585, 684 (1905)

3. Pauli W. *Z. Physik* **31**, 765 (1925)

4. Fermi E., *Z. Phys.*, **36**, 902 (1926)

5. Dirac P. A., *Proc. Roy. Soc. A*, **112**, 661 (1926)

6. Ashcroft N. W. and Mermin N. M., *Solid State Physics.*, Saunders College Publishing, Orlando, FL, (1976)

7. Pauli, W., *Z. Phys.* **41**, 81 (1927)

8. Sommerfeld A, *Z. Physik*, **47**, 1 (1928)

9. Cracknel, A. P., Wong , K. C., *The Fermi Surface*, Clarendon Press, Oxford, (1973)

10. Kittel C., *Introduction to Solid State Physics*, sixth ed. John Wiley & Sons, Inc. New York, (1986)

11. Ziman, J. M., *Theory of Solids*, second ed., Cambridge University press, (1972)

12. Alanso J. A., March N. H., *Electrons in Metals and Alloys*, Academic Press, New York, (1989)

13. Mc Kelvey, J. P., *Solid State and Semiconductor Physics*, Harper and Row Publisher, New York (1966)

14. Brown C. F., *The Physics of Solids*, W. A. Benjamin, Inc. New York, NY (1967)

15. Whittaker E.T. and Watson G.N., *Modern Analysis*, third ed., p. 412 Macmillan, New York (1946).

16. Smith R. A, *Wave Mechanics of Crystalline Solids*, Chapman and Hall, London, p. 39 (1961)

17. Kronig R. L. and Penney W. S., *Proc. Roy. Soc.* **A130**, 499 (1930)

18. Brillouin L., *Wave Propagation in Periodic Structures*, Dover publications, New York, (1953)

Reproduced with permission of the copyright owner. Further reproduction prohibited without permission.

19. Mc Coll D. and Simpson O. C., *AEC Research and Development Report ANL-6647*, Argonne National Laboratory, November (1962)

20. London H. *Proc. Roy. Soc. A*, **176**, 522 (1940)

21. Pippard A.B. *Phil. Trans. A*, **250**, 325:104,105 (1957)

22. Wash W. M., *Solid State Physics*, Vol. 1, edited by J. F. Cochran and R. R. Hearing, Gordan and Breach, New York (1969)

23. Chambers, R.G. *The Fermi Surface*, ed. Harrison and Webb, Willey, New York (1960)

24. Pippard A.B., *Dynamics of Conduction Electrons*, Gordon & Breach New York (1965)

25. Shoenberg D, *Magnetic Oscillations in Metals*, Cambridge University Press, Cambridge, (1984)

26. Hummel R. E., *Electronic Properties of Materials*, second ed. Springer-Verlag New York (1993)

27. Burns, G., *Solid State Physics*, Academic Press, New York, (1985)

28. Landau L., *Soviet Physics JETP* **3**, 920 (1957)

29. Andres K., Graeber J. E., Ott H. R., *Phys. Rev. Lett.* **35**, 1779 (1975)

30. For reviews, see Fisk Z., Ott H. R., Rice T. M., Smith J. L., *Nature (London)* **320**, 124 (1986); Ott H. R. and Fisk Z., *Handbook of Physics and Chemistry of the Actinides*, A.J. Freeman and G.H. Lander, Eds. (North Holland, Amsterdam) (1988); Stewart G.R., *Rev. Mod. Phys.* **56**, 755 (1984); Lee P. A, Rice T. M., Serene J. M., Sham L.J., Wilkins J. M., *Comments Condensed Matter Physics* **12**, 99 (1986)

31. Ott H. R., Rudiger H., Felder E, Fisk Z., Batloog B., *Phys. Rev. Lett.* **55**, 1595 (1985)

32. Palstra T.T.M., *et al., ibid*, p. 2727; Maple M.B. *et al., ibid* **56**, 185 (1986)

33. Ott H.R., Rudiger H., Delsing P., Fisk Z, *Phys. Rev. Lett.* **52**, 1551 (1984)

34. Fisk Z., Stewart G. R., Willis J. O., Ott H. R., Hulliger F., *Phys. Rev. B* **30**, 6360 (1984)

35. Ott H. R, Rudiger H., Fisk Z., Smith J. L., *Phys. Rev. Lett* **50**, 1595 (1983)

Reproduced with permission of the copyright owner. Further reproduction prohibited without permission.

36. Smith J.L., Fisk Z., Willis J. O., Batlogg B., Ott H. R., *J. Appl. Phys.* **55**, 1996 (1984)

37. Fujita T., Satoh K, Onuki Y., Komatsubara T., *J. Magn. Magn. Mater.* **47-48**, 66 (1985)

38. Moshovich R., Graf T., Mandrus D., Thompson J.D., Smith J. L., and Fisk Z. *Phys. Rev. B* **53**, 8241 (1996)

39. Mathur N. D., Grosche F. M., Julian S. R., Walker I. R.. Freye D. M., Haselwinner R.K.W and Lonzarich G. G., *Nature* **394**, 39 (1998)

40. H. Hegger, C. Petrovic, E.G. Moshopoulou, M.F. Hundley, J.L. Sarrao, Z. Fisk and J.D. Thompson, *Phys. Rev. Lett.* **84**, 4986 (2000)

41. Ruderman M. A., and Kittel C., *Phys. Rev.* **96**, 99 (1954)

42. Kasuya T., *Prog. Theo. Phys. Japan* **16**, 45 (1956)

43. Yosida K, *Phys. Rev.* **106**, 893 (1957)

44. Kondo J., *Prog. Theo. Phys.* **32**, 37 (1964); and Kondo J., *Solid State Phys.* **23**, 184 (1969)

45. Steglich F., Aarts J., Bredl C. D., Lieke W., Meschede D., Franz W. and Schafer H., *et al. Phys. Rev. Lett.* **43**, 1892 (1979).

46. Springford M., *Physica B* **171**, 151 (1991)

47. Bucher E., Maita J. P., Hull G. W., Fulton R. C., and Cooper A. S., *Phys. Rev. B* **11**, 440 (1975)

48. Abe H., Kitizawa H., and Aoki H., *J. Phys. Soc. Jpn.* **67**, 1852 (1998)

49. Trovarelli O., Geibel C., Cardoso R., Mederle S., Borth R., Busshinger B., Grosche F.M., Grin Y., and Steglich F., *Phys. Rev. B* **61**, 9467 (2000)

50. Amsler B., Fisk Z., Sarrao J. L., Molnar S. V., Meisel M. W. and Sharifi F., *Phys. Rev. B* **57**, 8747 (1998).

51. Bredl C. D., *J. Magn. Magn. Mater.* **63-64**, 355 (1987).

52. Walker I. R., Grosche F. M., Julian S.R., Freye D. M., and Lonzarich G. G, *Physica B* **282-287**, 303 (1997).

Reproduced with permission of the copyright owner. Further reproduction prohibited without permission.

53. Cornelius A. L., Pagliuso P.G., Hundley M. F., and Sarrao J. L., *Phys Rev. B* **64** 144411 (2001)

54. Movshovich R, Jaime M., Thompson J. D., Petrovic C., Fisk Z., Pagliuso P. G. and J.L.Sarrao, *Phys. Rev. Lett.* **86**, 5152 (2001).

55. Petrovic C, Pagliuso P.G., Hundley M. F., Movshovich R., Sarrao J.L., Fisk Z., Monthoux P. *Journal of Physics-Condensed Matter* **13**, L337 (2001)

56. Petrovic C., Movshovich R., Jaime M., Pagliuso P. G., Hundley M. F., Sarrao J. L., Fisk Z., and Thompson J.D, *Europhysics Letters* **53**, 354 (2001)

57. Hurd C.M., Electrons In Metals, John Willey & Sons, Inc. New York, p. 187, (1975).

58. Doniach S., in R.D. Park (Ed.), *Valance Instabilities and Related Narrow Band Phenomena*, Plenum, New York, (1977).

59. Sato K., Fujita T., Maeno Y., Onuki Y., Komatsubara T., *J. Phys. Soc. Japan* **58**, 1012 (1989).

60. Besnus M.J., Kappler J.P., Lehman P., Meyer A., *Solid State Commun.* **55**, 779 (1985).

61. Andrake B, Kim J. S., Srewart G. R., Fisk Z., *Phys. Rev. B*, **44**, 4371 (1991)

62. Satoh K, Fujita T., Maeno Y., Onuki Y., Komatsbara T., and Ohtsuka T., *Solid State Commun.* **56**, 327 (1985)

63. Sullow S. Ludoph B., Nieuwenhuys G. J., Menovsky A. A., and Mydosh J. A., *Physica B*, 223-224, 208 (1996)

64. Stewart G.R., Z. Fisk, J. L.Smith, J.O. Willis and M.S Wire, *Phys. Rev. B* **30**, 1249 (1984)

65. Stewart G.R., Z. Fisk, J.O. Willis and J.L. Smith, *Phys. Rev. Lett.* **52** 679 (1984)

66. Cornelius A. L., Arko A. J., Sarrao J. L., and Harrisson N. Phys. Rev. B, 59, 13542 (1999)

67. Cornelius A. L., A.J. Arko, J.L. Sarrao, M. F. Hundley and Z. Fisk *Phys. Rev. B* **62**, 14181 (2000)

68. Cornelius A.L. *private communication.*

Reproduced with permission of the copyright owner. Further reproduction prohibited without permission.

69. J. D Thompson, R. Movshovic, Z. Fisk, F. Bouquet, N. J. Curro, R.A Fisher, P.C. Hammel, H. Hegger, M. F. Hundley, M. Jaime, P.G. Pagliuso, C. Petrovic, N. E. Phillips, and J.L. Sarrao, *J. Magn. Magn. Mater.* **226** 5 (2001).

70. Bardeen J., Cooper L. N., and Schrieffer J. R., *Phys Rev.* **108**, 1175 (1957)

71. Osheroff, D. D., Gully W. J., Richardson R.C., Lee D.M., *Phys. Rev. Lett.* **29**, 920 (1972)

72. Jaccard D., Behnia K., and Sierro J., *Phys. Rev. A* **163**, 475 (1992)

73. Grosche F.M., Mathur S. R. J. N. D. and Lonzarich G. G., *Physica (Amsterdam)* **224B**, 50 (1996)

74. Taillefer L., Flouquet J., and Lonzarich G.G., *Physica B* **169**, 257 (1991)

75. Grewe N. and Steglich F. Handbook on the Physics and Chemistry of Rare Earth eds. K.A. Gschneider Jr., and L. Eyring 14, p.343 Amsterdam-North Holland.

76. Fulde P. *Ann. Phys.* **9**, 871 (2000).

77. Hall D.,E. Palm, T. Murphy, S. Tozer, Eliza Miller Ricci, Lydia Peabody, CharisQuay Huei Li, U. Alver, R.G. Goodrich, J.L. Sarrao, P.G. Pagliuso, J.M. Wills and Z. Fisk. *Phys. Rev. B* **64**, 64506 (2001)

78. Moshopoulou E.G., Fisk Z., Sarrao J. L., and Thompson J. D., *Journal of Solid State Chemistry*, **158**, 25 (2001)

79. Haga Y., Inada Y., Harima H., Oikawa K., Murakawa M., Nakawaki H., Tokiwa Y., Aoki D., Shishido H., Ikeda S., Watanabe N., and Onuki Y. *Phys. Rev. B* **63**, 060503 (2001)

80. Takeuchi T., Inoue T., Sugiyama K., Aoki D., Tokiwa Y., Haga Y., Kindo K., and Onuki Y., *Journal of the Physical Soceity of Japan* **70**, 877 (2001)

81. Murphy T. P., Hall Donavan, Palm E.C., Tozer S.W., Fisk Z., Goodrich R.G., Pagliuso P, G., Sarrao J.L, Thompson J. D., (unpublished)

82. Wei Bao, P.G. Pagliuso, J.L. Sarrao, J.D. Thompson, Z. Fisk, J.M. Lynn, and R.W. Ervin, *Phys. Rev. B*, **62**, R14621 (2000)

83. Hall D.W., *et al.* to be published.

84. Goodrich R. G., *et al.* to be published.

85. Landau, L. *Z. Phys.*, **64**, 629 (1930)

Reproduced with permission of the copyright owner. Further reproduction prohibited without permission.

86. de Haas W.J., and van Alphen P.M., *Proc. Netherlands Roy. Acad. Sci.* **33,** 1106 (1930)

87. Peieirls R., *Z. Phys.*, **81**,186 (1933)

88. Blackman M., *Proc. Roy. Soc.* A **166**, 1 (1938)

89. Shoenberg D., *Proc. Roy. Soc.* A **170,** 341 (1939)

90. Marcus J. A. Phys. Rev. 71, 559 (1947)

91. L. Onsanger, *Phil. Mag.*, **43**, 1006 (1952)

92. Dingle R. B., *Proc. Roy. Soc.* A **211**, 517 (1952)

93. Lifshitz,I.M. and Kosevich,A.M. *Dokl. Akad. Nauk. SSR* **96,** 963 (1954)

94. Priestly M. G., *Phil. Mag.* **5**, 111 (1960)

95. Cohen M. H., and Falicov L. M., *Phys. Rev. Lett.* **7**, 231 (1961)

96. Blount E. I., Phys. Rev. 126, 1636 (1962)

97. Shoenberg D., *Phil. Trans. Roy. Soc. A* **255**, 85 (1962)

98. Lifshitz,I.M. and Kosevich,A.M, *Sov. Phys. JETP* **2**, 636 (1956)

99. Shoenberg D., *Magnetic Oscillations in Metals*. Cambridge University Press, Cambridge, 1984

100. Gold A. V., in J.F. Cochrane and R. R. Haering (eds.), *Electrons in Metals* Gordon and Breach, New York 1968

101. Reinders P.H.P., Springford M., Coleridge P.T., Boulet R., and Ravot D. J., *Phys. Rev. Lett.* **57**, 1631 (1986)

102. Luttinger J.M., *Phys. Rev.* **121**, 1251 (1961)

103. Bychkov Yu. A. and Gorkov L.P. *Sov. Phys. JETP* **14**, 1132 (1962).

104. Fowler M. and Prange R. E. *Physics* **1**, 315 (1965).

105. Engelsberg S., and Simpson G., *Phys. Rev. B* **2**, 1657 (1970).

106. Wasserman A., Springford M., *Adv. in Phys.* **45**, 471 (1996)

Reproduced with permission of the copyright owner. Further reproduction prohibited without permission.

107. Shoenberg D., *Physica* **19,** 791 (1953)

108. Brooks J. S., Naughton M. J., Ma Y. P, Chaikin P. M. and Chamberlin R. V., *Rev. Sci. Inst.* **58**, 117 (1987)

109. Shoenberg D., *Phil. Trans. Roy. Soc. London*, **245**, 1 (1952)

110. Haanappel E. G., Hedderich R., Joss W., Askenazy S., and Fisk Z., *Physica B* **177**. 181 (1992)

111. Goodrich R.G. *et al.*(to be published)

112. Harrison N., Balicas L., Teklu A. A., Goodrich R. G., Brooks J. S., Cooley J. C., and Smith J. L., *Phys. Rev. B* **63**, 081101(R) (2001).

113. Aoki H., Uji S., Albessard A.K., ank Onuki Y., *Phys. Rev. Lett.* **71**, 2110 (1993).

114. Springford M., and Reinders P. H. P., *J. Mag. Mag. Mat.* **76-77**, 11 (1988).

115. Hunt M., Meeson P., Probst P.-A., Rienders P., Springford M., Assmus W., and Sun W., *J. Phys.: Condens. Mat.* **2**, 6859 (1990).

116. Gor'kov L.P., and Kim J. H., *Phys. Rev. B* **51,** 3970 (1995)

117. Joss W., Vanruitenbeek J.M., Crabtree G. W., Tholence J.L., Vandeursen A.P.J. and Fisk Z. *Phys. Rev. Lett.* **59**, 1609 (1987)

118. Chapman S. B., Hunt M., Meeson P., Springford M., *Physica B* **163**, 361 (1990)

119. A. Wasserman, M. Springford and F. Han, *J. Phys.: Condens. Matter* **1**, 2669 (1988)

120. R. G. Goodrich, N. Harrison, A Teklu, D. Young and Z. Fisk, *Phys. Rev. Lett.* **82**, 3669 (1999)

121. Teklu A. A., Goodrich R.G., Harrison N., Hall D., Fisk Z., and Young D., *Phys. Rev. B* **62,** 12875 (2000).

122. Edwards D. M., and Green A.C.M., *Z. Phys. B* **103**, 243 (1997).

123. Onuki Y., Settai R., *Physica B* **300**, 61 (2001)

Reproduced with permission of the copyright owner. Further reproduction prohibited without permission.

APPENDIX

LETTER OF PERMISSION

AMERICAN PHYSICAL SOCIETY

AMERICAN PHYSICAL SOCIETY

October 29, 2001

Umit Alver, PhD. Candidate
Department of Physics and Astronomy
Louisiana State University
Baton Rouge, LA 70803, PhD. Candidate
Department of Physics and Astronomy
Louisiana State University
Baton Rouge, LA 70803

Attn: Dr. Alver

RE: **Your request to reprint or mount your Article, or any portion of it, in your thesis or Dissertation**

Articles: Phys. Rev. B, 64, 064506-1. Figures 1, 2, 3, 6, 7, and 8, plus Tables II, III, and V. Phys. Rev. B, 64, 180402-1. Figures 1, 2, 3, and 4.

As the author of the requested material, you retain the right, after publication, to use all or part of the article, without revision or modification including the APS formatted version, in personal compilations or other publications of your owns works, including your personal web home page, and to make copies of all or part of the material for your use for lecture or classroom purposes and in your thesis or dissertation.

Please cite the original publication in full and the copyright line as follows:

Authors names, journal title, volume number, year of publication, and page numbers.
"Copyright (year) by the American Physical Society."

If you wish to mount or post your Article on your personal webpage, please set-up a link to the article's abstract page ("wrapper"), using APS's simple URL formula ("link manager," http//publish.aps.org/linkfaq.html).

For example, the URL for Physical Review Letters, Vol. 83, p. 4872 would be:
http://publish.aps.org/abstract/prl/v83/p4872

Reproduced with permission of the copyright owner. Further reproduction prohibited without permission.

The Article may not be sold in any format. The definitive version of the Article is the APS online version.

For your reference, a copy of the APS Copyright Form can be found at:
ftp://aps.org/pub/jrnls/copy_trnsfr.pdf

If you have any questions, please feel free to contact us.

Sincerely,

Anita Wiley, APS Customer Service

**The APS formatted version is the full text PostScript (PS) or the PDF version produced by APS or its vendors with no links or navigation.*

Reproduced with permission of the copyright owner. Further reproduction prohibited without permission.

VITA

Umit Alver was born in Amasya, Turkey, on March 25, 1968. After graduating from Trabzon High School in 1985 he entered the Faculty of Education, in Karadeniz Technical University from which he received a diploma in Physics in 1989. From 1990 to 1993 he worked as a physics teacher in Trabzon Technical High School and from 1993 to 1995 he worked as a research assistant at Department of Physics of Karadeniz Technical University. In May 1995, he came to Old Dominion University in Virginia as a sponsored student from the Higher Educational Council of Turkey and obtained an Master of Science in Physics in 1997. In August 1997, he enrolled at Louisiana State University to pursue a Doctor of Philosophy in Physics.

Reproduced with permission of the copyright owner. Further reproduction prohibited without permission.

DOCTORAL EXAMINATION AND DISSERTATION REPORT

Candidate: UMIT ALVER

Major Field: PHYSICS

Title of Dissertation: de Haas van Alphen Effect Measurements on CexLa(1-x)MIn5(M=Co, Rh, Ir) Alloys

Approved:

R.G. Goodrich
Major Professor and Chairman

Dean of the Graduate School

EXAMINING COMMITTEE:

Robert L. Kurtz

Hyo Prakash Sarma

Julia Chan

P.K. Ajmera

Date of Examination:

October 15, 2001

Reproduced with permission of the copyright owner. Further reproduction prohibited without permission.